ABSTRACT

Title of Document: ASSESSING FOREST BIOMASS AND
                            MONITORING CHANGES FROM
                            DISTURBANCE AND RECOVERY WITH
                            LIDAR AND SAR

                            Wenli Huang, Doctor of Philosophy, 2015

Directed By: Professor Guoqing Sun, Department of
                            Geographical Sciences

This dissertation research investigated LiDAR and SAR remote sensing for assessing aboveground biomass and monitoring changes from anthropogenic forest disturbance and post-disturbance recovery. First, waveform LiDAR data were applied to map forest biomass and its changes at different key map scales for the two study sites: Howland Forest and Penobscot Experimental Forest. Results indicated that the prediction model at the scale of individual LVIS footprints is reliable when the geolocation errors are minimized. The evaluation showed that the predictions were improved markedly (20% R^2 and 10% RMSE) with the increase of plot sizes from 0.25 ha to 1.0 ha. The effect of disturbance on the prediction model was strong at the footprint level but weak at the 1.0 ha plot-level. Errors reached minimum when footprint coverage approached about 50% of the area of 1.0 ha plots (16 footprints) with no improvement beyond that.

Then, a sensitivity analysis was conducted for multi-source L-band SAR signatures, to change in forest biomass and related factors such as incidence angle, soil moisture, and disturbance type. The effect of incidence angle on SAR backscatter was reduced by an empirical model. A cross-image normalization was used to reduce the radiometric distortions due to changes in acquisition conditions such as soil moisture. Results demonstrated that the normalization ensured that the derived biomass of regrowth forests was cross-calibrated, and thus made the detection of biomass change possible.

Further, the forest biomass was mapped for 1989, 1994 and 2009 using multi-source SAR data, and changes in biomass were derived for a 15- and a 20-year period. Results improved our understanding of issues concerning the mapping of biomass dynamic using L-ban SAR data. With the increase of plot sizes, the speckle noise and geolocations errors were reduced. Multivariable models were found to outperform the single-term models developed for biomass estimation.

The main contribution of this research was an improved knowledge concerning waveform LiDAR and L-band SAR's ability in monitoring the changes in biomass in a temperate forest. Results from this study provide calibration and validation methods as a foundation for improving the performance of current and future spaceborne systems.

ASSESSING FOREST BIOMASS AND MONITORING CHANGES FROM
DISTURBANCE AND RECOVERY WITH LIDAR AND SAR

By

Wenli Huang

Dissertation submitted to the Faculty of the Graduate School of the
University of Maryland, College Park, in partial fulfillment
of the requirements for the degree of
Doctor of Philosophy
2015

Advisory Committee:
Professor Ralph Dubayah, Chair
Research Professor Guoqing Sun, co-chair
Professor Eric Kasischke
Research Scientist Bruce Cook
Professor Andrew Baldwin

Dedication

To

My parents,
Bilong Huang & Guangmin Que,

and

My husband,
Rui Leng

For their endless love, supports and sacrifices.

Acknowledgements

Table of Contents

List of Tables

List of Figures

xi

Chapter 1 Introduction

1.1   Background

1.1.1   Relevance of forest biomass to terrestrial ecosystems and carbon budget

Terrestrial carbon storage is an critical component in the global carbon budget, and is essential to understanding climate change and ecosystem responses to human activities, however, current estimates contains high levels of uncertainties *(Le Quere et al., 2014).* The global carbon dioxide budget is described by emissions and sinks divided proportionally among atmosphere, ocean and land:

$$E_{FF} + E_{LULUC} = G_{ATM} + S_{OCEAN} + S_{LAND} \qquad\qquad \textbf{Equation 1-1}$$

Where E_{FF}, E_{LULCC} are the carbon sources from fossil fuel & cement, and land use and land-cover (LULUC) change; G_{ATM} is the carbon growth in the atmosphere; S_{LAND}, S_{OCEAN} are the carbon sinks from land and ocean (Figure 1-1). Note that the S_{LAND} and E_{LULUC} have the largest uncertainties of 2.9 ± 0.8 GtC/yr and 0.9 ± 0.5 GtC/yr, and both are associated with changes in forest carbon stocks.

Forest carbon stocks are generally stored in the form of biomass, which includes the above- and below- ground biomass (AGB and BGB), such as trees, shrubs, vines, roots, and the dead mass of fine and coarse litter associated with the soil. Forest aboveground biomass (hereafter biomass) can be converted into carbon stocks by multiplying a simple carbon fraction (about 0.5 in many cases). It is an important component in temperate and tropical forest ecosystems, and is a relatively smaller part in boreal forest ecosystems *(Malhi et al., 1999).*

Anthropogenic disturbance and management, including deforestation and forest degradation from management manipulations, have led to changes in biomass and thus the carbon budget *(Hall et al., 2011; Houghton et al., 2012)*. Yet the loss of carbon from forest disturbance and the gain from post-disturbance recovery have not been well assessed. Accurate surface measures of spatial and temporal variations in biomass change will support climate treaty frameworks such as Reduced Emissions from Deforestation and Forest Degradation Plus (REDD+).

Forest management might increase or decrease carbon storage (Figure 1-2), and applying the former will help to reduce climate disruption as well as increase forests' resilience in the face of climate change *(Evans and Perschel, 2009)*. There is a debate regarding the net effect of forest management on the carbon budget *(Nunery and Keeton, 2010)*, because it is difficult to accurately quantify how much of the forest carbon changes are due to stand-scale management and landscape-scale strategies *(Canadell and Raupach, 2008)*. Forest management has been incorporated into estimates in net flux of carbon in forest only recently *(Houghton et al., 2012)*.

Therefore, accurately quantifying biomass and changes after forest disturbance is desirable in order to reduce the uncertainties in the carbon budget, and thus to inform the policy and decision-making community.
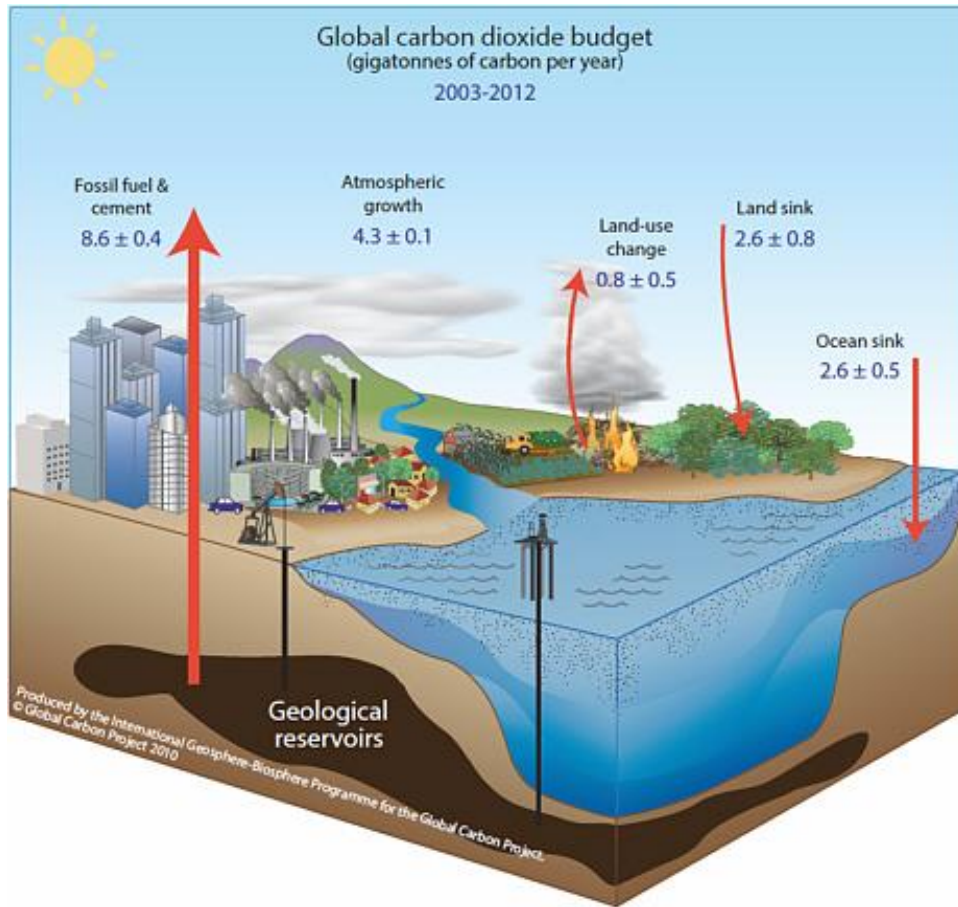
Figure 1-1. Conceptual diagram of global carbon dioxide budget. Global Carbon Project 2014 (Le Quere et al., 2014).
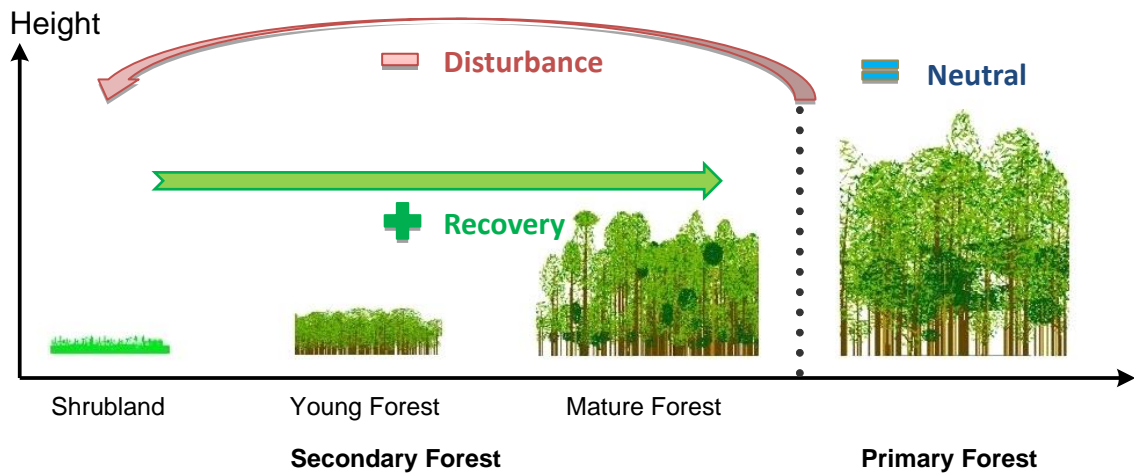
Figure 1-2. Conceptual relationship between changes in forest and carbon budget.

1.1.2   Current approaches to estimate forest carbon stocks and changes

Three approaches summarized by *Houghton et al. (2012)* have been applied to estimating forest biomass density (Mg·ha^{-1}) and changes in density due to LULUC: 1) field inventory, 2) remote sensing-based estimates, and 3) modeled estimates.

A. Field inventory

Table 1-1. Comparison of the forest biomass from field inventory

Category	Approach	Description	Advantages	Disadvantages
Direct	Destructive sampling	Harvest of all or representative trees	Accurate and direct measure;	Time-consuming & labor-intensive;
		Fresh/dry masses weighted	Essential for development of allometric equations	Relationship applied for limited regions
Indirect	Allometric equations	Species based relationship between biomass and dbh, tree height, and wood density	Easy to conduct measurements in the field	Relationship varied due to environmental and climate conditions
	Component ratio method	Biomass converted from volume	With many sampled plots from national forest inventory	Relationship varied due to environmental and species composition

Field inventory, either directly or indirectly conducted, is the most accurate approach for measuring forest biomass (Table 1-1). Specifically, direct measurement requires harvest of all materials, average stands, or individual representative trees *(Monk et al., 1970)*. Many regional studies usually destructively sample individual trees to build up an allometric relationship between biomass and field measured tree attributes such as height and dbh (diameter at breast height) through regression analysis. On the other hand, indirect field inventories consist of allometric methods (*i.e.*, regional or national allometric equations *(Jenkins et al., 2003)* and volume based methods (*i.e.*, component ratio method *(Heath et al., 2008)*. These field inventories

4

form the basis for many national forest inventories and can be combined with LULCC to track changes in carbon using an empirical bookkeeping method which assigns averaged values for each type of forest. However, these ground-only inventories are labor and time intensive, and are unable to reflect the spatial variation of biomass within forest *(Houghton et al., 2012).*

B. Remote sensing

Field inventories are accurate if properly conducted, however they are labor-intensive and time-consuming. Moreover, no method is currently capable of measuring forest biomass directly in a spatial continuous content, therefore a combination of remotely sensed data and a well-established field inventory is considered suitable for informing programs such as REDD+ *(Langner et al., 2014; Næsset et al., 2013).*

A variety of remote sensing techniques have been investigated for estimation and monitoring of forest carbon stocks *(Goetz and Dubayah, 2011; Lu, 2006; Lu et al., 2014)*, and can be generally classified into three major groups based on the sensor systems used: 1) passive multispectral and hyperspectral sensor, 2) LiDAR (Light Detection and Ranging), and 3) radar (Radio Detection and Ranging) (Table 1-2). Passive multispectral and hyperspectral imagery can provide mapping of spatially continuous content, but with limited sensitivity to forest biomass unless associated with canopy vertical structure from LiDAR and radar. The capability of LiDAR in estimating forest biomass is promising, yet LiDAR has inherent limited spatial coverage and temporal resolution. Current LiDAR systems either provide data with limited spatial coverage and temporal resolutions (airborne systems such as small

footprint discrete-return and large footprint waveform systems), or sampling data with sparse temporal observations (spaceborne large footprint waveform systems). Radar such as Synthetic Aperture Radar (SAR) compensates for this limitation with global coverage and more frequent repeated observations, showing the ability to monitor deforestation and forest degradation *(Almeida-Filho et al., 2009; Rosenqvist et al., 2003)*. But many factors other than the change in forest structure and biomass, such as radar incidence angle and looking direction, as well as surface and environmental conditions, also affect the radar backscattering.

Table 1-2. Comparison of the forest biomass from remote sensing-based estimation

Category	Sensor	Variables	Advantages	Disadvantages
Passive	Multi-spectral	Spectral bands Vegetation index	Wall-to-wall	Saturation observed
	Hyper-spectral	Multiple bands	Accurate for species classification	Saturation observed
Active	SAR	Backscatter coefficients	Wall-to-wall	Limited by environmental conditions (*i.e.*, Soil moisture); Saturation observed
	InSAR	Coherence Height of phase center Canopy height	Repeat observations	Saturation observed
	LiDAR	Sampling of target attributes	No saturation	Limited observations

Due to issues with each sensor system, few studies have looked into the potential for monitoring changes in biomass after forest disturbance and post-disturbance recovery, only a limited studies have assessed the net effect on changes in carbon budget using remote sensing techniques *(Dubayah et al., 2010; Hudak et al., 2012)*. Two sets of methods used for mapping changes in forest biomass using remote sensing are: 1) the direct method which relates field-derived changes in

estimated biomass to temporal changes in remote sensing signatures directly; and 2) the indirect method (or time-for-space method) which first develops one or two sets of models to retrieve forest biomass from remote sensing observations, and then calculates change by subtracting one from another. The direct method requires two or more co-incident sets of estimated biomass from field measurements *(Dubayah et al., 2010)*, which is rare and limits its applications. On the other hand, the indirect method is less efficient than the direct method in terms of accuracy *(Rowland et al., 2008)*, but is more applicable with current field measurements once the repeated remote sensing observations are available. Recently, studies have looked into the possibility of monitoring biomass dynamic using LiDAR and SAR remote sensing *(Mitchard et al., 2011b; Rowland et al., 2008)*. The potential method and key issues of using LiDAR and SAR data for assessing forest biomass and monitoring changes in biomass after forest disturbance were investigated by empirical approaches in this study. In addition, various factors affect the relationship of remote sensing observations to forest biomass, leading to a large uncertainty in estimates. Important sources of uncertainty are found in mapping biomass and changes in biomass from remote sensing: (1) uncertainties in the estimate of remotely sensed measurements, (2) uncertainties resulting from the biomass prediction models, (3) uncertainties in the in-situ estimates of forest attributes, and (4) uncertainties due to time-shift between in situ estimate and remotely sensed measurements *(Weisbin et al., 2013)*. Uncertainties from these sources in using LiDAR and SAR data will be addressed in this study.

C. Modeled estimates

A third approach employs physical-based inversion via Radiative Transfer Model (RTM) or process-based ecosystem models that calculate internally the carbon density of vegetation and soils in different types of ecosystem initialized by climate drivers *(Peddle et al., 2011; Ranson et al., 2001).* Results from remote sensing such as vegetation types and canopy vertical structure are a critical input for these forest ecosystem models, and forest biomass is an essential product for validation of output from these models.

1.2 *Research questions and objectives*

This dissertation will address the following two major questions: 1) what is the level of sensitivity of remotely sensed signatures (i.e., from waveform LiDAR and SAR) to changes in forest biomass caused by disturbance and post-disturbance recovery? And 2) what are the key factors to be considered in monitoring and assessing the net change in forest biomass, including loss from forest disturbance and gain from post-disturbance recovery, via LiDAR and radar remote sensing?

The overall goal of this study is to monitor forest biomass and assess its change after disturbance using LiDAR and radar remote sensing. Specifically,

1) Mapping forest biomass from waveform LiDAR data, and assessing the loss from disturbance and gain from post-disturbance recovery.

2) Analyzing the sensitivity of SAR signatures to forest disturbance and major influence factors, including incidence angle, soil moisture, and disturbance type.

3) Mapping aboveground biomass data, and assessing the changes after disturbance using multi-source SAR data from spaceborne and airborne platforms.

1.3   *Howland Forest and Penobscot Experimental Forest*

Forest management strategies are changing over time and have distinct impacts on the forest structures and thus on biomass. Statistics reported by the U.S. Forest Service (*Figure 1-3*) show that total harvest wood volume at the State level (solid line with filled dot) is relatively stable, but partial harvest (dark grey filled bars) has increased dramatically and becomes a major management strategy over the last two decades in Maine *(Scott et al., 2004)*. The use of clear-cut will result in a regrowth similar to natural forest. On the other hand, shelterwood harvest, which allows a natural regeneration by increasing light penetration from an opened forest canopy, can maintain the same maximum tree height with decreased total biomass at stand-level.
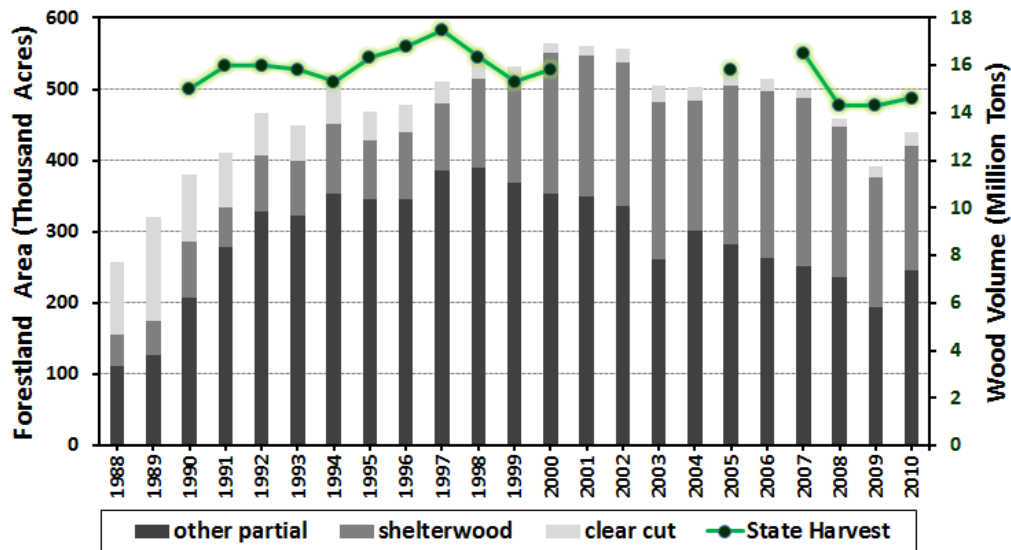
Figure 1-3. Forest Harvest Trend in Maine, data from Maine Forest Service. Types of harvest: partial=harvest where trees are removed individually or in small (<5 acre) patches; shelterwood=harvest of mature trees from a forest site in two or more stages (5-15 years apart); clear-cut=harvest on a site larger than 5 acres that results in a residual basal area of acceptable growing stock trees >4.5" DBH of less than 30".

Howland Forest (HF) (45°08' ~ 45°14' N, 68°42' ~ 68°45' W), and the Penobscot Experimental Forest (PEF) (45°49' ~ 45°52.5' N, 68°30' ~ 68°38.5' W) are located in south-central Maine. These forests belong to a transition zone between eastern broadleaf and northern forest. They are essential ecological research stations in support of multi-disciplinary studies such as biodiversity, conservation, forest-atmosphere-soil carbon exchange, and forest management for timber production. Most importantly, they provide ground-truth data dating back to the mid-20th century for forest biomass studies. HF has an AmeriFlux Tower within an intermediate aged forest, and the surrounding areas are privately land owned by a timber production company (International Paper®, IP) with different forest management manipulations over the last three decades, such as clear-cuts and plantation during the 1980s, strip-cuts during the 1990s, and select-cuts (shelterwood harvest and reestablishment) after 2000. Harvests since 2000 mostly employ the shelterwood method which typically consists of 3 separate entries spaced 10 years apart, with each entry removing about 1/3 of the basal area *(Scott et al., 2004)*.

HF and PEF sites consist of sub-boreal forest with mixed deciduous and coniferous tree species *(Hollinger et al., 1999; Safford et al., 1969)*. The dominant species include *Tsuga canadensis* (eastern hemlock), *Picea rubens* (red spruce), *Acer rubrum* (red maple), *Abies balsamea* (balsam fir), *Thuja occidentalis* (northern white cedar), *Betula papyrifera* (paper birch), *Fagus grandifolia* (Beech), *Betula alleghaniensis* (yellow birch), and *Larix laricina* (Tamarack) (see Table 5-1 for details). The region features relatively level and gently rolling topography.

According to USGS 1/3-Arc Second National Elevation Dataset (NED) published in

2009, the elevation ranges from 40 m to 178 m at HF, and from 29 m to 83 m at PEF.

These two sites were selected for this study mostly due to the abundant

ground measurements as well as the large number of remotely sensed datasets that

have been collected. Details about the field campaign and remotely sensed datasets

are given in the following chapters.
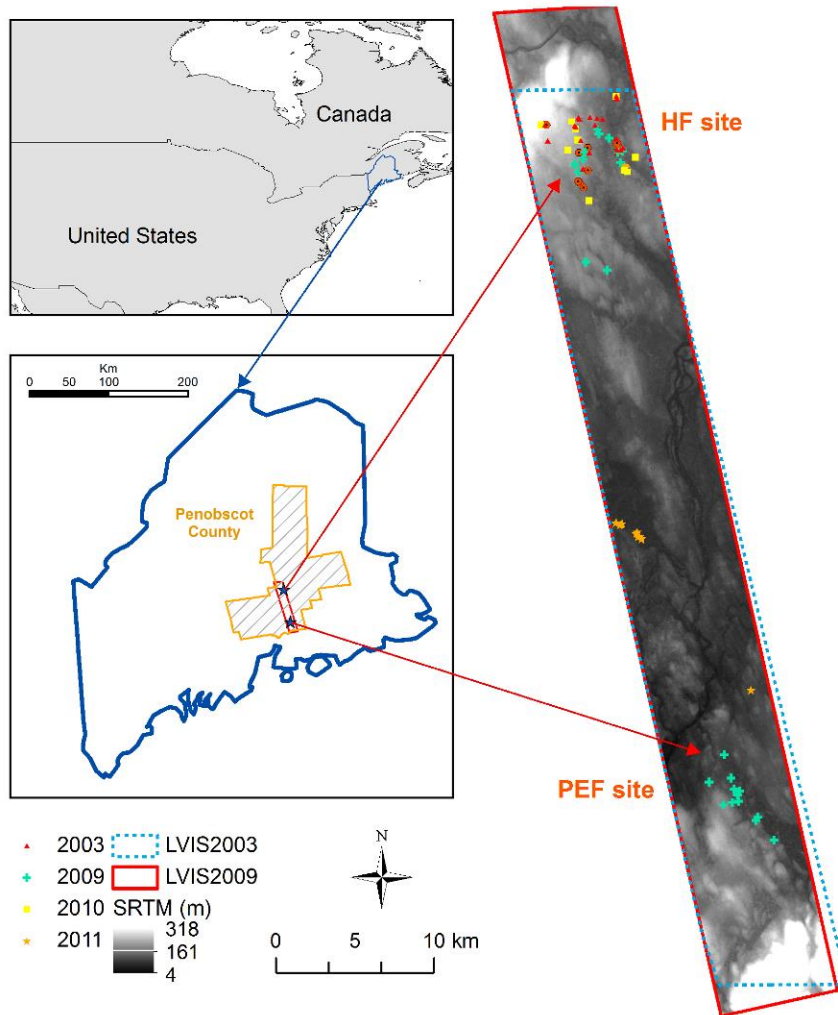
Figure 1-4. Location of study area and field sites: the site to the north is Howland
Forest (HF), and the site to the south is Penobscot Experimental Forest (PEF).

1.4   *Dissertation outline*

This dissertation contains 5 chapters. This, the first chapter, summarizes the relevance of biomass estimation to the broader discipline of Climate Change and current approaches that are applied for mapping and monitoring forest biomass.

Chapter 2 demonstrates the ability of repeat LiDAR measurements to map the changes in forest biomass, and thereby to evaluate the loss from forest disturbance and the gain from recovery. Within the study sites, regression models developed at the footprint scale (~0.06 ha) were evaluated with independent plot-level data (up to 1 ha), and footprint-level models were applied within the study sites. The effects of forest disturbance on prediction models were investigated. The influence of footprint density on biomass predictions is discussed, and average annual biomass reduction rate from forest disturbance are given.

Chapter 3 analyzes the sensitivity of SAR signatures to forest biomass and changes due to disturbance. Sensitivity analysis was conducted to investigate the influence of radiometric distortion caused by incidence angle, and the backscatter variation caused by soil moisture. Feasibility of cross-image normalization between multi-temporal and multi-sensor SAR data is demonstrated; and the possibility of applying normalized backscatter to detect biomass changes due to forest disturbance and post-disturbance recovery is discussed.

Chapter 4 focuses on the application of multi-temporal and multi-sensor SAR data to map biomass and biomass changes after forest disturbance. Cross-image normalization proposed in Chapter 3 is applied to airborne and spaceborne multi-temporal SAR data, and single-term and multi-variable regression models are

developed. Results from leave-one-out cross-validation are summarized, comparison to lidar-derived biomass map is given, and the changes in biomass from for a 15- and 20- year period from spaceborne and airborne SAR data are reported.

Chapter 5 summarizes the main findings and contributions from the previous chapters. Future research directions are also discussed based on the results from this dissertation study in relation to subsequent spaceborne LiDAR and SAR missions.

Chapter 2 Mapping Biomass Change after Forest Disturbance using waveform LiDAR[1]

2.1   Introduction

Aboveground biomass (AGB, here after biomass) stock from forest represents a significant component of the global carbon cycle *(Goetz and Dubayah, 2011)*. A variety of passive and active remote sensing techniques have been investigated for measuring and monitoring forest carbon stocks *(Goetz and Dubayah, 2011; Lu, 2006)*. Light detection and ranging (LiDAR) is promising because of its ability to directly measure canopy vertical profile, providing canopy height information which is highly correlated with the forest biomass. LiDAR systems are categorized as small- or large-footprint based on the size of the illuminated ground area. Small-footprint LiDAR systems (5-30 cm diameter) provide dense samples for detailed representation of the canopy structure, but their use is restricted to low-altitude airborne platforms. Small footprint full waveform systems have appeared in recent years with ability to record the complete waveform *(Mallet and Bretar, 2009)*. Large-footprint laser systems (10-70 m diameter) record a continuous, vertical profile of returned signal. Although large-footprint LiDAR data is not able to capture the very fine spatial details of forest canopies, structural attributes can be derived from vertical profiles of return energy for application in ecology studies *(Mather, 2004)*. LiDAR derived metrics from small-footprint discrete return LiDAR *(Asner et al., 2010; Gonzalez et*

---

al., 2010; Næsset and Gobakken, 2008; Nilsson, 1996; Pang et al., 2008; Zhao et al., 2011) and continuous returned full-waveform LiDAR *(Drake et al., 2002; Drake et al., 2003; Dubayah et al., 2010; Lefsky, 2010; Lefsky et al., 2002b; Lefsky et al., 1999; Lefsky et al., 2005a; Lefsky et al., 2007; Means et al., 1999; Ni-Meister et al., 2010)* have been used for estimation of forest canopy height and biomass. Various multi-sensor fusion *(Asner et al., 2012; Asner et al., 2010; Kellndorfer et al., 2010; Lefsky et al., 2005b; Nelson et al., 2009; Saatchi et al., 2011b; Sun et al., 2011; Swatantran et al., 2011)* used LiDAR samples and optical or radar imagery data for regional to continental mapping of forest attributes.

Laser Vegetation Imaging Sensor (LVIS) *(Blair and Hofton, 1999)* with a footprint size of 10-25 m, records the entire profile (waveform) of the return signal in ~30 cm vertical bins *(Dubayah and Drake, 2000; Dubayah et al., 2010)*. Because the footprint size is larger than the diameter of a tree crown and the laser beam can pass gaps between trees, a waveform can capture the tree top and ground surface in a forest stand. Studies have confirmed the ability of LVIS-derived metrics to estimate biomass, even in dense tropical forests. *Drake et al. (2002)* reported that height of mean energy (HOME or RH50) is the best single term predictor for estimating tropical forest biomass at the LVIS footprint-level (~0.05 ha, 25 m diameter) and the plot-level (~0.5 ha). The issue of sampling sizes has also been discussed by several studies with small- to large-footprint LiDAR system. They compared regression models at the footprint-level and the plot-level for a tropical wet forest at La Selva, Costa Rica, and found that because of geolocation uncertainties, large tree location, and species composition, the prediction model was better at plot-level with the R2 of

0.73 and RMSE of 60.02 Mg·ha^{-1}. Results from *Hyde et al. (2005)* indicated a strong

agreement between field data and LVIS measurements for height ($R^2=0.75$;

RMSD=8.2m) and biomass ($R^2=0.83$; RMSD=73.5 Mg·ha^{-1}) at Sierra Nevada sites in

California, but not for canopy cover. *Anderson et al. (2006)* found good relationship

between LVIS metrics and height (R2=0.80), but the relationship is weaker between

metrics and biomass ($R^2=0.61$, RMSE=58 Mg·ha^{-1}) at Bartlett Experimental Forest

(BEF) in New Hampshire, USA. According to *Anderson et al. (2008)*, the possible

factors for a weaker correlation include geolocation error, species composition, and

intensity of disturbance. *Dubayah et al. (2010)* applied the LVIS data for mapping

biomass change. They found various issues that need to be considered in detecting

and mapping the biomass change with LVIS data, and suggested using range-distance

based ΔRHE metrics to develop the uniform biomass change equation at plot-level to

avoid errors caused by ground detection and two sets of regression models. Asner et

al. (2010) noted the scaling issue that the small-footprint LiDAR prediction errors

decrease with the increase of plot size. *Mascaro et al. (2011)* proposed a "crown-

distributed" approach to address the plot and edge scaling issues caused by the

disagreement between LiDAR and field measurements.

The effects of disturbance on the relationship between biomass and height

metrics were investigated by field observations and model simulation. *Drake et al.*

(2003) investigated the relationships of simple LiDAR metrics (*i.e.*, RH50) with

estimated biomass, and indicated that there are significant differences between

different types of forest (*i.e.*, tropical wet forest and tropical moist forest). *Ni-Meister*

et al. (2010) indicated that combined height and gap fraction could improve the

estimation of biomass particularly for coniferous. *Ranson and Sun (2010)* simulated the waveforms RH metrics from different stands (disturbed and undisturbed forest) by a 3D-LiDAR model, and showed that the relationships between forest biomass and LiDAR metrics were distinguishable. *Asner et al. (2011)* found that the fitted curves between forest carbon stocks and LiDAR signals are different from plantations and natural regrowth after disturbance because of stocking differences. Inventory data and modeling results also demonstrated that young forests accumulated biomass much faster than the matured forest for the first 10 to 20 years after disturbance *(Chazdon, 2003)*. Vegetation change tracker (VCT) algorithm was designed for detecting forest disturbance *(Huang et al., 2010)* via spectral-temporal information from Landsat time series stack (LTSS). The products of yearly disturbance maps from LTSS-VCT were used in this study.

The biomass prediction models can be developed at the scale of footprints and larger plots. To facilitate regional and global biomass mapping using LiDAR waveform data, models at footprint-level are desirable because sampling large plots is much more time consuming than footprint-level sampling. The accuracy of biomass estimation at coarser scales will depend on the accuracy of the footprint-level models and the number of samples (footprints) at this scale. In this study we will investigate 1) if the model at footprint-level can be developed with desirable accuracy in our study sites, 2) if the forest management practices in term of disturbances will affect the models, and 3) what will be the proper scale with concern of uncertainties for mapping biomass from LVIS data in our study sites. Forest biomass map at 1.0 ha

pixel size was produced from LVIS acquired in 2003 and 2009. The changes of biomass from 2003 to 2009 were analyzed in this study.

2.2   Data

2.2.1   Field campaign

Field measurements for this chapter were conducted during August 2009 to 2011. Both footprint-level (~0.03 ha, 20 m diameter) and plot-level (0.25 ha - 1.0 ha) plots (see Figure 2-1 for typical layout) were measured. Differential Global Position System (DGPS) instruments were used to locate LVIS footprints and establish sampling plots.

Twenty-four 1.0 ha plots (hectare plot, 200m $\times$ 50 m, Figure 2-1a) and ten 0.5 ha plots (half hectare plot, 100m $\times$ 50m, Figure 2-1b) were established in 2009 and 2010, respectively. The longer edges of these plots were in the range direction of the NASA/JPL Uninhabited Aerial Vehicle Synthetic Aperture Radar (UAVSAR) flight lines. The layout of these plots is illustrated in, where each plot consists of sixteen 0.25 ha (quarter hectare plot, 25m $\times$ 25m) subplots. Ninety-one circular plots with 20m diameter (Figure 2-1c) centered at each LVIS footprint were measured in 2010 and 2011. Forty-seven footprints were measured in August, 2010 and forty-four were measured during January and August of 2011.

Twenty forest inventory samples across the HF site were collected in October, 2003 for biomass and other forest parameters. For each inventory sample, three to four plots with radius of 4 m, 7 m or 10 m were arranged in the center, 30 m north, south-west, and south-east from the center. The diameter at breast height (DBH, diameter at 1.3 m above ground) for every tree with a DBH $\geq$ 3 cm were recorded

18

along with the species in both years. The relative canopy position (*i.e.*, dominant, co-dominant, intermediate, suppressed, or dead), heights of two dominant trees were measured for each plot in 1992. The height, crown length and width of 8 trees in each plot were measured in 2003. Details about collections of field data during the October 2003 campaign were described by *Sun et al. (2011)*. Seventeen forest inventory samples within the HF study site were used for the evaluation of 2003 biomass map.

From 2009 to 2011, the DBH, species of ever tree with DBH $\geq$ 10 cm, top height, height of crown base and crown width of the three highest trees in each subplot were recorded. A census of stems below the established size threshold (DBH < 10 cm) and height $\geq$1.3 m were sampled within a 2 m transect along the center of the rectangular plot, and from north-to-south in footprint-level circular plots. The number of stems falling into four diameter categories (*i.e.*, 0-2 cm; 2-5 cm, 5-8 cm and 8-10 cm) was counted and used as a representative sample of all small stems in the plot. Biomass values at HF and PEF span from 0.3 to 361.4 Mg ha^{-1} for 0.25 ha plots, 0.6 to 316 Mg ha^{-1} for 0.5 ha plots, and from 1.0 to 278.9 Mg ha^{-1} for 1.0 ha plots.
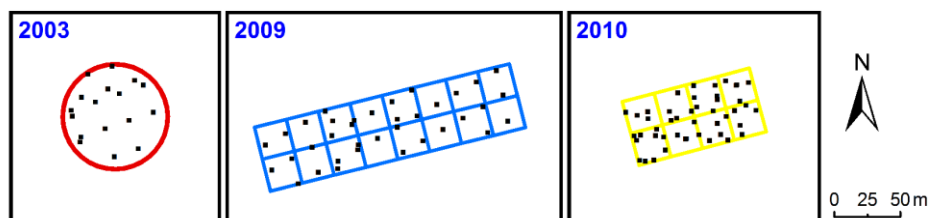
Figure 2-1. Layout of typical field plot in 2003, 2009, and 2010. (a) stand plot (80 diameter) in 2003; (b) 1-ha (50m by 200m) plot in 2009; (c) 0.5-ha (50m x 100m) plot in 2010. Black dots are LVIS footprint center.

2.2.2   LiDAR data

The Laser Vegetation Imaging Sensor (LVIS) is a large footprint airborne scanning laser altimeter developed by NASA Goddard Space Flight Center (GSFC) *(Blair et al., 2006; Blair et al., 1999)*. LVIS data of study area were acquired during leaf-on season in August of 2003 and 2009. For both years, the footprints had a nominal diameter of 20 m. The 2003 data was reprocessed in 2008, thus it is more consistent with the 2009 data.

LVIS products of version 1.02 provide three types of datasets: LVIS Canopy Elevation (LCE), LVIS Geolocated Elevation (LGE), and LVIS Ground Waveforms (LGW) *(Blair et al., 2006)*. From the waveform, mean elevation of the lowest detected mode is defined as ground elevation (zg). Then, relative heights (RH) to the ground elevation are calculated at quartile percentage of cumulative waveform energy (*i.e.*, 25%, 50%, 75%, and 100%). The footprint density varies at different locations in the study area because of overlapping flight lines during the campaign.

2.2.3   Auxiliary data

LTSS-VCT disturbance products were used in this study to identify disturbed forests from undisturbed ones *(Huang et al., 2010)*. The study area is located in the center of Landsat p011/r029 of the World Reference System (WRS) with good quality images. Subset product maps are used in this study to differentiate the year of disturbances (Figure 2-2). The product detects most of clear-cuts events, however, it has missed some strip-cutting around 1990-1995 and select-cut (shelterwood harvest) after 2000 at HF site. Similar problem has been noticed and documented at other validation sites in USA *(Thomas et al., 2011)*. Therefore, a further forest

20

management map was created from operation information from the private owner

(International Paper®, IP Company) and Google images at HF site. Several patches

of disturbed forest were digitized from Google Earth images and combined with

digitized version of management operation maps in different year. These maps were

used to identify the occurrence of disturbance, and will be explained in details in

sections of results and discussion.
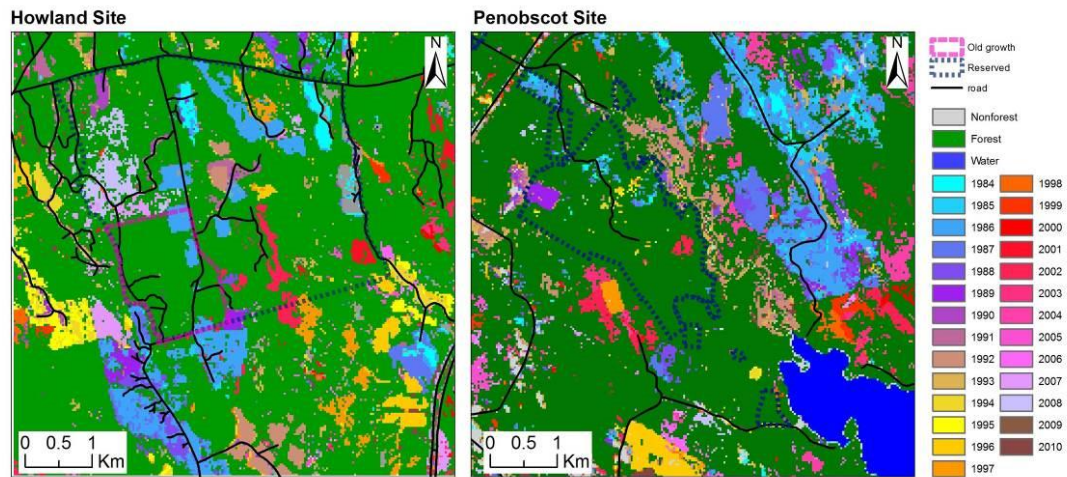
Figure 2-2. Year of disturbance from LTSS-VCT product at the HF and PEF study
sites. Pink polygon is the near matured forest at HF site; and dark blue polygon is the
outline of reserved area at both sites.

2.3   *Method*

2.3.1   Allometric-based biomass calculation

The diameter-based allometric equations used for large stems (DBH $\geq$ 10 cm)

and small stems (DBH < 10 cm) came from the comprehensive report of USDA on

North American forest *(Jenkins et al., 2003; Jenkins et al., 2004)*. Biomass of large

stems was calculated by corresponding species-specific allometric equations.

Biomass of the small stems was calculated by mixed hardwoods equations using the

midpoint of the diameter class (*i.e.*, 1.0 cm, 2.5 cm, 6.5 cm and 9.0 cm) as the DBH

times the number of stems in each category. Biomass was first calculated for each stem, and then total biomass was aggregated from subplot to plot levels.

2.3.2   LiDAR data processing

Relative height metrics (RH25, RH50, RH75 and RH100) of LVIS waveform were retrieved from LVIS LGE datasets for all sampling plots and measured footprints. The LVIS RH metrics of the study sites (HF and PEF) in 2009 were shown in Figure 2-3 as false color images (R: RH50, G: RH100, B: RH25). Images were created by interpolating of point data into 15m grid with a Delaunay triangulation method (TRIGRID function) provided by IDL Version 7.1 (Exelis, Boulder, CO).

The change in canopy profiles in waveform reveals the biomass change between 2003 and 2009. Waveforms acquired in 2003 and 2009 at HF site are shown in Figure 2-4. The distances between the waveform centers in 2003 and 2009 were less than 2 m. These waveforms represent the disturbed forest with (a) near-mature forest with neutral changes, (b) disturbed forest with negative change in RH metrics, and (c) forest with positive change in RH metrics, respectively.
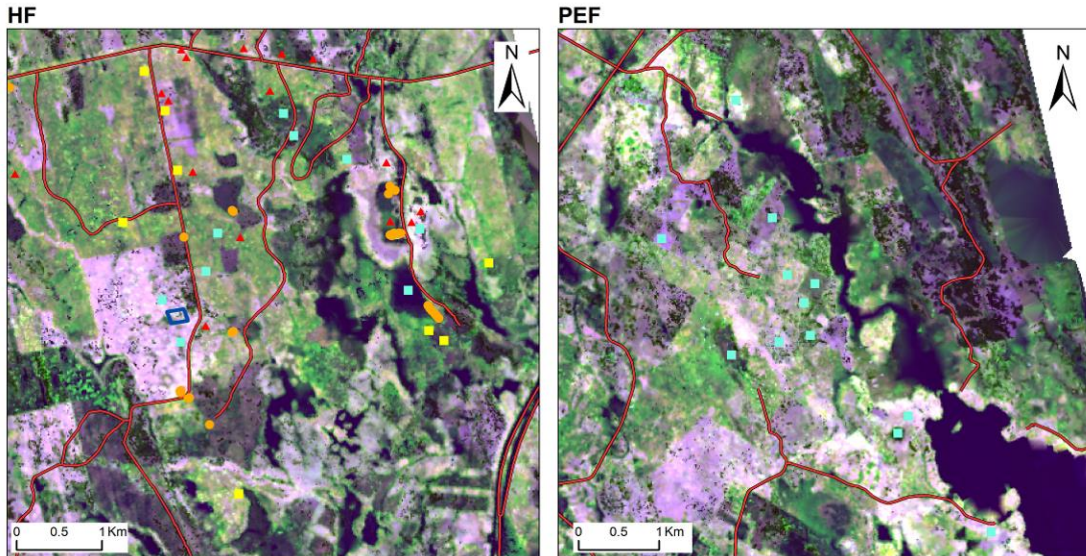
Figure 2-3. Images of gridded RH (R: RH50, G: RH100, B: RH25) metrics over study sites in 2009. Left - HF; right - PEF. Red lines are major roads. Dark blue rectangle in HF is the stem-map site. Field measurements are labeled with different colors for 2003 (red), 2009 (cyan), 2010 (yellow) and 2011 (orange).
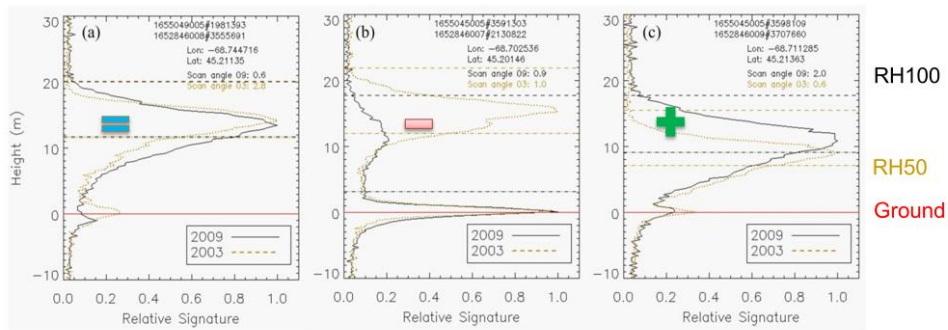
Figure 2-4. Typical co-incidence waveforms (center within 2m) from LVIS 2003 and 2009 data. (a) RHs relatively unchanged; (b) RHs have significant negative changes; (c) RHs with positive change. Black solid waveform is from 2009, gold dash waveform is from 2003. Red solid line is the detected ground in LGE, dashed straight lines are the RH100, dashed with dot lines are the RH50.

The density of LVIS waveforms in each field plot varied depending on number of overlapping flightlines at a given portion of forest. The nominal spacing of LVIS footprint is 20 m both along and cross track. Ideally, the nominal footprint density within a plot would be 9, 18, and 36 at sizes of 0.25 ha (50 m $\times$ 50 m), 0.5 ha (50 m $\times$ 100 m) to 1.0 ha (50 m $\times$ 200 m). However, two factors lead to a varied footprint density. First, there were overlapping LVIS flight lines for our study site. Similar issues have been mentioned at other LVIS study sites such as Sierra site in California *(Hyde et al., 2005)*, Bartlett site in New Hampshire *(Anderson et al., 2008)*, and La Selva site in Costa Rica *(Dubayah et al., 2010)*. In addition, the long edges of 50m $\times$ 200m field plots were set along the range direction of the UAVSAR data, which has a 10-20 $^\circ$ angle to the LVIS's flight direction as shown in Figure 2-4 b-c. Therefore, the averaged footprint density within the measured plots in 2009 and 2010 was not consistent and varied from 14, 27, and 53 footprints per plot from 0.25 ha, 0.5 ha to 1.0 ha plot-levels.

While processing the footprint-level field samples, two samples in the near matured old-growth forest region were found with wrong ground elevations (zg from LVIS LGE product) values. This discrepancy has been mentioned in LVIS known data set issues (*http://lvis.gsfc.nasa.gov/DataDisclaimer.html*), which is caused by insufficient energy returned from the ground and errors associated with the automated peak-finding algorithm. These two points were corrected in this study by finding a mean ground elevation of their neighboring footprints.

2.3.3 Forest disturbance identification

All sampled plots were classified as undisturbed or disturbed based on LTSS-VCT yearly disturbance product (1984 to 2010), high-resolution images and field notes. Forest disturbance maps were generated to show the disturbances prior to 2003, during 2003 to 2009 and after 2009 using the abovementioned data and forest management information from the owner. Most of the disturbed plots in HF site were those disturbed by management activities *(Sun et al., 2011)*, including clear-cut stands in the 1980s, strip-cuts in the 1990s and select-cuts (shelter-wood harvest) after 2000. A few tree plantations in our study site were also labeled as disturbed forest, as they were mainly planted after clear-cut. While the disturbance data we used relied heavily on the LTSS-VCT, we enhanced the classification using visual interpretation of high resolution imagery and field notes to refine the boundaries of forest disturbance patches. In addition, National Land Cover Data (NLCD) products in 2001 and 2006 were used to discriminate forest and non-forest for the entire study area. Woody forestlands and wetlands were included as forests in our analysis.

The sampled footprints consist of 47 undisturbed (51.6%) and 44 disturbed (48.4%) samples. The mean biomass value of undisturbed field samples (157.1 Mg·ha^{-1}) was higher than that of disturbed ones (87.4 Mg·ha^{-1}). At 0.25 ha plot-level, there were 41 undisturbed and 64 disturbed plots. At 0.5 ha plot-level, there were 18 undisturbed and 34 disturbed plots. At 1.0 ha plot-level, there were 10 undisturbed and 12 disturbed plots.

2.3.4   Mapping forest biomass and biomass changes

The mapping procedure consists of four steps: 1) develop the biomass estimation models from 2009 LVIS waveform data at the footprint-level and choose the best one; 2) evaluate the model performance with the plot-level observation data in 2009 and 2003, and determine the pixel size of the biomass map to be generated; 3) apply the selected model to generate biomass maps in both 2009 and 2003 with LVIS waveform data; and 4) detect the change in biomass from 2003 to 2009. The first two steps are shown in a conceptual workflow in Figure 2-5.
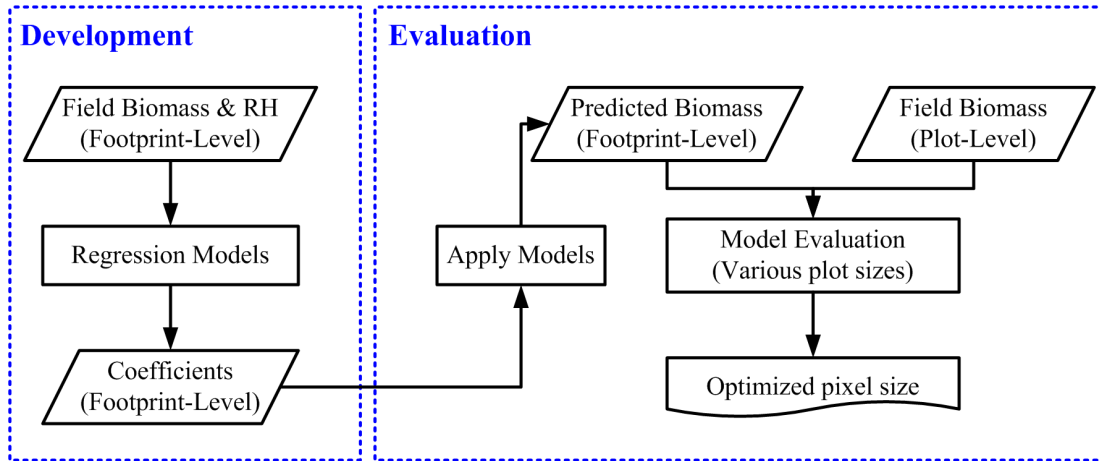
Figure 2-5. Workflow of model development and evaluation for biomass mapping.

This study employed several widely used statistical indicators to evaluate the accuracy of different regression models. Indicators included coefficient of determination (R^2), root mean square error (*RMSE*), and *RMSE (%)* which is the ratio of RMSE to mean observed value:

$$RMSE(\%) = \frac{RMSE}{\bar{y}}$$
    Equation 2-1

where $\bar{y}$ is the mean biomass.

26

A. Development of Regression Models

Linear regression models were developed relating field-measured biomass and LVIS metrics at footprint-level and evaluated at different plot-level (*i.e.*, 0.25 ha, 0.5 ha and 1.0 ha rectangular plot). Two types of models were developed, *i.e.*, combined model without consideration of disturbances and disturbance-specific models. RHs metrics are highly correlated as shown in Table 2-1, so we only develop the single term regression models.

Table 2-1. Correlation between RH metrics of LVIS footprint samples

	RH25	**RH50**	**RH75**	**RH100**
RH25	1.00			
RH50	**0.90**	1.00		
RH75	0.79	**0.96**	1.00	
RH100	0.72	0.87	**0.95**	1.00

A dummy variable was introduced into the linear regression model to test the effect of disturbances on intercepts and slopes *(Solberg, 2010)*. This dummy variable is used to indicate the occurrence of disturbance, where the truth is represented by a numerical value of 1. Then the equation becomes:

$$\text{Biomass} = \beta_1 + \beta_2 X_1 + \beta_3 X_2 + \beta_4 X_1 X_2 + e_i \qquad \textbf{Equation 2-2}$$

where $\beta_1 \sim \beta_4$ are estimated parameters, X_1 is the RH metrics in meters, X_2 is the dummy variable with values 0 (undisturbed) or 1(disturbed), and e_i is the error item. The hypothesis is H_0: $B_{undisturbd}$ - $B_{disturbed} = 0$ or $\beta_4 = 0$. If $\beta_4 = 0$ then we will reject the H_0 which means that the undisturbed and disturbed models are the same, otherwise they are different.

B. Evaluation of prediction models by field biomass data

Biomass of LVIS footprints within field plots was predicted from the footprint-level model and aggregated to the plot-levels. Then it was compared with corresponding field measurement. For 2009 data, the predicted biomass was evaluated with field measurements aggregated at three scales of plot-levels: 0.25 ha, 0.5 ha and 1.0 ha. For 2003 data, the field biomass was measured with FIA-style field measurements at ~0.5 ha plot-level. The predicted biomass was an average of the biomass from the footprints within a circle of 80 m diameter. The best mapping pixel size was determined by the plot-level model evaluation. Generally the aggregation footprint-level samples to larger plots reduced the overall variance and impact of geolocation errors *(Hall et al., 2011)*. Two recently studies have shown similar pattern that LiDAR prediction errors were reduced at larger plot sizes *(Frazer et al., 2011; Mascaro et al., 2011)*. The optimized pixel size for biomass mapping was selected based on statistical measurements including averaged prediction value, R^2, RMSE, and bias.

2.3.5   Biomass mapping from LVIS data

The mapping procedure is illustrated in Figure 2-6. First, two masks were created. A persistent non-forest mask was generated from NLCD product in 2001 and 2006. Non-forest pixels in both years were excluded from the mapping in this study. In addition, a data coverage mask was created for the area common to both LVIS data in 2003 and 2009. These masks were gridded into the selected optimized pixel size to match the biomass mapping scale. Next, the regression model was applied to the

LVIS footprints of entire study area in 2003 and 2009. Finally, the mean value of the

footprint-level biomass within each grid cell was calculated and assigned to the pixel.

The biomass change map was generated by subtracting 2003 biomass from that in

2009 within the forested area common to both LVIS data collections.
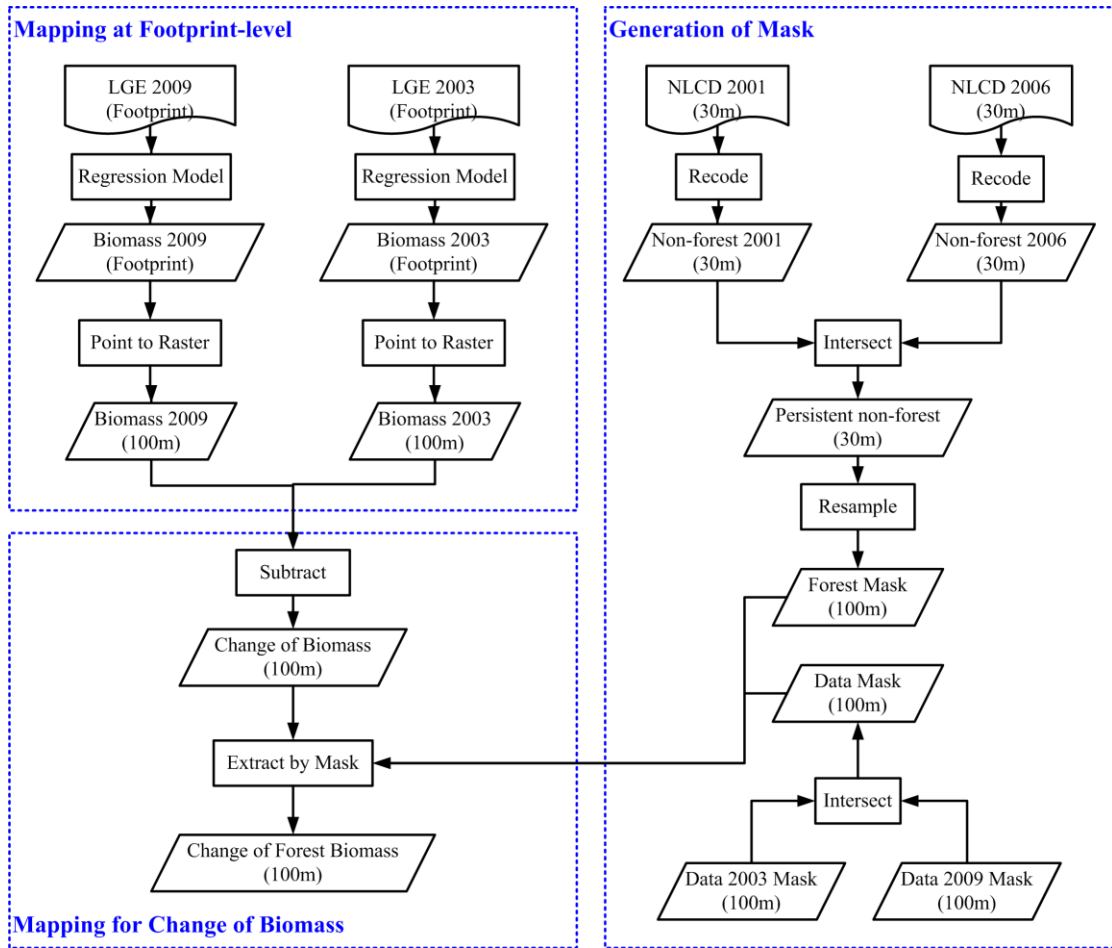
Figure 2-6. Biomass mapping and change detection from LVIS data.

2.4   Result

2.4.1   Model performance at the LVIS footprint-level

A. Single term regression model

Table 2-2 shows the biomass prediction from single term regression models. The biomass models at the footprint-level by all four RH metrics have high R^2 values ranging from 0.70 to 0.86. For all groups, there were strong and significant correlations ($p < 0.005$) between biomass and RH metrics. The RH50 and RH75 metrics perform similarly in terms of R^2, RMSE and RMSE (%). Averaged field biomass of 91 sampled footprints was 123.4 Mg·ha^{-1}. As mentioned above RH metrics are highly correlated. The correlation is as high as 0.96 between RH75 and RH50. Therefore, the single term regression model using RH50 was selected for the combined prediction model at the footprint-level for all data as it explains the greatest proportion of variance ($R^2 = 0.86$), and has the lowest residual error (RMSE = 31.0 Mg·ha^{-1}, and a relative error 25.1%).

Table 2-2. Summary of single term regression models at footprint-level

Model (ft-level)	Intercept	Slope	R^2	RMSE (Mg·ha^{-1})	RMSE (%)
Bio ~ RH25	90.8	22.0	0.70	45.1	36.5
Bio ~ RH50	**30.3**	**16.1**	**0.86**	**31.0**	**25.1**
Bio ~ RH75	-3.3	13.5	0.84	33.0	26.6
Bio ~ RH100	-51.9	11.1	0.74	42.1	34.2

*For 2009 data, Bolded is the selected model for mapping
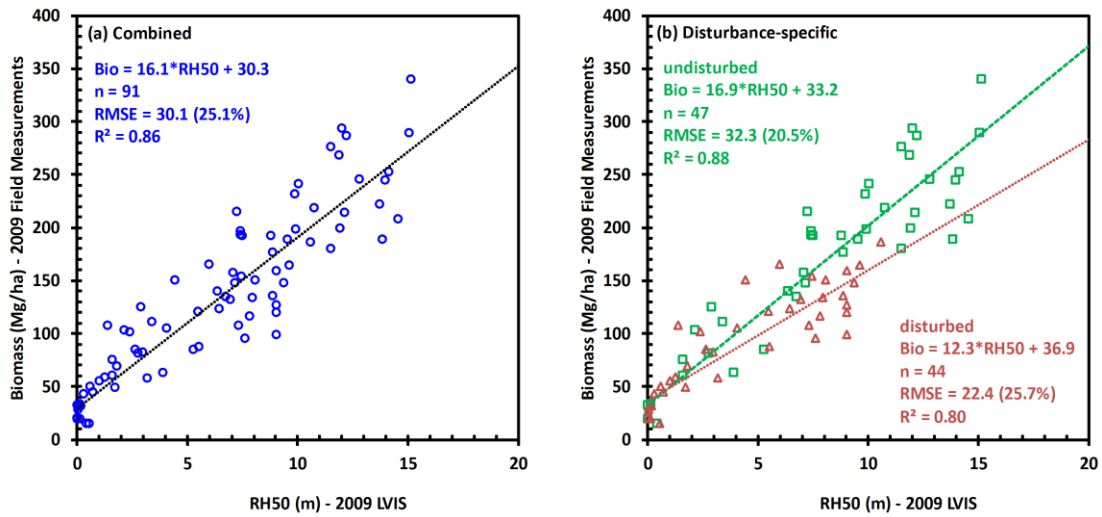
Figure 2-7. Relationship between field biomass and LVIS relative height metric RH50 at footprint-level: (a) Combined model; (b) Disturbance-specific models. Different colors indicate different models: rectangle dots (green) represent the undisturbed group, and triangle dots (red) represent the disturbed group.

Figure 2-7 shows the relationship between field biomass and RH50 and the contrast between undisturbed and disturbed groups at footprint-level. From Figure 2-7 (b), we could visually observe the two groups with different slopes of their trend lines. A statistical measurement was used to test the disturbance effect on intercepts and slopes in the next section.

B. Disturbance effect test

Following equation is from the regression when a dummy variable "disturb" with value 0 for disturbed and 1 for undisturbed forest was added for RH50 model:

Bio = 33.2 + 16.9*RH50 -3.7*disturb - 4.6*RH50*disturb   **Equation 2-3**

with Multiple R^2: 0.94, standard error: 28.7 Mg·ha^{-1}, F-statistic: 224.7 on 3 and 87 degrees of freedom, and a $p<0.001$.

31

Since the coefficient for the dummy variable ($\beta_4 = -4.6$) is not equal to zero, we reject the H_0 hypothesis. The effect of disturbances on biomass estimation model from RH50 is significant.

The dummy variable was also added to RH75 model and the regression equation was:

Bio = -8.6 + 15.4*RH75 -22.7*disturb - 6.0*RH75*disturb   **Equation 2-4**

with Multiple R^2: 0.95, standard error: 24.7 $Mg \cdot ha^{-1}$, F-statistic: 309.3 on 3 and 87 degrees of freedom, and a $p<0.001$.

Hence, we also rejected the H_0 hypothesis for the RH75 model.

A student T-test with two tails, unequal sample sizes, and unequal variance was employed to measure the disturbance effect on the predicted biomass. The T-test showed that disturbance has a significant effect on the predicted biomass from both RH50 ($p<0.001$) model and RH75 ($p<0.001$) model.

Thus, footprint-level single term models were developed for undisturbed and disturbed forest with RH50 and RH75 models. As shown in Table 2-3, both the RMSE and RMSE (%) were reduced for the disturbance-specific RH50 and RH75 models. Even though the R^2 and RMSE of the disturbance-specific models were not always better than the combined model, the comparisons between the field biomass and predicted biomass of all sample footprints showed better results from disturbance-specific models. The third lines in RH50 and RH75 of the disturbance-specific models are the results of comparing predicted biomass with field biomass of all sampling footprints. Disturbance-specific models explained higher predicted variance (RH50, $R^2=0.89$; RH75, $R^2=0.91$) than the combined model (RH50, $R^2=0.86$;

RH75, R^2=0.84). RMSE (RH50, 27.9 from 31.0 Mg·ha^{-1}; RH75, 24.2 from 32.9

Mg·ha^{-1}) as well as RMSE (%) (RH50, 22.6% from 25.1%; RH75, 19.6% from 26.6%)

were reduced. The large differences in RMSE (%) for different groups (disturbed,

undisturbed and all) are partially caused by the differences of mean biomass. The

mean biomass of the undisturbed forest (157.1 Mg·ha^{-1}) is over 50% larger than that

of the disturbed (87.4 Mg·ha^{-1}), and also larger than that of the combined plots (123.4

Mg·ha^{-1}).

Table 2-3. Combined and disturbance-specific models at footprint-level

Model	Variable	N	GP #	Intercept	Slope	R²	RMSE (Mg·ha⁻¹)	RMSE (%)
Combined	**RH50**	**91**	**all**	**30.3**	**16.1**	**0.86***	**31.0**	**25.1**
	RH75	91	all	-3.3	13.5	0.84*	32.9	26.6
Disturbance-specific	RH50	47	1	33.2	16.9	0.88*	32.3	20.5
		44	2	36.9	12.3	0.80*	22.4	25.7
		91	all	-	-	0.89*	27.9	22.6
	RH75	47	1	-8.6	15.4	0.89*	30.0	19.1
		44	2	14.1	9.4	0.90*	15.9	18.2
		91	**all**	**-**	**-**	**0.91***	**24.2**	**19.6**

GP#: 1 is undisturbed plots group, 2 is disturbed plots group; N: number of sample; *P-value < 0.005.
Bolded are models with best performance by evaluation at corresponding scale;

2.4.2 Evaluation of prediction model

A. Evaluation of combined prediction model in 2009 and 2003

The footprint-level RH50 model from the combined data

(*Bio=30.3+16.1*RH50*) was applied to 2009 LVIS data and evaluated at three plot-

levels: 1) 0.25 ha plot (50m $\times$50m), 2) 0.5 ha plot (50m $\times$100m), and 3) 1.0 ha plot

(50m $\times$200m), respectively. The evaluation plots were also divided into disturbed

and undisturbed plots using LTSS-VCT and Google Earth images.

The evaluation of the combined footprint-level models with plot-level field

data was shown in Table 2-4. As expected, the best model at three plot-levels in 2009

is RH50 model with higher explanation of total variance, lower RMSE and lower bias. The overall model performance improved with larger plot size from 0.25 ha, 0.5 ha to 1.0 ha. At 1.0 ha plot-level, the combined RH50 model explained 91% of the total variance with a positive bias of 2.0 Mg·ha^{-1} (1.4%) and RMSE of 22.4 Mg·ha^{-1} (15.6%).

Figure 2-8 shows the scatter plot of predictions versus field measurements from the best combined footprint-level prediction model. In 2009, the combined RH50 model has better performance than RH75 model from evaluations at all three plot-levels. While in 2003, the combined RH75 model was better than combined RH50 model. There is almost no bias (less than ±1.3%) observed for predictions in 2009, but the evaluation of 2003 biomass prediction at sampling sites showed worse results. In 2003, the combined RH75 prediction model overestimates the biomass with a positive bias of 11.9 Mg·ha^{-1} (+7.9%). It has lower explanation of total variance (54%) and higher RMSE of 46.6 Mg·ha^{-1}. The combined RH50 model also overestimates the biomass and has similar explanation of total variance (53%) and higher RMSE. A part of the reason is that the plot size and shape in 2003 (80m diameter circle, ~0.5 ha) were different from 2009 (rectangular) which leads to an inconsistency. The number of sample in 2003 is relatively small compared with that of 0.5 ha plot-level samples in 2009. In addition, the GPS unit used in 2003 for field-sampled plot wasn't as good as the one for 2009, which leads to geolocation errors.

Table 2-4. Evaluation of the footprint-level combined RH50 and RH75 models by plot-level field data in 2009 and 2003

Model	Year	Plot-size	N	Mean field	Mean predict	R^2	RMSE		Bias	
		ha		Mg·ha^{-1}	Mg·ha^{-1}		Mg·ha^{-1}	%	Mg·ha^{-1}	%
RH50		**0.25**	**105**	**143.6**	**144.5**	**0.79**	**32.6**	**22.7**	**+0.8**	**+0.6**
	2009	**0.5**	**52**	**142.7**	**144.4**	**0.83**	**28.5**	**20.0**	**+2.2**	**+1.5**
		1.0	**22**	**143.8**	**145.8**	**0.91**	**22.4**	**15.6**	**+2.0**	**+1.4**
	2003	0.5	17	151.0	168.0	0.53	50.4	33.4	+17.0	+11.2
RH75		0.25	105	143.6	147.1	0.72	37.3	26.0	+3.5	+2.4
	2009	0.5	52	142.7	147.7	0.76	33.8	23.7	+4.9	+3.5
		1.0	22	143.8	144.6	0.84	28.5	19.8	+0.8	+0.5
	2003	**0.5**	**17**	**151.0**	**162.9**	**0.54**	**46.6**	**30.9**	**+11.9**	**+7.9**

N: number of sample; Mean of field: mean biomass averaged over samples at plot-level; Mean of predict: mean predicted biomass averaged over samples at plot-level; Bolded are models with best performance at corresponding scale and year;

Table 2-5. Evaluation of the footprint-level disturbance-specific RH50 and RH75 models by plot-level field data in 2009 and 2003

Model	Year	Plot-size	N	Mean field	Mean predict	R^2	RMSE		Bias	
		ha		Mg·ha^{-1}	Mg·ha^{-1}		Mg·ha^{-1}	%	Mg·ha^{-1}	%
RH50	**2009**	**0.5**	**52**	**142.7**	**139.7**	**0.80**	**31.3**	**21.9**	**-2.9**	**-2.1**
		1.0	**22**	**143.8**	**145.8**	**0.91**	**23.1**	**16.1**	**+0.9**	**+0.6**
	2003	**0.5**	**17**	**151.0**	**170.9**	**0.51**	**54.6**	**36.2**	**+19.9**	**+13.2**
RH75		0.25	105	143.6	142.0	0.73	37.8	26.3	-1.7	-1.2
	2009	0.5	52	142.7	140.9	0.75	35.4	24.8	-1.9	-1.3
		1.0	22	143.8	145.4	0.86	27.9	19.4	+1.6	+1.1
	2003	0.5	17	151.0	171.3	0.48	57.4	38.0	+20.3	+13.4

N: number of sample; Mean of field: mean biomass averaged over samples at plot-level; Mean of predict: mean predicted biomass averaged over samples at plot-level; Bolded are models with best performance at corresponding scale and year;

B. Evaluation of disturbance-specific prediction models in 2003 and 2009

Similar steps were conducted to evaluate the disturbance-specific models by different plot-level data. Evaluation results were shown in Table 2-5. It can be seen from comparing the R^2 listed in the Table 2-4 and Table 2-5 that the disturbance-specific models preformed slightly better than common models. The disturbance-specific RH50 model has almost the same values of explanation of variance and RMSE as the combined RH50 model. At 1.0 ha plot-level, the disturbance-specific RH50 model explained 91% of the total variance, with a positive bias of 0.9 Mg·ha^{-1} (0.6%) and RMSE of 23.1 Mg·ha^{-1} (16.1%). The bias was reduced from -3.0 Mg·ha^{-1} to 0.9 Mg·ha^{-1} from 0.25 ha to 1.0 ha plot-levels.
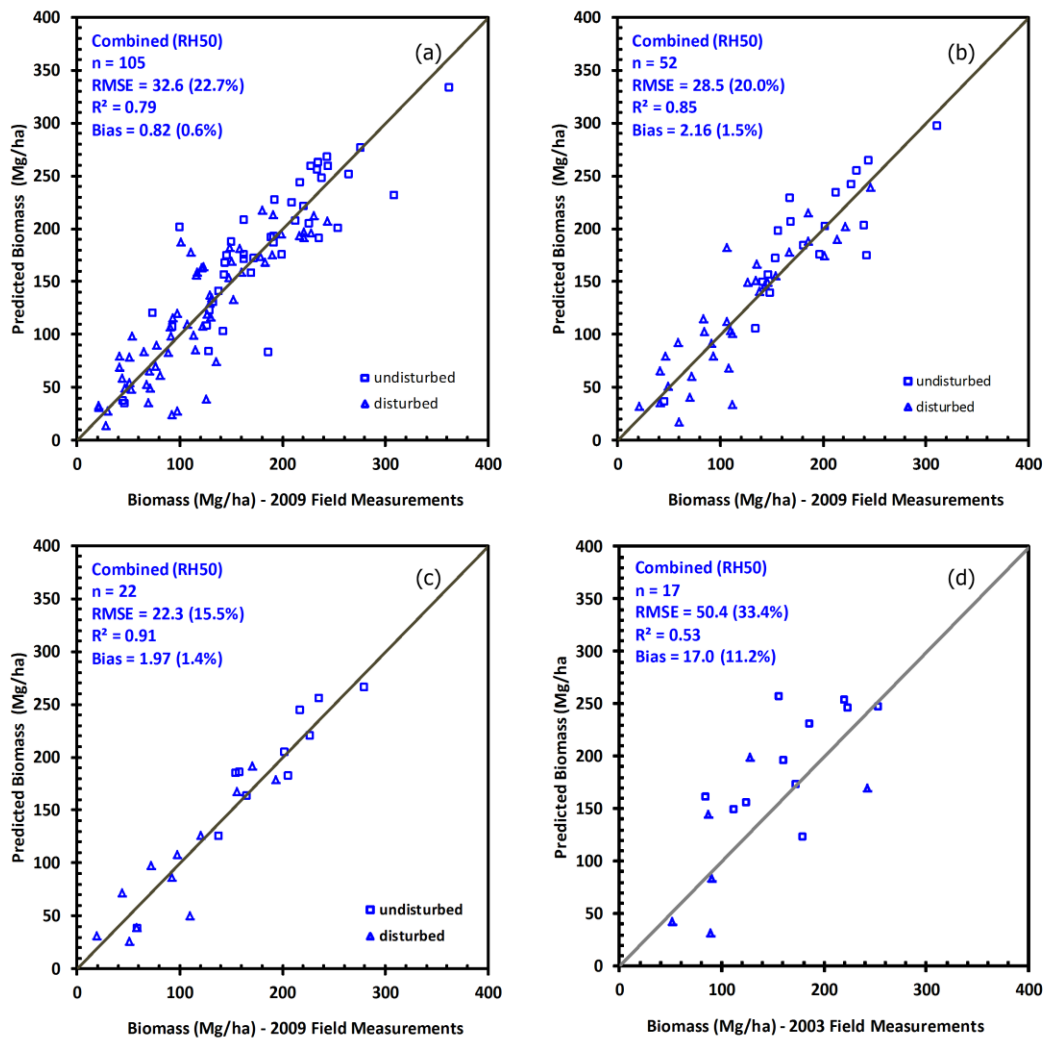
Figure 2-8. Evaluation of combined footprint-level RH50 model in 2009, with the solid line for y=x. (a) 0.25 ha field plots; (b) 0.5 ha field plots; (c) 1 ha field plots in 2009; (d) 0.5 ha field plots in 2003. All results were from the application of combined model. Rectangle dots represent the undisturbed points, and triangle dots represent the disturbed points.
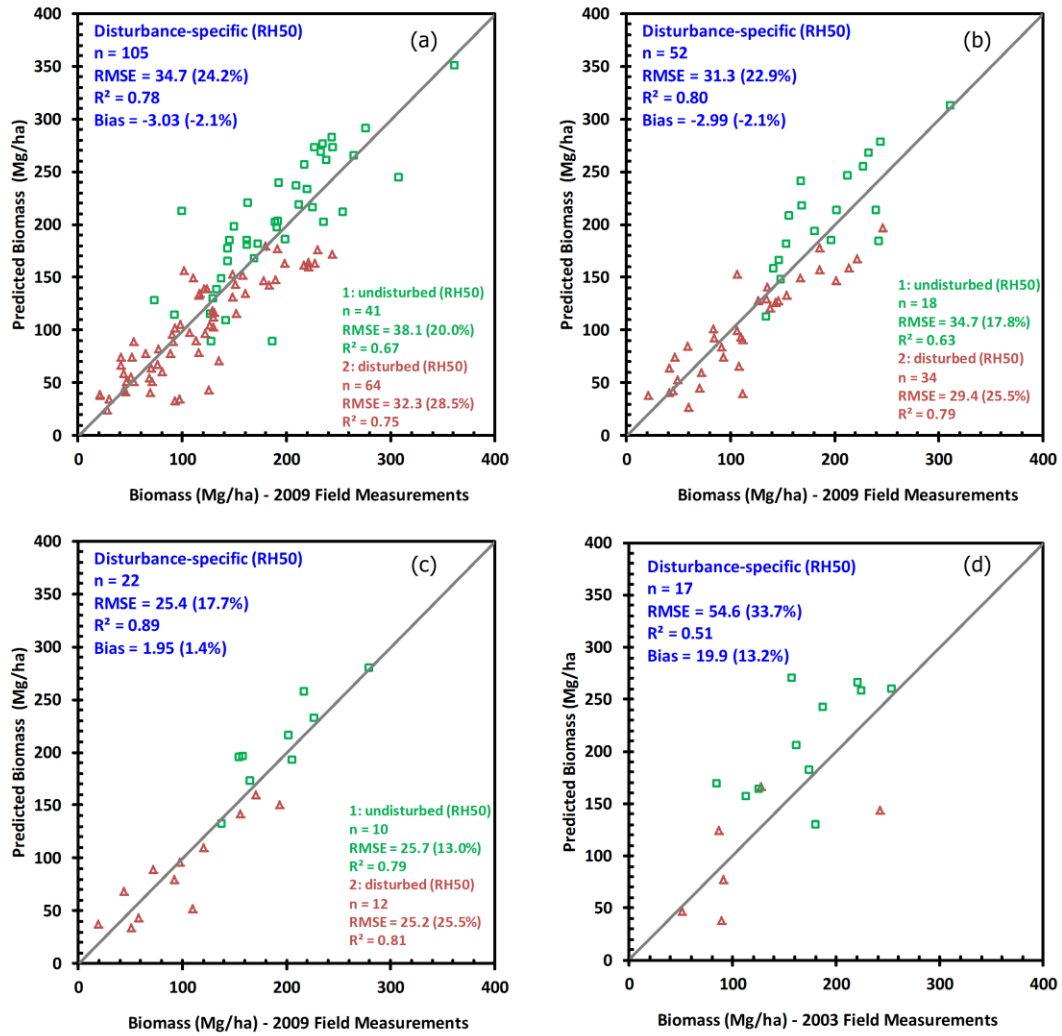
Figure 2-9. Evaluations of disturbance-specific RH50 footprint-level biomass model, with solid line for y=x. (a) 0.25 ha field plots; (b) 0.5 ha field plots; (c) 1.0 ha field plots in 2009; (d) ~ 0.5 ha field plots in 2003. Different colors indicate the different models were used: rectangle dots (green) represent the undisturbed group, and triangle dots (red) represent the disturbed group.

Figure 2-9 shows the scatter plots of predictions versus field measurements from the best disturbance-specific footprint-level models at various plot sizes. The RH50 model has the best performance at all plot levels and in both 2009 and 2003. Again, there is almost no bias (less than ±2.0%) observed for predictions in 2009 and a less than +13.5% bias in 2003. Similar to the combined RH models, the disturbance-specific models overestimated the biomass for 2003.

Even though the statistical tests of prediction models at footprint level showed significant effect of disturbance, the evaluation of the predicted biomass demonstrated that the disturbance effect is reduced in a larger sampling area. For further biomass mapping and change detection the combined RH50 model was used and the biomass maps were generated at 1.0 ha (100 m) spatial resolution.

2.4.3 Biomass mapping from LVIS data

Figure 2-10 shows the biomass maps from LVIS data for year 2003 and 2009 were produced using the RH50 regression model and were averaged to 1.0 ha spatial resolution. The biomass ranges up to 350 $Mg \cdot ha^{-1}$, with a color of orange (0-50 $Mg \cdot ha^{-1}$) to dark green (>300 $Mg \cdot ha^{-1}$) indicates an increase of biomass. Grey color represents the areas of no data and non-forest. The overall similar patterns of biomass can be seen from both years of 2003 and 2009. As shown in Figure 2-10, the north-west region with biomass less than 100 $Mg \cdot ha^{-1}$ at HF site in 2009 was mostly caused by select-cut (*i.e.*, shelter-wood harvest, removed large trees accounting for about 1/3 of the basal area) and strip-cut (*i.e.*, systematically removed stems in rows). The undisturbed forests in the center of the map (outlined by pink polygon in dotted

39

line) were with high value of biomass (>300 Mg·ha^{-1}). For PEF in 2003 and 2009, high biomass regions were observed in the south and west region of the map. Low biomass regions with less than 50 Mg·ha^{-1} in the north-east were the woody wetland along the Penobscot River.

2.4.4   Biomass change mapping

Figure 2-11 (a) and (b) shows the changes of biomass (green to red color) from 2003 to 2009 at the two study sites, corresponding to the disturbance maps of Figure 2-11 (c), (d), and (e). In addition, a confidence interval (CI) was applied for the predictions from LVIS data in 2003 and 2009 as shown in Figure 2-12, where only predicted values within the 95% CI were kept (Figure 2-12h). It can be seen that most of the changes are consistent with the forest disturbance patterns detected by the LTSS-VCT product and the historical management map.
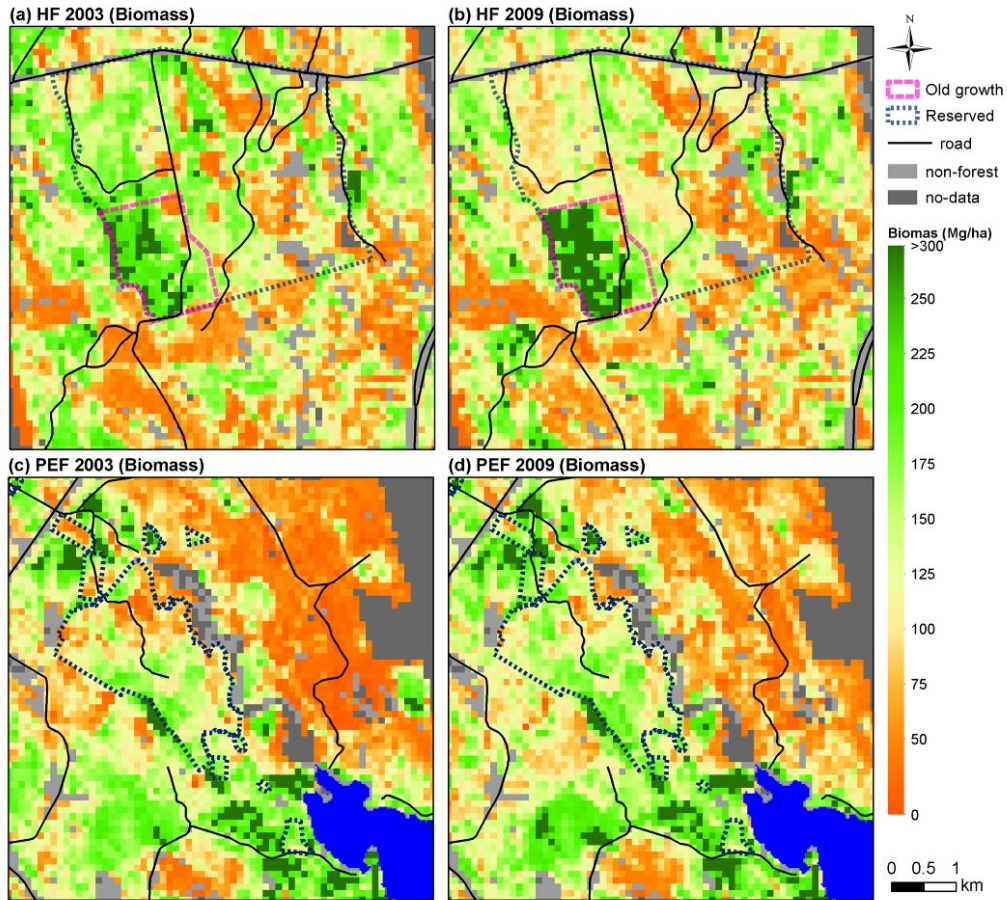
Figure 2-10. Biomass map for HF site (a) and (b), and PEF site (c) and (d) in 2003 and 2009 at 1.0 ha level by the combined RH50 models. A color of orange to dark green indicates an increase of biomass. At HF site, pink polygon is near matured old-growth forest; and dark blue polygon is the outline of reserve area.

41
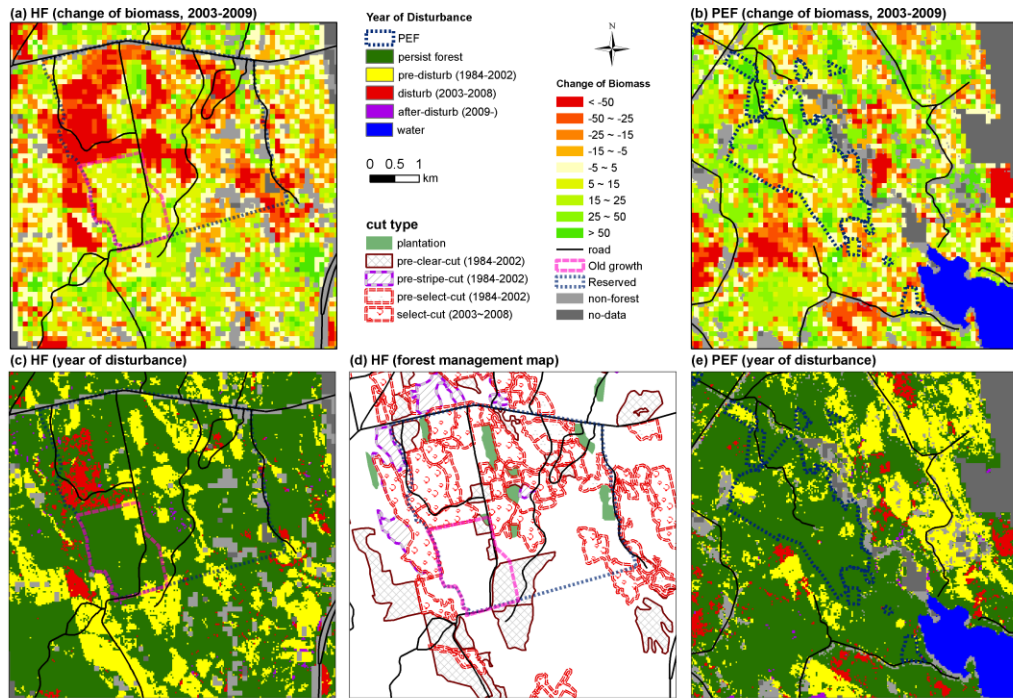
Figure 2-11. Change in biomass for HF site (a) and PEF site (b) from 2003 to 2009 at 1.0 ha level by the combined RH50 models. The (c) and (e) are the years of disturbances: disturbances prior to 2002 (yellow), between 2003 and 2008 (red), and after the 2009 (purple). (d) is the forest management map of HF created from information from private owner (international paper company) and Google images. The plantation is represented with green solid filled polygons. The clear-, select-, and strip-cuts prior to 2002 are outlined with dark red solid lines with gray cross-hatched pattern, purple long dotted lines, and red double long dashed lines with gray stripes, respectively. The select-cut during 2003 to 2008 is outlined by red double dashed lines with irregular dots. At HF site, pink polygon is the near matured forest; and dark blue polygon is the outline of reserved area. The select-cut during 2003 to 2008 is outlined by red double dashed lines with irregular dots.

At HF site, biomass changes in the undisturbed near-mature forests (center of the map, highlighted by pink polygon in dotted line) were mostly positive (5 to 15 Mg·ha^{-1}) or near neutral (-5 to 5 Mg·ha^{-1}). The average annual biomass accumulation from undisturbed forest and regrowth is +4.4 Mg·ha^{-1}. The area surrounding this undisturbed forest shows strong negative change (in red, represent < -50 Mg·ha^{-1}). Most areas along the roads are the degraded forests from select-cut between 2003 and 2008 (filled irregular dots) as shown in Figure 2-11 (d). The average annual biomass reduction rate from forest disturbance is -7.0 Mg·ha^{-1}. Several patches highlighted with yellow in Figure 2-11 (c) show an increasing biomass during 2003 to 2009, due to the forest regrowth after clear-cut in the 1980s or strip-cut in the 1990s. At PEF site, patches of strong negative biomass changes with red color in Figure 2-11 (e) were sparsely distributed over the study region. Most of them were detected by LTSS-VCT disturbance product in Figure 2-11 (d). The average annual biomass reduction rate from forest disturbance is -6.2 Mg·ha^{-1}. The woody wetlands with low biomass along the Penobscot River were regrowth from clear-cut prior to 2002. The average annual biomass accumulation from regrowth is +4.4 Mg·ha^{-1}.

Regression model developed in 2009 were applied to two years LVIS data, and change in biomass were mapped from 2003 to 2009 (Figure 2-12). Prediction intervals (*i.e.*, 95% confidence interval) were calculated for estimated biomass in 2003 and 2009, and cells with overlapped predictions were masked out (Figure 2-12 d) as neutral (statistically indistinguishable from zero). A detailed comparison is given for HF site. The patterns of biomass change (Figure 2-12 h) are consistent with VCT product (Figure 2-12 e) and local forest management (Figure 2-12 d), where most of

the near matured area as neutral and positive change in biomass are mostly from

plantation as well as forest recovery after disturbance (*i.e.*, disturbed between 1984

and 2002).
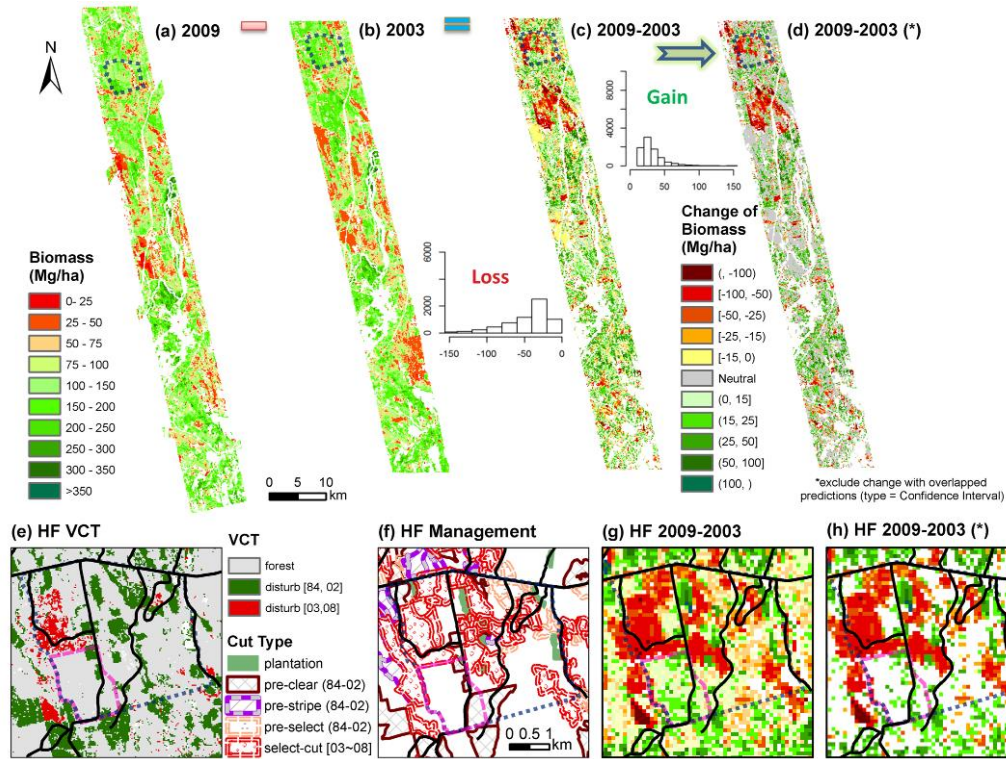
Figure 2-12. Changes in biomass from LVIS 2003-2009. The (a) and (b) are biomass maps at 1.0 ha level by the combined RH50 models using all LVIS from 2003 to 2009footprints in Maine, non-forest cells are maksed out (in white). (c) is the change in biomass from 2003 to 2009, and (d) is the change map that masked out cells (in grey) where in two years overlapped in predictions (95% confidence interval). (e) ~ (h) are the zoom-in maps over HF sites, where (e) is the year of disturbance: disturbance between 1984 and 2002 (dark green), disturbance between 2003 and 2008 (red), and non-changed forest (grey); (f) is the forest management of HF; (g) is the HF biomass change map from 2003 to 2009; and (h) is the map excluding cells with overlapped predictions in 2003 and 2009, respectively.

2.5   *Discussion*

Our results highlight four important issues concerning biomass mapping from waveform LiDAR: (1) the feasibility of the prediction model at the LiDAR footprint, (2) the effect of forest disturbances on the biomass prediction model, (3) the effect of map scale and footprint density on the biomass estimation, and (4) the application of the footprint-level model for biomass change detection.

2.5.1   Prediction model at LiDAR footprint-level

The results in our study sites demonstrate that LiDAR footprint-level models could be developed and applied to map biomass, with 91% explanation of total variance, a RMSE of 22.4 Mg·ha^{-1} (15.6%) for the combined RH50 model at 1.0 ha plot-level. Two main factors lead to this conclusion. First, the accurate location provided by DGPS and high quality LVIS data reduced the geolocation errors. On the one hand, in our study, all footprint-level field measurements and sampling plots at HF in 2010 and 2011 and at PEF in 2009 were located using DGPS with a measurement error of 0.5-3.0 m (best case was 0.5-1.0 m). On the other hand, increased accuracy of the geolocation has been reported for the LVIS product released after 2003 by improved post data processing. Reprocessed 2003 LVIS data which using the same waveform analysis method are more consistent with 2009 LVIS data. Therefore geolocation errors are mostly avoided for the data used in the study. Secondly, the footprint size of LVIS facilitates the application of models at the footprint-level. LVIS data has a 20m diameter footprint, which generally corresponds

to the largest tree crowns, and thus can capture canopy characteristics *(Dubayah and Drake, 2000)*.

2.5.2   Disturbance effect

Footprint-level regression models differed between undisturbed and disturbed forest, different species composition. Previous study *(Anderson et al., 2006, 2008)* has mentioned the effect of species composition to the biomass estimation. Forest disturbances change the spatial structure as well as the species composition. The statistical tests reveal a significant difference at 95% confidence level between models for the disturbed and undisturbed forests. The disturbance-specific models performed slightly better for biomass estimation than the combined model (Table 2-3). But the evaluations results (Table 2-4 and Table 2-5) at different plot-levels from 0.25 ha, 0.5 ha to 1.0 ha show almost the same biomass estimation accuracies for the combined and disturbance-specific models. The evaluation of biomass estimation shows that the combined RH50 model overpasses the combined RH75 model, and the disturbance-specific RH50 and RH75 models regardless of scale. These results weaken the importance of introducing disturbance factor into footprint-level model. It is reasonable for the effect of disturbance weaker at plot levels because averaging of LVIS footprints in plot will reduce the disturbance effect. The combined model was used for biomass mapping in this study. However, we still recommend considering the disturbance effect in area with more complicated species composition.

On the other hand, it is important to note the potential error that can be introduced by the classification of disturbance from LTSS-VCT. Based on field notes, recent Google Earth imagery and LTSS-VCT product, we are confident in the

46

accurate classification of disturbance for our field samples. For a broader region more efforts are need to guarantee the accuracy in identification of disturbance. Careful application of a disturbance dataset is recommended when conducting forest biomass change assessments.

2.5.3   Map scale and footprint density

Biomass maps were produced by application of prediction models developed at the footprint-level (~0.03 ha; 20 m diameter circle plot) and re-sample the footprint biomass into map grids. The field biomass samples at different plot-levels (0.25 ha, 0.5 ha, and 1.0 ha; rectangular plot) served as independent data for evaluation of the accuracies of biomass maps.

Figure 2-13 shows the RMSE (%) of the biomass prediction models developed at footprint level, and the evaluations at 0.25 ha, 0.5 ha and 1.0 ha plot-level. We can see a decreasing trend for RMSE (%) with increasing size of plots. At 1.0 ha plot, the RMSE (%) from disturbance-specific and combined models is similar and is much lower than at other smaller plot levels. Recent studies *(Frazer et al., 2011; Mascaro et al., 2011)* have indicated that 1.0 ha plots could capture biomass with low and stable errors close to 10%. Therefore, we used a 1.0 ha scale for the biomass mapping and change detection using the combined RH50 models.
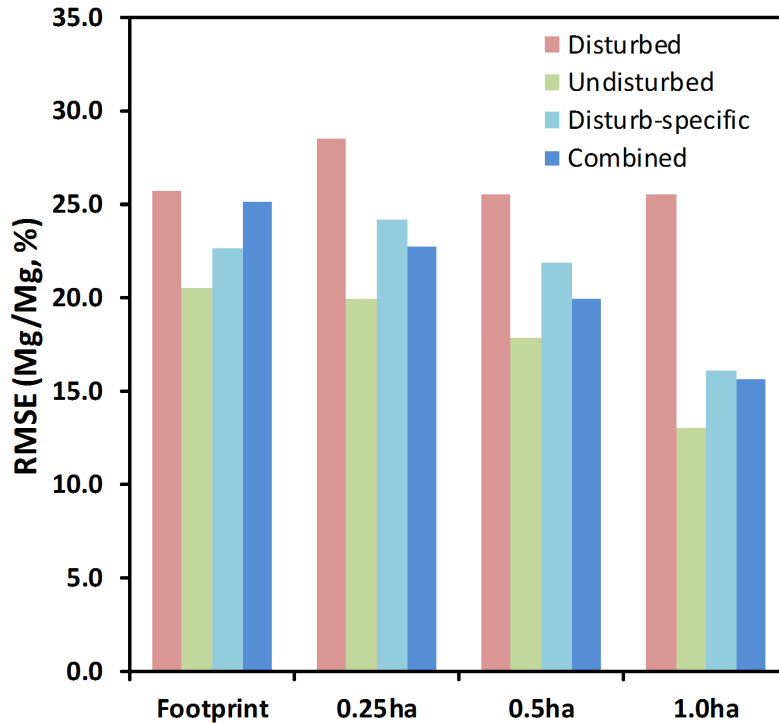
Figure 2-13. RMSE (%) of the RH50 biomass prediction models developed at footprint-level and the evaluations at 0.25, 0.5 and 1.0 ha scales. Bars from left to right represent best models for disturbed (pink), undisturbed (green), disturbance-specific (light blue), and combined (dark blue).

Figure 2-14 shows the sensitivity of (a) RMSE (%) and (b) R^2 to the footprint density (pt·ha^{-1}) from 0.25 ha, 0.5 ha and 1.0 ha plot-level. With the increasing of footprint density, there is a decreasing trend for RMSE (%), and an increasing trend of R^2 at 0.25 ha, 0.5 ha and 1.0 ha plot-levels. At all three plot-levels, a critical inflection point where point density equals to 16 pt·ha^{-1} was observed regardless of scale. The relationship between RMSE (%) and point density become stable after reaching this inflection point. This is the same to the trend of R^2. Therefore, optimal point density of 16 is suggested for a high quality of biomass estimation at 1.0 ha plot-level. This is feasible because the average footprint density within our field

sampled plots was over 50 pt·ha^{-1} with a 20 m nominal spacing both along and across track.
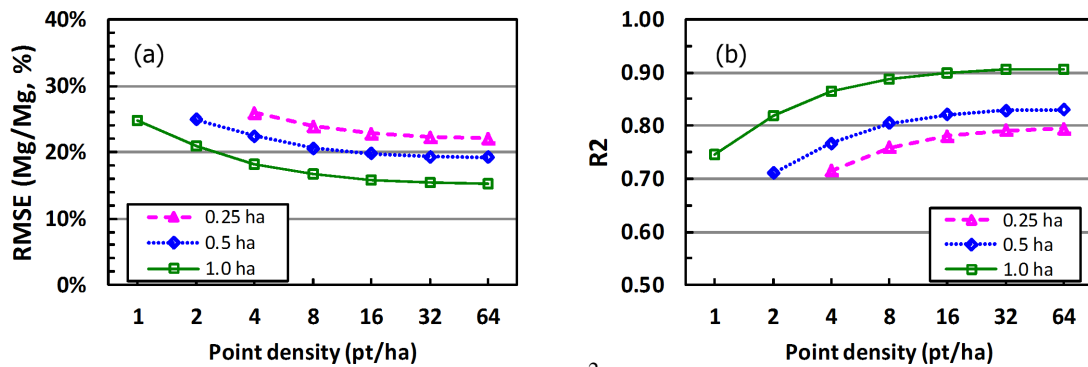
Figure 2-14. Sensitivity of RMSE% (a) and R^2 (b) to the density of footprints within the plot (pt ha^{-1}) at 0.25 ha, 0.5 ha and 1.0 ha plot-levels; RMSE (%) and R^2 values were from the combined RH50 footprint-level biomass prediction model.

2.5.4   Application of footprint-level model for biomass change mapping

The footprint-level models were developed using 2009 data in this study and then applied to both 2009 and 2003 data for mapping forest biomass and its change. Repeat acquisition of LiDAR data has been used for detecting changes of canopy height and biomass. *Dubayah et al. (2010)* recommended using the relationship between the biomass change and change in LVIS-derived range-based forest canopy height metrics for biomass change studies to avoid using two sets of biomass estimation models. However, due to limited co-incidence field measurements at either footprint or plot level, we couldn't develop the similar equations. Instead, footprint-level plots were selected to develop a uniform biomass equation and then this equation was applied to LVIS data in both 2003 and 2009. In addition to the forest spatial structural variations from disturbances, other factors such as species composition, seasonal changes of leaf area index, reflectance of ground surface, etc. will also affect the LiDAR waveform metrics and the biomass prediction model. This

should be considered in applying prediction model developed at a place at certain time to other places or data acquired at different seasons. The LiDAR waveform data used in this study were acquired using the same instrument (LVIS) and at the same season (August) in 2003 and 2009. The processing of the LVIS data is also the same for 2003 and 2009 data. Therefore the common relationship between biomass and LiDAR waveform metrics should keep consistent from 2003 to 2009.

2.6   Conclusion

1) Prediction model at the scale of individual LVIS footprints is reliable when the geolocations of the measured footprints were determined by DGPS with a best accuracy of 0.5-1.0 m.

2) The differences between biomass prediction models for disturbed and undisturbed forests were statistically significant (P<0.001) at the scale of footprint, and the disturbance-specific models performed slightly better (R^2=0.89, RMSE=27.9 Mg ha^{-1}, and relative error of 22.6%) than the combined model (R^2=0.86, RMSE=31.0 Mg ha^{-1}, 25.1%).

3) The evaluation using field plot data showed that the predictions of biomass were improved markedly with the increase of plot sizes from 0.25 ha to 1.0 ha and that the effect of disturbance was not strong. At 1.0 ha plot-level, both disturbance-specific and combined models agreed well with field estimates (R^2=0.91, 23.1 Mg·ha^{-1}, 16.1%; and R^2=0.91, 22.4 Mg·ha^{-1}, 15.6%).

4) Sensitivity analysis on levels of variation and error to footprint density suggests that a certain density of LVIS footprints is required for biomass mapping. The errors

were minimized when footprint coverage approached about 50% of the area of 1.0 ha plots (16 footprints).

5) By applying the footprint-level models developed from 2009 LVIS data to both 2009 and 2003 LVIS data, the change in biomass from 2003 to 2009 could be assessed. The average annual biomass reduction rate from forest disturbance at two sites is -7.0 Mg·ha^{-1} and -6.2 Mg·ha^{-1}, the average annual biomass accumulation from regrowth is +4.4 Mg·ha^{-1} and +5.2 Mg·ha^{-1}, respectively.

Estimating biomass dynamics over relatively short time scales is a difficult task, yet is central to obtaining a better understanding of the effects of disturbance and subsequent regrowth on the terrestrial carbon cycle. There is additionally a strong and growing need to develop effective mapping and monitoring in support of climate treaty frameworks such as REDD+ *(Goetz and Dubayah, 2011)*. The work presented here gives some examples of LiDAR remote sensing approach to this problem.

Change studies using LiDAR remote sensing are also dependent on having sufficient LiDAR coverage to develop spatially meaningful maps. Ideally such coverage would be wall-to-wall, but practically that may not be achievable nor may it be entirely necessary. Our errors were minimized when footprint coverage approached about 50% of the area of 1.0 ha plots (16 footprints) with no improvement beyond that. This is a particularly important point when considering monitoring from space-based LiDAR, which is unlikely to have swath-mapping capability in the near term.

While our experiment showed improvement in biomass prediction when disturbance was included, the results were not compelling. We doubt that this conclusion is generalizable beyond the present study. While canopy metrics must implicitly include the effects of disturbance as reflected in height, other factors also control height, most notably climate and edaphic factors. Thus more work is needed to untangle the relationships between these factors, disturbance, and their manifestation in height metrics. That said, the fusion of Landsat disturbance products with time series of LiDAR data is a powerful approach to quantifying landscape level changes in vegetation structure and will certainly be exploited with increasing frequency in future studies.

Ultimately, there is distance to travel before we can confidently monitor biomass and canopy structure dynamics at policy-relevant scales with the requisite accuracy in a consistent and transparent framework from remote sensing. LiDAR remote sensing is so new that only now are we able to evaluate data sets with sufficient time intervals between them, and for which contemporaneous field estimates are available. We anticipate that as more investigations undertake such studies, rapid progress will result in this important capability.

Chapter 3 Sensitivity of Multi-Source SAR Backscatter to Changes in Forest Aboveground Biomass[2]

3.1   *Introduction*

The carbon budget of terrestrial ecosystems contains large uncertainties at

both global and regional scales *(Goetz and Dubayah, 2011)*. Aboveground biomass

(AGB, hereafter biomass) stock from forest represents an important component of the

global carbon cycle and related carbon policy *(Houghton et al., 2009)*.

Anthropogenic disturbance including deforestation and forest degradation due to

management has led to significant changes in biomass and thus the carbon budget

(Hall et al., 2011). However, the loss of carbon due to deforestation and forest

degradation, and the gain from post-disturbance recovery have not been sufficiently

assessed. The use of active remote sensing techniques such as Synthetic Aperture

Radar (SAR) is a promising approach for measuring and monitoring the spatial and

temporal variation of forest carbon stock *(Hall et al., 2011; Kasischke et al., 1997; Lu,*

2006).

Imaging with SAR has advantages over optical imagery in its capacity to

penetrate clouds, rain, smoke, and haze, which are known problem for optical sensors.

The ability to penetrate the forest canopy makes it possible to retrieve the forest

structure as a function of backscatter mechanisms *(Kasischke et al., 1997)*. Generally,

studies have reported that SAR backscatter is more sensitive to canopy biomass

(especially tree trunks) at longer wavelengths. Full polarimetric SAR (PolSAR)

---

[2] The presented material has been previously published in: Huang, W., Sun, G., Ni, W., Zhang, Z., Dubayah, R. (2015). Sensitivity of Multi-Source SAR Backscatter to Changes in Forest Aboveground Biomass, *Remote Sensing*. 7(8): 9587-9609; doi: 10.3390/rs70809587.

provide four combinations of transmitted and received polarizations: co-polarized

bands HH (horizontal transmitted and horizontal received) and VV (vertical

transmitted and vertical received), as well as cross-polarized bands HV (horizontal

transmitted and vertical received) and VH (vertical transmitted and horizontal

received). Longer SAR wavelengths such as P- (30-100 cm) and L- (15-30 cm)

bands penetrate farther into the forest canopy and capture more vertical structure than

C- (4.8-7.7 cm) and X- (2.8-5.2 cm) bands, while HV backscatter from dual-

polarization (e.g., HH, HV) or full-polarization (*i.e.*, HH, VV, HV, and VH) are more

sensitive to woody biomass.

A series studies suggested that a widely applicable relationship exists between

biomass and backscatter from L-band SAR for woody vegetation with lower levels of

biomass ($\leq$150 Mg·ha^{-1}) in tropical *(Collins et al., 2009; Englhart et al., 2011;*

Mitchard et al., 2011a; Mitchard et al., 2009b; Pope et al., 1994; Saatchi et al.,

2011b), temperate and boreal biomes *(Botkin and Simpson, 1990; Kurvonen et al.,*

1999; Ranson et al., 1995; Sandberg et al., 2011). Both airborne and spaceborne

systems were involved in these studies. These including airborne instruments such as

AIRborne SAR (AIRSAR) and Uninhabited Aerial Vehicle SAR (UAVSAR)

developed by NASA, Experimental-SAR (E-SAR) operated by the German

Aerospace Center (DLR), as well as spaceborne instruments such as Spaceborne

Imaging Radar-C and X-B and SAR (SIR-C/XSAR), and Phased Array type L-band

SAR (PALSAR) on board the Advanced Land Observing Satellite (ALOS). *Ranson*

et al. (1995) investigated the use of multi-frequency, multi-polarization and multi-

season image data from SIR-C/XSAR to map forest cover type and estimate

aboveground biomass for a Boreal Ecosystem-Atmosphere Study (BOREAS) site in Saskatchewan, Canada. *Santos et al. (2002)* utilized the L-HH channel of JERS-1 data in tropical forest-savanna contact zones, and found that the logarithmic and sigmoid functions were adequate to explain the SAR backscatter as a function of forest biomass. *Collins et al. (2009)* indicated that the L-HV channel of polarimetric SAR backscatter intensity from AIRSAR was best suited (R^2=0.92) for modeling biomass (both above- and below-ground) of the tropical savannahs in North Australia. *Mitchard et al. (2009a)* examined the relationships between field-measured biomass at four study sites in Cameroon, Uganda and Mozambique and data from ALOS/PALSAR, and found that biomass estimates based on these relationships were highly significant and similar among sites. *Sandburg et al. (2011)* explored the relationship between SAR backscatter from E-SAR data and forest biomass in southern Sweden, and found that for L-band data the best results were obtained from HV-polarized backscatter. *Robinson et al.(2013)* studied the variation in field estimated biomass at different scales (0.0625, 0.25, 0.5, and 1.0 ha) in a temperate to boreal transitional region (Howland, ME), and found that the cross-polarized HV had the highest sensitivity to field estimated biomass (R^2=0.68).

Nevertheless, a number of important factors can affect the relationship between radar backscatter and forest biomass, including change in forest structure *(Dobson et al., 1995)*, radar incidence angle *(Sun et al., 1991; Wang et al., 1993)* and look direction *(Sun and Ranson, 1998)*, surface and environmental conditions (*i.e.*, soil moisture) *(Harrell et al., 1997; Kasischke et al., 2011)*, trunk dielectric properties *(Way et al., 1991)* and saturation *(Dobson et al., 1992; Kasischke et al., 1997; Ranson*

and Sun, 1997). Backscatter from vegetated areas depends on a combination of canopy structure and underlying surface conditions *(Ranson and Sun, 2000).* The former is related to water content of the vegetation, while the latter is linked to soil moisture (SM) changes. Both (vegetation and soil) are affected by environmental factors such as temperature and moisture that will affect the dielectric constants of the target. These effects (*i.e.*, temperature and moisture) need to be removed before any further analysis of changes caused by forest disturbances.

However, few studies have been focused on analyzing sensitivity of multi-source SAR backscatter to changes of forest biomass after forest disturbances. *Ranson and Sun (2000)* reported up to a 7 dB change in backscatter coefficient between frozen and non-frozen conditions and suggested multi-year comparisons under similar temperature conditions should be made such during in the summer growing season. In addition, saturation in SAR backscatter varies among different bands. *Dobson et al. (1992)* indicated biomass saturation levels of ~200 Mg·ha^{-1} and ~100 Mg·ha^{-1} for P-band and L-band polarimetric SAR (PolSAR), respectively. *Imhoff (1995)* reported that the radar signal saturation was ~100 Mg·ha^{-1} for the P-band, ~40 Mg·ha^{-1} for the L-band, and ~20 Mg·ha^{-1} for the C-band by comparing SAR backscatter and forest biomass relationships over a tropical broadleaf evergreen forest in Hawaii and coniferous forest stands in North America and Europe. *Ranson and Sun (1997)* indicated that SAR backscatter from AIRSAR and SIR-C/XSAR could provide estimates of biomass up to ~150 Mg·ha^{-1} with an average of 97 Mg·ha^{-1}. *Lucas et al. (2010)* studied the relationship between PALSAR data and biomass in Australia, and concluded that PALSAR data acquired when surface moisture and

rainfall are minimal allow better estimation of the biomass of woody vegetation and that retrieval algorithms ideally need to consider differences in surface moisture conditions and vegetation structure.

This chapter will describe the analysis of the sensitivity of multi-sensor and multi-temporal SAR signatures to changes in forest biomass. The objectives were to investigate: 1) a procedure to reduce the distortion in SAR backscatter caused by incidence angle and soil moisture; 2) the feasibility of cross-image calibration between multi-temporal and multi-sensor SAR data; and 3) the possibility of applying normalized backscatter to detect changes in biomass due to forest disturbance and post-disturbance recovery. This chapter is organized as follows. First, the study area and data are described. Then the factors that influence changes in SAR backscatter are described and discussed. A cross-image normalization method is proposed to reduce the offset between multi-temporal and multi-sensor data. The performance of our correction is evaluated and applied to selected stands after forest disturbance. A biomass-backscatter regression model is developed from field measurements, and applied to map changes in forest biomass in the study area. Finally, the significance and limitations of the results are discussed and conclusions are drawn.
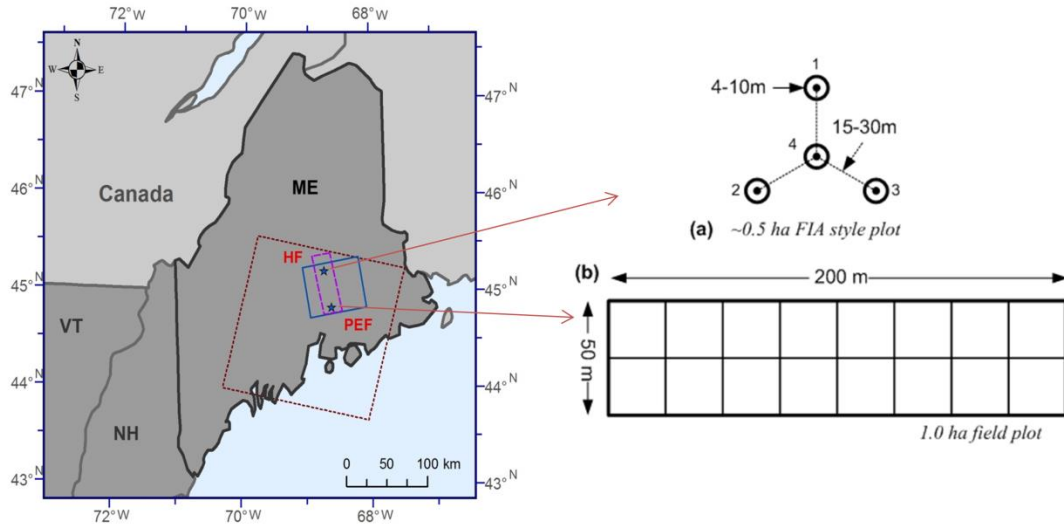
Figure 3-1. Map of study sites, and coverage of Landsat ETM+ scene (red dashed line, p011/r029), ALOS PALSAR FBD scene (blue solid line) and PLR scene (purple dashed line). (a) 0.5 ha FIA style plot in 1992 and 2003, (b) 1.0 ha field plot in 2009.

3.2.1   SAR data

All SAR data used in this study were collected during middle April to early October and by systems operating at the L-band (23.6 cm wavelength or 1.3 GHz frequency). Key parameters for SAR data used in this study site (HF, Figure 3-1) are given in Table 3-1. Airborne Synthetic Aperture Radar (AIRSAR) L-band data with full polarizations (*i.e.*, HH, VV, HV, VH) and multi-look angles (*i.e.*, target at 25 °, 35 °, 45 °) were collected in 1989 and 1994. Uninhabited Aerial Vehicle SAR (UAVSAR) data were gleaned for the study area on August 5th, 6th, 7th and 14th in 2009, with looking angle ranges from 20 ° to 60 °, and headings of 167° and 347°. Meanwhile, Spaceborne Imaging Radar C- and X-Band SAR (SIR-C/XSAR) data with full polarizations at L-band and C-band were collected in April and October 1994. Phased Array type L-band SAR (PALSAR) on board the Advanced Land

Observing Satellite (ALOS) is an enhanced version of JERS-1 SAR instruments

launched in 2006 with a 46-day recurrent period. PALSAR data were collected for

study area from 2007 to 2010 with fine beam dual mode (FDB: HH, HV) and

polarimetric mode (PLR: HH, HV, VH, VV). The Japan Space Exploration Agency

(JAXA) has reported a geometric accuracy of 70 m and a radiometric accuracy of

0.22 dB for measurements done in the Amazon forest areas *(Shimada et al., 2009)*.

Detail information about the SAR data selected for this study are listed in Table 3-2,

including acquisition date, center incidence angle, and environmental conditions such

as temperature and precipitation.

Table 3-1. Key instrument parameters of SAR system in this study

Parameter	AIRSAR	UAVSAR	SIR-C/ XSAR	JERS-1	PALSAR FBD	PALSAR PLR
Platform	Airborne	Airborne	Spaceborne	Spaceborne	Spaceborne	
Available date	1994	2009	1994	1995, 1998	2007-2010	
Frequency	1.26GHz	1.26GHz	1.26GHz	1.3 GHz	1.27 GHz	
Polarization	HH, HV, VH, VV	HH, HV, VH, VV	HH, HV, VH, VV	HH	HH, HV	HH, HV, VH, VV
Look angle	25-64	25-65	17-63	35	10-50	
Swath width	15km	16km	15km	75km	70km	30km
Pixel size	10m	6m	12.5m	18m	20m	30m

*Pixel size for multi-looked ground-projected product. FBD=Fine beam dual; PLR=Polarimetric. Technical specs from https://www.asf.alaska.edu/sar-data

Table 3-2. SAR data selected for sensitivity analysis

Sensor	Scene id	Acquisition date	Pixel size* (m)	Incidence angle# (∘)	Environmental conditions			
					Temperature (℃)	Precipitation (mm)		
						3day	7day	14day
SIR-C /XSAR	PR12331	04/13/1994	12.5	31.7	T ~ 5.5 ℃	17.3	42.1	50.9
SIR-C /XSAR	PR47494	10/04/1994	12.5	31.7	T ~ 10.1 ℃	0	0.2	76
AIRSAR	/	09/02/1989	10	35.0	T ~ 10.1 ℃	16.8	18.6	27.6
AIRSAR	CM6221	10/07/1994	10	35.0	T ~ 10.1 ℃	0	0.2	76
UAVSAR	16702_ 09054_016	08/05/2009	6	48.0	T ~ 21.6 ℃	11.5	49.6	94.4
PALSAR /FBD	ALPSRP 191680890	08/30/2009	20	34.3	T ~ 14.8 ℃	20.4	32	34.2

*Pixel size for the multi-looked ground-projected product. #incidence angles are at scene center; for technical specifications see
https://www.asf.alaska.edu/sar-data

3.2.2   Auxiliary data

Local forest management maps, Landsat derived disturbance maps, and climate data were prepared as referenced dataset for the study site. Specifically, forest management maps were digitized and composited from scanned American Forest Management (AFM) maps for the study site during 1980 to 2011 (Figure 3-2). Three management maps were used: 1) AFM forest property map (1980-2011), 2) Edinburg, and 3) Howland cut map (manage unit map with harvest dates) in 2000 rectified to road map and satellite images with UTM/WGS84 map projection. The products of yearly forest disturbance map from Landsat time series stack vegetation change tracker (LTSS-VCT) *(Huang et al., 2010)* were obtained for the study area (see details in Chapter 2).

In addition, with an AmeriFlux tower in the HF study site, various climate data were collected from 1987 including daily air temperature, total precipitation, wind speed, etc. The soil near the AmeriFlux tower consists with 50.35% sand, 33.75% silt, and 15.9% clay. From autumn of 1999, soil moisture, temperature and salinity were collected by five Hydra-Vitel probes and thermistors buried at depths of ~5 cm, 10 cm, 20 cm, 50 cm, and 100 cm. Figure 3-3 shows the variation of water fraction by content (WFC, %) versus precipitation (mm) in 2009.
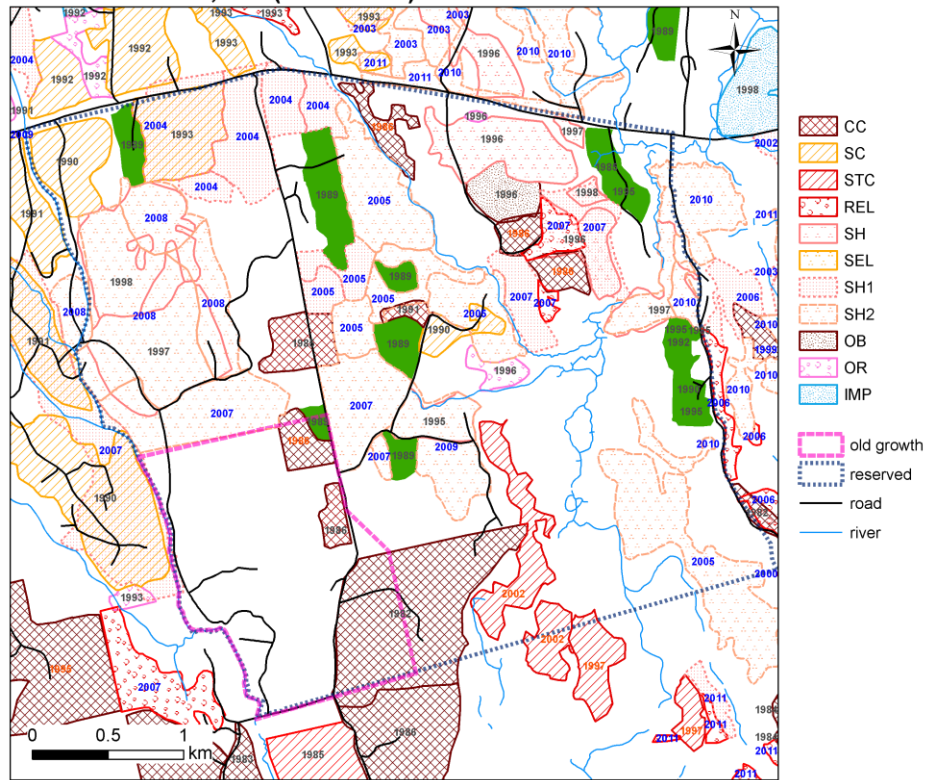
Figure 3-2. Forest management map at the HF study site. Solid dark blue line polygon is the outline of the reserved area, and the solid green line is the near mature forest. PLT=plantation; CC=clear-cut; SC/STC=strip-cut; SEL=select-cut; SH=shelterwood-harvest, 1 and 2 denotes 1st and 2nd entry of shelterwood-harvest; OB/OR= overstory removal; IMP=intensive management plot. Number inside the polygon denotes the year of management.
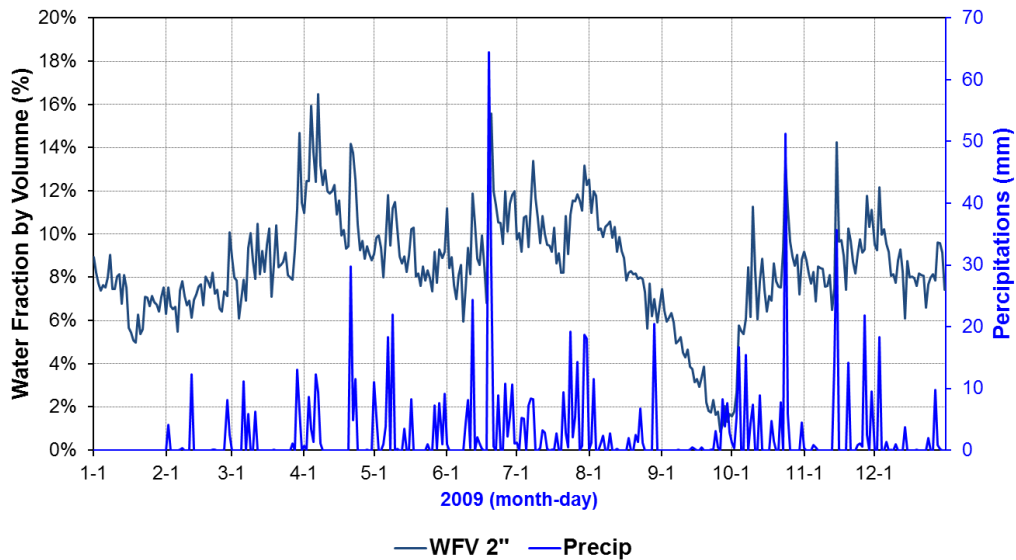
Figure 3-3. Water fraction by Volume (WFV, %) and precipitation (mm) as a function of date. WFV measured at depths of 2 inches (~=5 cm).

3.3   *Method*

Sensitivity analysis in this study includes three steps: incidence angle effect reduction, reduction of soil moisture effect, and determination of sensitivity to forest biomass (Figure 3-4). First, a theoretical model and field measurements are employed to illustrate relationship between SAR backscatter and forest biomass. Then, an empirical model is applied to reduce incidence angle effects on SAR backscatter . The influence of soil moisture on SAR backscatter is analyzed through *in-situ* soil moisture and field biomass studies. A cross-image normalization procedure is proposed to lessen the environmental effect on SAR backscatter. Lastly, the sensitivity of SAR backscatter to biomass is determined using normalized SAR data and field measurements.
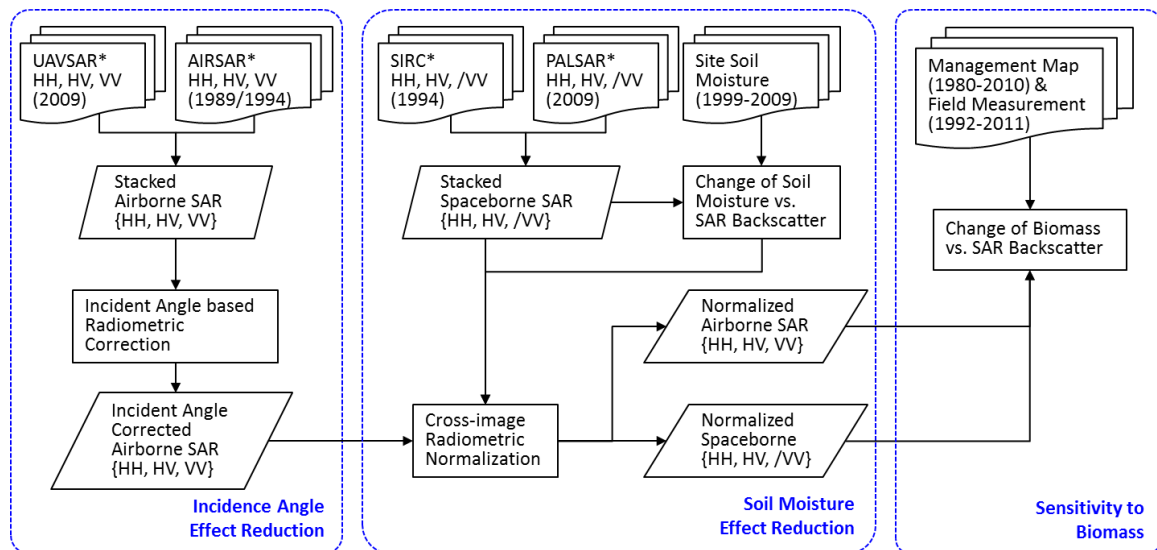
Figure 3-4. Flowchart of SAR data processing and sensitivity analysis.

3.3.1   Sensitivity of SAR backscatter to biomass

We employed a theoretical model to show the sensitivity of L-band SAR backscatter to forest biomass. ZELIG *(Urban, 1990)* is an individual tree-based forest gap model with the ability to simulate the forest ecosystem with complex species composition over a long-term period. Driven by temperature and precipitation data, as well as growth and environmental response parameters of each tree species and soil characteristics *(Levine et al., 1994)*, the model was parameterized for Howland Forest *(Ranson et al., 2001)*. The output of ZELIG model are forest stand parameters, including biomass density, forest height and leaf area index (LAI), and the size of each tree. Then, a radar model that simulated L-band radar backscatter of PolSAR data was implemented based on the output of ZELIG model *(Ni et al., 2013a; Sun et al., 1991)*. A look-up table (LUT) was generated from the physical-based forest backscatter model and was used in this study.

Based on model simulations as well as field measurements, the relationship between SAR backscatter and forest biomass is strong (Figure 3-5). However, the SAR backscatter has a wider dynamic range when the level of biomass density is high. The simulated SAR attributes for co-polarization (HH) and cross-polarization (HV) were plotted as a function of simulated forest biomass from the look-up table (Figure 3-5), where different soil types reflected differences in hydrological condition related to soil moisture and ground roughness *(Levine et al., 1994; Ni et al., 2013a)*. The SAR backscatter data from airborne (*i.e.*, UAVSAR) and spaceborne observations (*i.e.*, PALSAR) were plotted as a function of field measured biomass (Figure 3-5, in blue circles). The figure shows that when biomass increases from 0 to 50 Mg·ha^{-1},

the backscatter ranges from -20 dB to -13 dB (~7 dB) at HV polarization, and from -

14 dB to -9 dB at HH polarization (~5 dB). This is consistent with conclusions in the

aforementioned literatures that HV is more sensitive to forest disturbance than HH;

and that HV is sensitive to structures of post-disturbance tree regrowth, while HH is

more sensitive to moisture content of the soils.
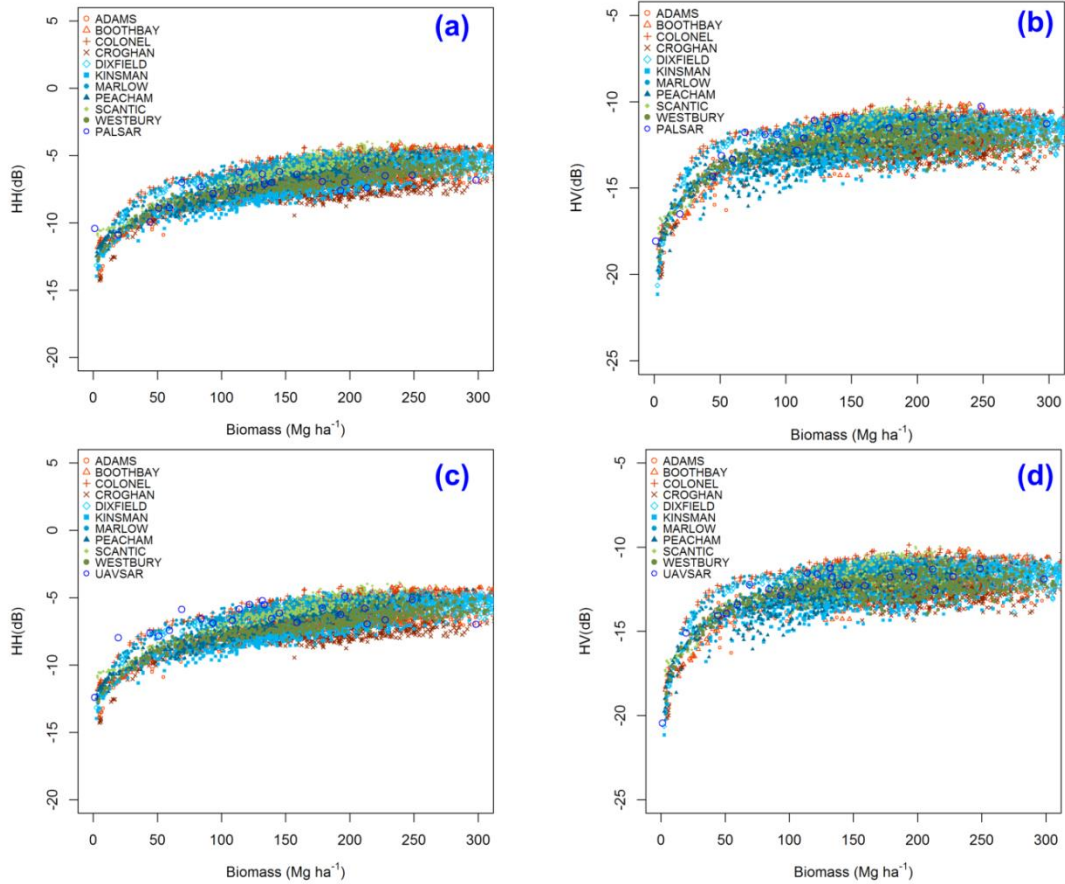
Figure 3-5. SAR backscatter as a function of forest aboveground biomass from model simulation and remote sensing observation. Simulation from ZELIG plotted with (a) PALSAR HH, (b) PALSAR HV, (c) UAVSAR HH, and (d) UAVSAR HV. ADAMS to WESTBURY are different type of soil based on drainage and taxonomic classification (Levine et al., 1994).

The above analysis indicates that changes in forest biomass after disturbance

are detectable from SAR backscatter. However, many factors other than the change

in forest structure and biomass, such as radar incidence angle and surface conditions,

also affect the radar backscattering. The influence of these factors will be discussed in the following sections.

3.3.2   Incidence-angle based correction for airborne SAR backscatter

Numerous studies have indicated that incident angle (IA) lead to changes in backscatter *(Sun et al., 1991; Wang et al., 1993),* and model-based correction was effective in reducing IA influence on SAR backscatter *(Menges et al., 2001; Sun et al., 2002).* Thus for airborne SAR data (AIRSAR and UAVSAR), two set of empirical models are developed for IA correction:

HH and HV polarization: $\sigma^o_{raw} = \sigma^o_c \cdot (\cos\theta / \cos\theta_c)^n$ **Equation 3-1**

VV polarization: $\sigma^o_{raw} = \sigma^o_c \cdot (\theta / \theta_c)^n$

where σ^o_{raw} is the raw backscatter before correction, θ_c is the radar incidence angle at the center of the image, and θ is the local incidence angle, and *n* is the power exponent coefficient with a range of [1, 2] determined by target attributes. The local incidence angle is defined as the angle between the radar line-of-sight and the local vertical with respect to geoid. If topography is gentle (*i.e.*, slope near to zero), then local incidence angle can be assumed equal to incidence angle.

Then, the correction models are applied to all pixels:

HH and HV polarization: $\sigma^o_{corr} = \sigma^o_{raw} \cdot (\cos\theta_c / \cos\theta)^n$ **Equation 3-2**

VV polarization: $\sigma^o_{corr} = \sigma^o_{raw} \cdot (\theta_c / \theta)^n$

where σ^o_{corr} is the corrected radar backscatter coefficients.

3.3.3 Sensitivity of SAR backscatter to soil moisture and cross-image normalization

To study the effect of surface environments such as soil moisture (SM) on changes in SAR backscatter, relationship between SAR signatures and soil moisture for the period of 2007-2010 over the selected stands was analyzed. Based on the forest management map, SAR signatures near the Main AmeriFlux tower (S1, near mature forest with biomass >200 Mg·ha^{-1}) and near the non-forested area (S2, clear-cut with biomass <10 Mg·ha^{-1}) were extracted from PALSAR collected during the growth season (May to October in 2009). The relationship between SAR signatures and soil moisture is analyzed for the period of 2007 to 2010 (Figure 3-6).

A conceptual diagram of the cross-image normalization is shown in Figure 3-6. The existence of radar "saturation" and different mechanisms from soil and canopy vegetation were utilized to conduct the cross-image normalization for multi-temporal and multi-sensor SAR data. Model simulations *(Ni et al., 2013a)* have indicated that SAR backscatter from soil is stronger than that from canopy in low biomass areas (non-forest areas), but weaker in high biomass areas (near mature forest). The objective of the normalization was to produce SAR signatures, acquired from different time and/or by different sensor, with similar patterns with regard to their SAR backscatter- biomass.
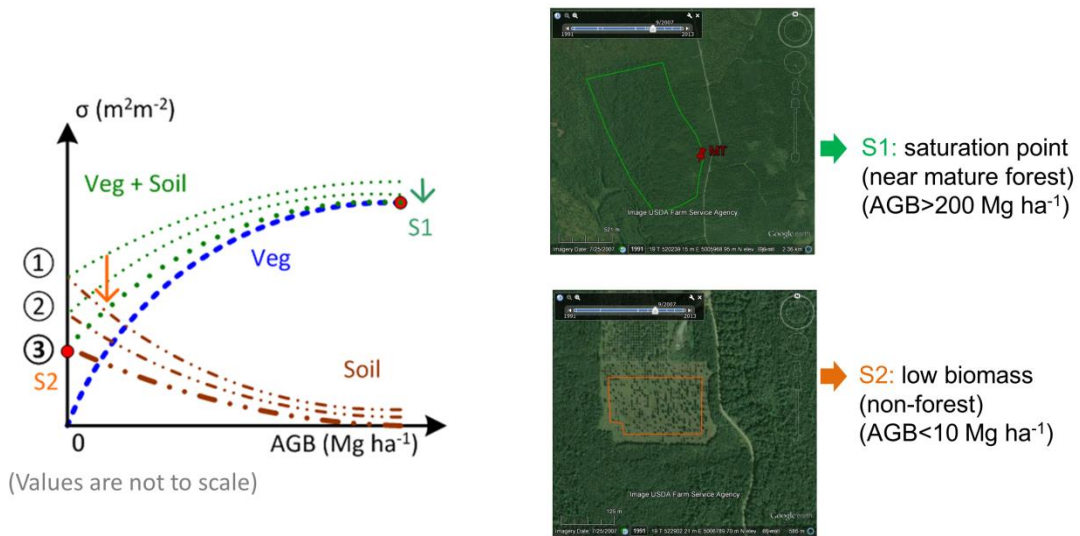
Figure 3-6. Conceptual diagram of the cross-image normalization. Figure units are in power domain ($m^2\ m^{-2}$) for backscatter (σ), and density per hectare ($Mg \cdot ha^{-1}$) for AGB. S1 is the saturation point in a near-mature forest; S2 is the maximum soil effect point in a non-forested area. Dashed blue line (Veg) is the fitted backscatter versus AGB received from vegetation canopy without soil influences in theory. Brown dashed and dotted lines are backscatter from soil surfaces. Green dotted lines are backscatter from vegetation canopy plus soil. ①②③ denotes backscatter from data with different surface and soil moisture conditions.

The following two-step normalization was developed for both airborne and spaceborne SAR data. First, the one-point normalization makes use the saturation point at higher levels of biomass (*i.e.*, near-mature forest). The first-step of the normalization can be expressed as:

$$\sigma_o'^o = (\sigma_{S1t}^o / \sigma_{S1o}^o) \cdot \sigma_o^o$$

Equation 3-3

where σ_o^o (sigma naught) is the original SAR backscatter before normalization. Both σ_{S1t}^o and σ_{S1o}^o are the SAR backscatter of a near-mature forest (S1) from the target (S1t) or reference image and the original image (S1o) that need to be normalized. The variables σ_{S2t}^o and σ_{S2o}^o are the SAR backscatter of the non-forested area (S2) from the target (S2t) or reference image and the image (S2o) that need to be normalized.

Then, the two-point normalization is applied to reduce the environmental effect of the soil component by subtracting it from the total signature. Normalized SAR backscatter after the second-step normalization can be expressed as:

$$\sigma_o''^o = \sigma_o'^o + \Delta\sigma^o$$
$$\Delta\sigma^o = a \cdot \sigma_o'^o + b$$

Equation 3-4

where $\Delta\sigma^o$ is the difference between SAR backscatter at two different soil moisture conditions, and the coefficients a and b are derived from linear fitting of the data:

$$a = (\Delta\sigma_{S1} - \Delta\sigma_{S2})/(\sigma'_{S1o} - \sigma'_{S2o})$$
$$b = \Delta\sigma_{S1} - (\Delta\sigma_{S1} - \Delta\sigma_{S2})/(\sigma'_{S1o} - \sigma'_{S2o}) \cdot \sigma'_{S1o}$$
$$\Delta\sigma_{S1} = \sigma'_{S1t} - \sigma'_{S1o}, \Delta\sigma_{S2} = \sigma'_{S2t} - \sigma'_{S2o}$$

Equation 3-5

where σ'_{S1t} and σ'_{S1o} are the target and the original SAR backscatter, respectively, of mature forest (S1) from Equation 3-3. The variables σ'_{S2t} and σ'_{S2o} are the target and the original SAR backscatter of the non-forested area (S2) from Equation 3-3. Finally, $\Delta\sigma_{S1}$ and $\Delta\sigma_{S2}$ are the differences between SAR backscatter of near-mature forest and non-forested area at two different soil moisture conditions.

Stands with select-cut and clear-cut trees were selected with assistance from forest management map (Figure 3-7a), to test the proposed normalization algorithm, and to analyze the sensitivity of normalized changes in backscatter to forest biomass over time. Figure 3-7a shows representative plots on the AIRSAR image (October 7,1994, R: HH, G: HV, B: VV). Figure 3-7b shows forest management map of logging activities from 1984 to 2011, where patches with different color denote types and years of disturbance. To make the management map comparable to the SAR images, the disturbances were reclassified into plantation before 1994 (1984–1993),

plantation after 1994 (1994–1995), natural regrowth after prior clear-cut, select-cut
and strip-cut events (1984–1993), and recent select-cut (1994–2008).
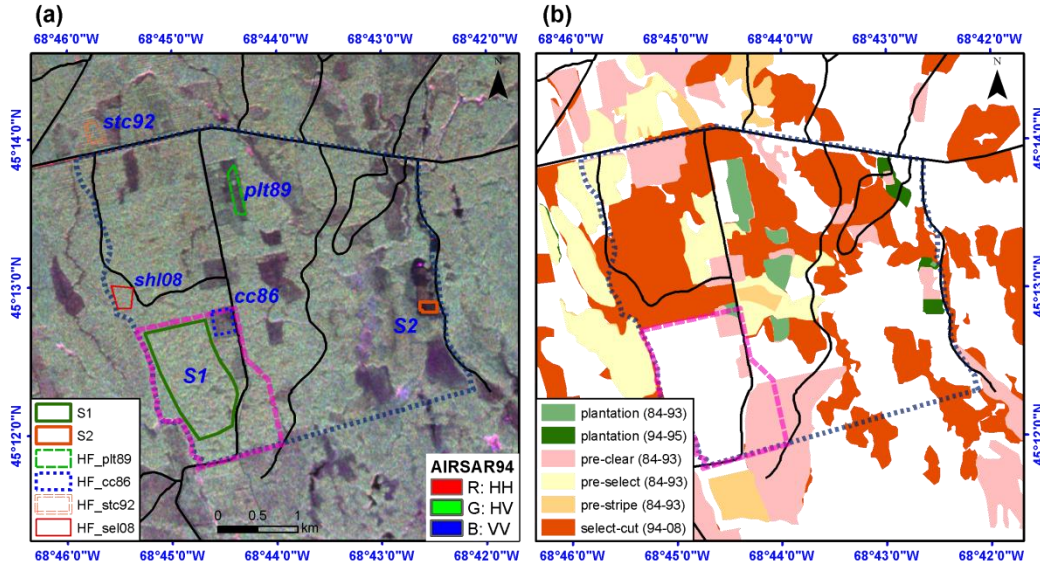
Figure 3-7. (a) Selected plots on AIRSAR image (10/07/1994, R: HH, G: HV, B: VV), and (b)
Forest management map at study site. Pink polygon is the near-mature forest; and dark blue
polygon is the outline of the reserved area. Solid line polygons with labels (*i.e.*, PLT89 =
plantation in 1989; CC86 = clear-cut in 1986; STC92 = strip-cut in 1992; SHL08 =
shelterwood-harvest in 2008) are the plots selected for sensitivity analysis. S1 is the
saturation point in a near-mature forest (biomass >200 Mg ha^{-1}), S2 is the maximum soil
effect point in a non-forested area (biomass <10 Mg ha^{-1}).

3.4   Result

3.4.1   Sensitivity of SAR backscatter to incidence angle

Table 3-3. Correction model parameters and coefficients of determinant for three
polarizations

Polarization	Correction Model	n	R^2
HH		1.5940	0.9733
HV	$\sigma^o_{corr} = \sigma^o_{raw} \cdot (\cos\theta_c / \cos\theta_{raw})^n$	1.5250	0.9665
VV	$\sigma^o_{corr} = \sigma^o_{raw} \cdot (\theta_c / \theta_{raw})^n$	-1.3293	0.9777

The correction models and coefficients of determination derived from

UAVSAR data for three polarizations are given in Table 3-3. Cosine models were

applied to normalize backscatter at HH and HV polarizations, and linear model is

selected for VV polarization.
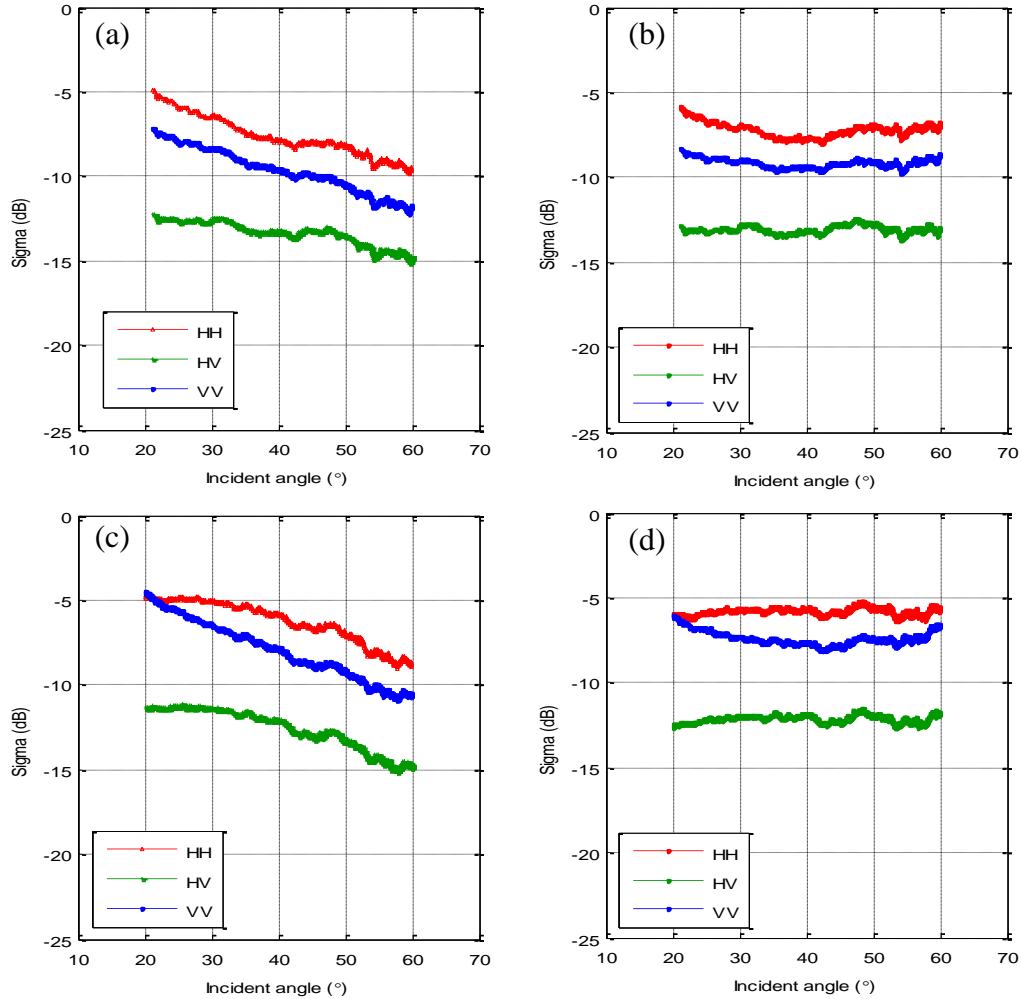
Figure 3-8. Mean backscatter in three polarizations (R:HH, G:HV, B: VV) as a function of incidence angle. AISSAR data acquired on 10/07/1994before (a) and after incidence angle normalization (b), UAVSAR data acquired on 08/05/2009 before (c) and after incidence angle normalization (d).

A plot of SAR backscatter data as a function of incidence angle (Figure 3-8)

illustrates the trend of SAR backscatter before and after the incidence angle based

radiometric correction. Before correction, there are significant decreasing trends

along the incidence angle for both AIRSAR (Figure 3-8a) and UAVSAR data (Figure

3-8c). After incidence angle correction, the overall trends of backscatter along the

incidence angle were mostly removed (Figure 3-8b and Figure 3-8d). Although there

is slightly decreasing trend from 20° to 30°, the corrected values keep relatively

stable (less than 1 dB variation) from 30° to 60° in all three polarizations (*i.e.*, R: HH,

G: HV, B: VV).

The incidence angle contamination from both AIRSAR (Figure 3-10) and

UAVSAR (Figure 3-9) can be seen clearly in the near range (*i.e.*, left edge of images

in the upper row), and there is a systematic decreasing from near range to far range.

The effect of correction on AIRSAR image is very similar to that of UAVSAR

(Figure 3-10 and Figure 3-9).
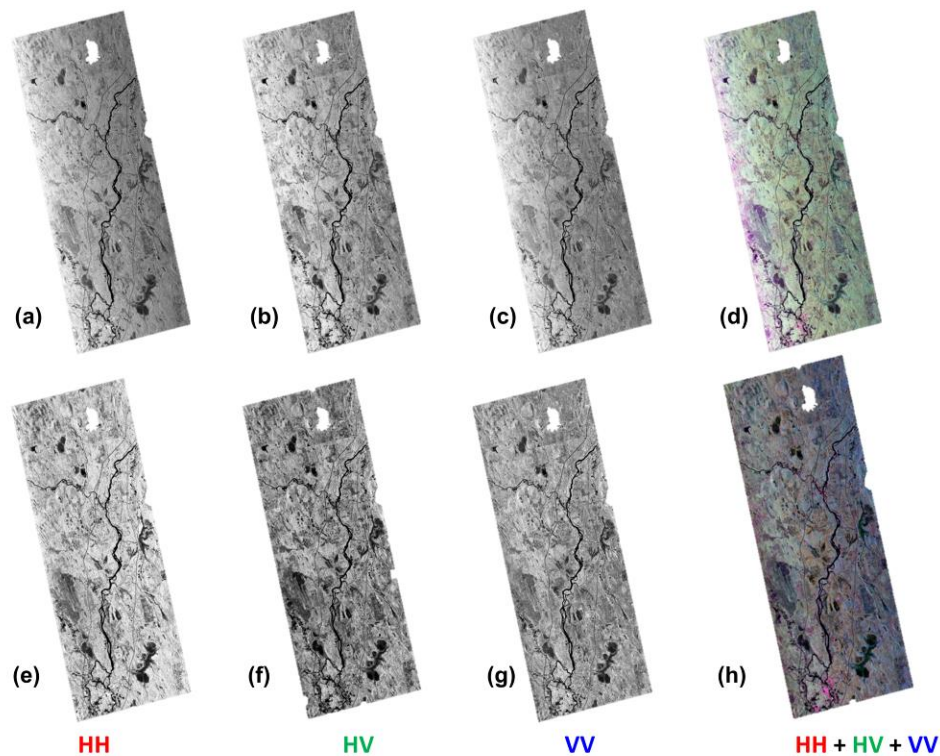
Figure 3-9. Polarized AIRSAR image acquired on 1994/10/07 in three polarizations and composite (R: HH, G: HV, B: VV). The above images (a)-(d) show the image requested from JPL archive, and the below images (e)-(h) are after correction for incident angle.
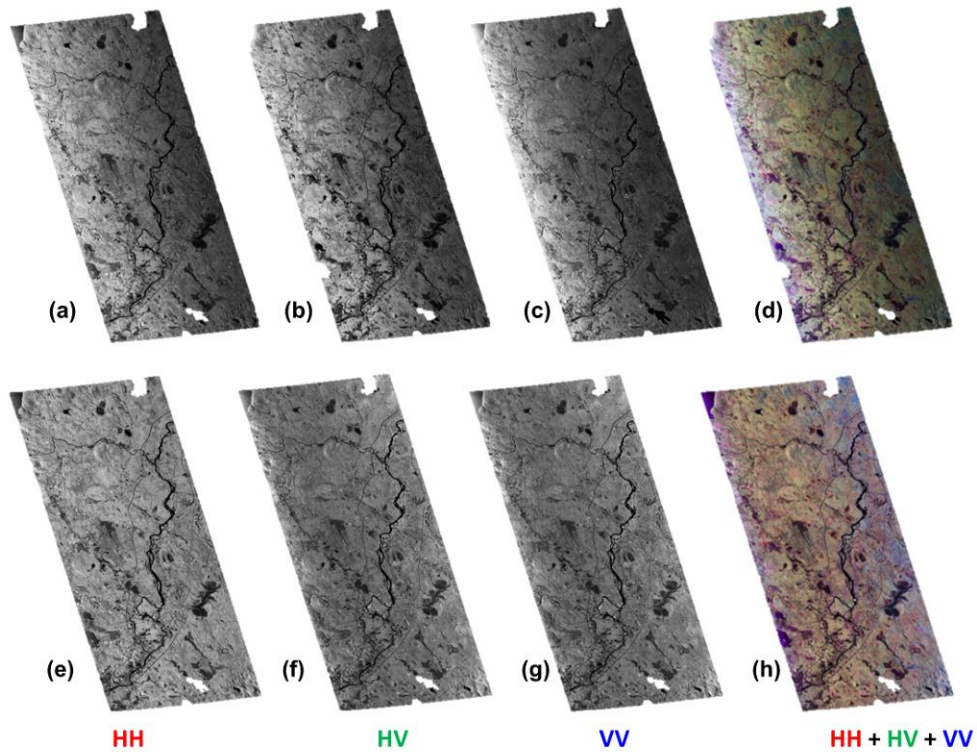
Figure 3-10. Polarized UAVSAR image acquired on 2009/08/05 in three polarizations and composite (R: HH, G: HV, B: VV). The above images (a)-(d) show the calibrated image distributed by JPL, and the below images (e)-(h) are after correction for incident angle.

3.4.2 Sensitivity of SAR backscatter to soil moisture

Two plots with field measurements taken in 2009 were selected to show the sensitivity of backscatter to soil moisture (Figure 3-11). Soil water fraction by volume (WFV) data was collected at 5 cm (2 inches) depth from the Main Tower, Howland. The SAR backscatter (sigma) was extracted from PALSAR data collected during the 2007 to 2010 grown seasons with incidence angle ranging from 37 ° to 40 °. Scatter plots show an increase in backscatter with increasing soil moisture at HH polarization for the low biomass plot (Figure 3-11b). A correction of radiometric distortion due to different soil moisture conditions is possible.

73
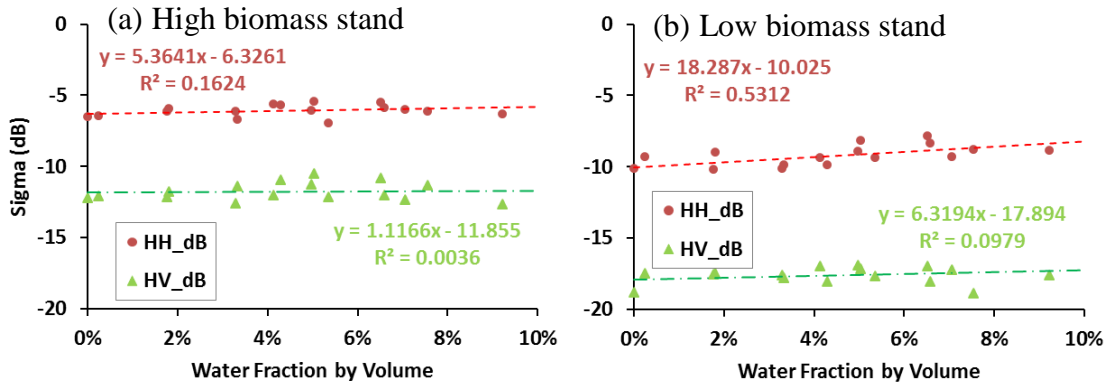
Figure 3-11. Mean backscatter (Sigma) plotted as a function of water fraction by volume (WFV, %): (a) High biomass stand, (b) Low biomass stand.

3.4.3   Sensitivity of normalized SAR backscatter to forest biomass

A two-step normalization was conducted to both airborne and spaceborne SAR data. First, spaceborne SIR-C/XSAR data obtained on April 13 (PR12331) and October 4 (PR47494), 1994 were chosen to test the effectiveness of the proposed algorithm. Specifically, the SIR-C/XSAR data acquired on April was normalized to the data acquired in October. Changes in backscatter from the two SIR-C/XSAR scenes were illustrated for the selected plots (Figure 3-12). The patch of forest near the flux tower was selected as the saturation point (S1), and the clear-cut (CC86) with no canopy in 1994 was selected as the low biomass point (S2). The two selected scenes had similar sensor conditions (*i.e.*, same looking direction and incidence angle). However, environmental conditions changed from April to October, including temperature increased from 5.5 ℃ to 21.6 ℃, and an increase in surface soil moisture. The soil surface was very wet in April not only due to cumulative rainfall that fell three to seven days prior to the SAR acquisition, but also due to the presence of snow. While rainfall totals were higher in October two weeks prior to the SAR acquisitions (76 mm vs. 50.9 mm, Table 3-2), melting snow and lower air temperature in April

74

would have resulted in higher surface moisture.   In fact, field crews in 1994 reported running water (small streams and ponds) at numerous locations in the forest. Finally, deciduous trees had not yet leafed out in April, while deciduous trees had retained their leaves in October, suggesting that sap flow (and thus stem dielectric properties) would have been lower in April than in October.

Before the normalization, we saw an increasing trend of backscatter (~2 dB) for all plots from April to October due to the changes in environmental conditions (Figure 3-12a). After normalization, the trend was removed for most plots (*i.e.*, S1, S2, and PLT89), and reduced for the select-cut plots (*i.e.*, SHL08 and STC89) with subtle changes (<1dB). The proposed two-step normalization algorithm successfully removed 50% to 100% of the effects of environmental conditions on SAR backscatter (Figure 3-13b). Therefore, the following section analyzes the sensitivity of normalized changes in backscatter to forest biomass over time using multi-sources SAR data.

Changes in multi-sensor SAR backscatter over time were analyzed for selected plots (Figure 3-13). Airborne AIRSAR data from 1989 and 1994 were normalized to UAVSAR data in 2009 (Figure 3-13a). Spaceborne SIR-C/XSAR data in Oct 1994 were normalized to PALSAR data in 2009 (Figure 3-13b). As expected, the change in biomass with time varies for different types of forest disturbance. Whole-stand disturbance (plantation after clear-cut) before the 1990s could be effectively detected its backscatter signature. Plantation (PLT89) and natural recovery (CC86) are good examples to show post-disturbance recovery from clear-cut events before the 1990s.

On the other hand, changes after partial-stand disturbance (*i.e.*, shelterwood-harvest and strip-cut) could be detected by SAR signatures only under certain conditions. The strip-cut stand, occurred in 1990s (STC92), shows a relatively slow recovery rate, which is not sensitive to SAR signatures. However, the decrease of biomass from shelterwood-cut between 1994 and 2009 (SHL08) is detectable. For example, SHL08 means the 1st entry was in 1998 and the 2nd entry was in 2008, when each time ~1/3 of the total biomass was removed. Previous model simulation *(Sun and Ranson, 1998)* showed that when radar looks perpendicular to the strip-cut direction, the radar signature doesn't change significantly. Meanwhile, the reason for radar not being able to detect the regrowth may be that radar signal after the strip-cut was still strong.
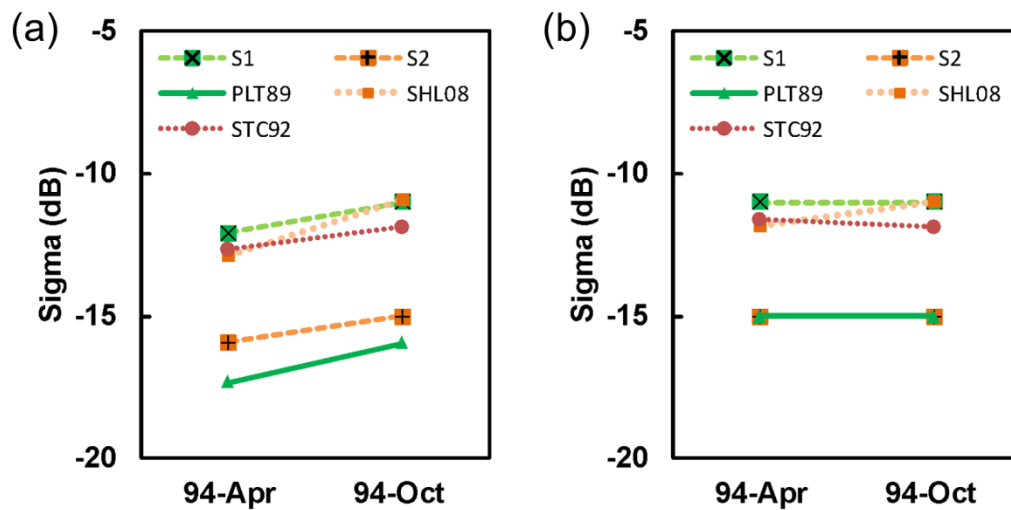
Figure 3-12. Changes in SAR backscatter (HV) from SIR-C/XSAR 1994 at represented plots: (a) before normalization, (b) after normalization.
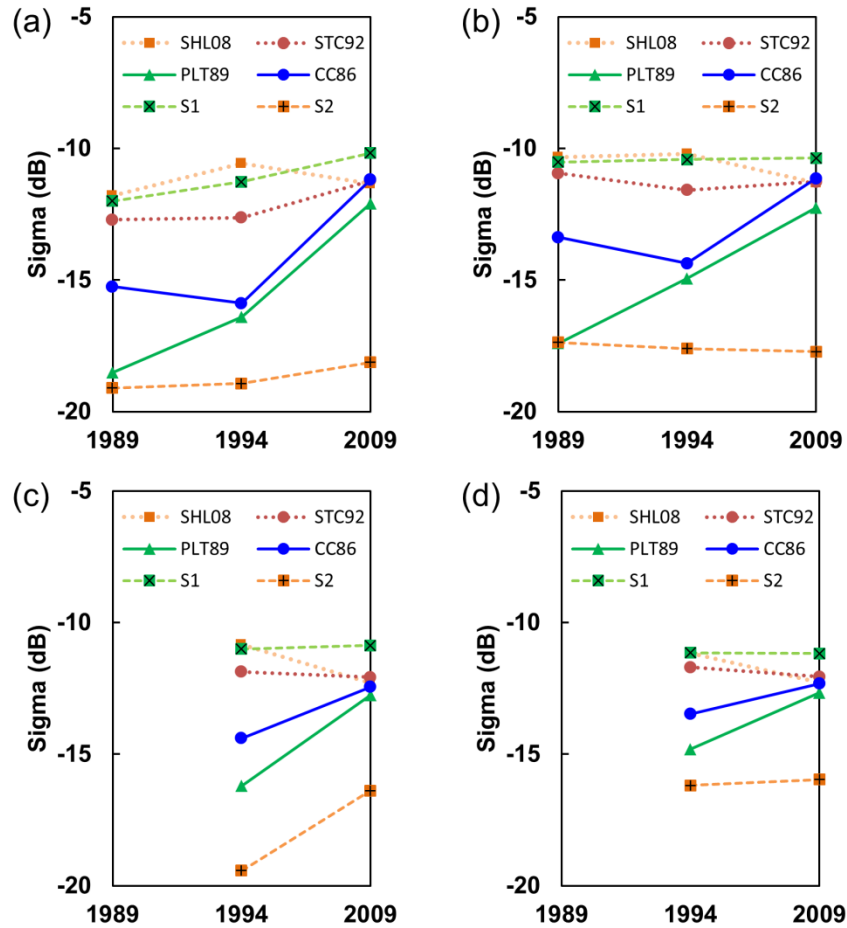
Figure 3-13. Original and normalized multi-sources backscatter (1989–2009) from airborne- and spaceborne- SAR systems at represented stands: (a) and (c) are from original data, and (c) and (d) are from normalized data. Airborne data include AIRSAR 89/09/02, 94/10/07, and UAVSAR 09/08/05. Spaceborne data include SIR-C/XSAR 94/10/07 and PALSAR 09/08/30.

3.5   *Discussion*

Our objectives were to investigate the influence of incidence angle (IA), soil moisture (SM), and changes in forest biomass on SAR backscatter. Knowledge from these analyzes forms the base for the cross-image normalization. Results from both spaceborne- and airborne- systems demonstrated that normalization ensured the derived biomass of regrowth forests was cross-calibrated, making the detection of

77

biomass changes from multi-source SAR data possible. Several main factors lead to this conclusion.

Results from airborne systems indicated that the influence of IA on SAR backscatter could be reduced to less than 1 dB using an empirical model (Figure 3-8). We chose an empirical method for incidence angle correction because it is efficient and only needs basic sensor parameters (*i.e.*, near range distance, instrument height, incident angle at near range and slant range resolution). Thus, this procedure was suitable for this study area, which has with a relatively flat topography and limited information in terms of sensor parameters in the archived data (AIRSAR). However, a more advanced radiometric correction that integrated terrain variations *(Small, 2011)* should be applied in regions with large terrain variation to improve the precision of the correction.

Second, the sensitivity of SAR backscatter to soil moisture was analyzed via spaceborne PALSAR data and *in situ* measurements from April 2007 to October in 2010. A cross-image normalization procedure was used to reduce the influence of environmental and acquisition conditions among multi-source SAR data. This procedure successfully reduced the temporal changes in backscatter for SIR-C/XSAR data collected between April and October 1994 by 50% to 100% (Figure 3-12). Assuming that surface roughness was the same in April and October, increased surface wetness would have increased direct backscattering from soil and double-bounce backscattering. More sap flow and higher temperatures in October increased the dielectric constant of the tree trunks, increasing direct backscatter from the trunk and the trunk-ground double bounce. A further application to multi-sensor SAR data

indicated that the proposed procedure successfully reduced radiometric distortions due to different acquisition conditions (Figure 3-13). We chose near-mature forest stands and non-forested area because they met the requirements for high and low biomass in the conceptual diagram (Figure 3-6Figure 3-6). Future work needs to incorporate physical-based models and develop according normalization algorithms.

In addition, the influence of incidence angle and soil moisture depends on the area and location of study area. For instance, previous studies suggests that correction of incidence angle effect is essential for study area with a range of incidence angle greater than 10 ° across the landscape *(Menges et al., 2001)*. While the effects of soil moisture will become more important as a study area approaching national to continental scale, because of the increasing spatial variation in soil moisture. However, current soil moisture products derived from interpolation of meteorological station data or available satellite observation have limited spatial and temporal resolution. For example, the Aqua Advanced Microwave Scanning Radiometer-EOS (AMSE-E) is with a nominal spatial resolution of 25 km *(Lucas et al., 2010),* which is beyond the scale of our study site. The relationship between SAR backscatter and soil moisture for the forested and non-forested areas is still under exploration because of limited observational as well as high-temporal SAR data.

Thirdly, the ability to detect forest biomass reduction and regrowth using SAR backscatter also depends on numerous factors such as the level of disturbance, model uncertainties, radar looking directions, forest structures, trunk dielectric properties, and tree species. Forest recovery from whole-stand disturbance (>50% removal), such as natural regrowth and plantation after clear-cut events, could effectively be detected

by backscatter signatures. Depending on the magnitude of change and radar looking direction, the recovery from partial-stand disturbance (shelterwood harvest and strip-cut with <50% removal) was not always captured by SAR signatures. Uncertainty in biomass estimation from single-date models will affect this ability. We were able to detect changes for pixels with changes greater than 100 Mg ha^{-1} or above 50% of 150 Mg ha^{-1}, although with a ~50 Mg ha^{-1} prediction error from the model. This is consistent with our analysis of selected plots (Figure 3-13), indicating that the level of disturbance has an influence on SAR detection ability. A previous study *(Robinson et al., 2013)* had mentioned the effect of forest structure and tree species composition on the biomass estimation. The model developed for biomass mapping in this study did not take these effects into account because of a relatively simple species composition in the study area. However, we still recommend considering structure and species effects in areas with more complicated composition.

Lastly, previous studies have indicated that a combination of multiple observations could improve the accuracy of biomass estimation from SAR data because multiple images provide more samples and using them together could reduce the radar speckle noise *(Englhart et al., 2011; Zhang, 2011)*. For example, *Zhang (2011)* indicated that models developed using multi-direction SAR backscatter (*i.e.*, left and right look) achieved the best performance in estimation of forest biomass. Moreover, *Englhart et al. (2011)* demonstrated that regression models developed from multiple observations with multiple frequencies such as SAR data from PALSAR (L-band) and TerraSAR-X (X-band) are more accurate than regression models developed from single observation. There is a trade-off between pixel size

80

and the ability to detect disturbance. Therefore for biomass estimation, the data were resampled to a 100 m resolution, and a mean value was calculated for each cell so that it was large enough to reduce the speckle noise in the SAR data used in this study. Airborne SAR data (*i.e.*, UAVSAR and AIRSAR) with higher spatial resolution revealed more detail than spaceborne data (*i.e.*, PALASAR and SIR-C/XSAR) in terms of changes in forest biomass.

3.6   *Conclusion*

This chapter analyzed the sensitivities of multi-sensor and multi-temporal SAR signatures to changes in forest biomass. Knowledge from these sensitivity analyses and corresponding correction is the base to the cross-image radiometric normalization. Results from both spaceborne- and airborne- systems demonstrated the normalization ensured the derived biomass of regrowth forests were cross-calibrated, and thus make the detection of biomass changes possible.

Findings from this study indicate that the use of a correction model can reduce incidence angle effects on SAR backscatter to less than 1 dB, and that cross-image normalization can reduce the effect of soil moisture on changes in backscatter to less than 50%. Thus, the changes in forest biomass greater than 100 Mg ha^{-1} or above 50% of 150 Mg ha^{-1} are detectable using cross-normalized SAR data.

Chapter 4   Mapping Biomass Change after Forest Disturbance from Multi-source SAR[3]

4.1   *Introduction*

A series of studies have utilized airborne instruments such as AIRSAR *(Ranson and Sun, 1997; Saatchi et al., 2011a)* and UAVSAR *(Robinson et al., 2013)* to estimate forest biomass; and spaceborne instruments such as PALSAR *(Mitchard et al., 2009a; Santoro et al., 2010)*, to detect clear-cut areas, evaluate forest biomass *(Lucas et al., 2010)*, and retrieve soil moisture for bare land *(Guo et al., 2013)* and post-burned forest *(Bourgeau-Chavez et al., 2013)*. Specifically, L-band SAR imagery can be used to monitor the changes in biomass and carbon stocks for early stages of secondary succession *(Ustin et al., 1991)* and post-disturbance recovery *(Hall et al., 2011). Ustin et al. (1991)* indicated that changes in biomass during the early stages of secondary succession could be monitored by L-band airborne SAR data for two datasets with an interval of five years. Their study also demonstrated that cross-image normalization is feasible for radar data obtained through stable systems under similar conditions. *Ranson and Sun (1997c)* developed a cube root regression model to estimate biomass density for a temperate forest using SIR-C/XSAR and AIRSAR data. *Salas et al. (2002)* evaluated the spatial and temporal variability in JERS-1 data and characterized the overall structure of clearings and secondary vegetation with age information derived from Landsat. *Baltzer et al. (2003)* utilized multi-sensor L-band SAR data (i.e., spaceborne SEASAT and JERS-1) to map regrowth of a conifer plantation in the Thetford Forest, UK. *Luckman et al. (1997)* compared biomass estimated from spaceborne SAR instruments

---

[3] The presented material is under preparation for publication: Huang, W., Sun, G., Ni, W., Zhang, Z., Dubayah, R. Mapping Biomass Change after Forest Disturbance using Multi-source SAR data.

(SIR-C/XSAR and JERS-1) and concluded that L-band SAR data were suitable for detecting regeneration in tropical regions. *Santoro et al. (2010)* utilized airborne and spaceborne data such as PALSAR to detect clearcutting of a boreal forest from July 2007 to October 2008 and found a temporal consistency in the time series of L-HV backscatter measurements and developed a detection algorithm for clear-cut areas.

However, few studies quantify the changes in forest biomass using multi-source L-band SAR data, because of issues such as limited SAR data acquisition over time, changes in forest structure *(Dobson et al., 1995)*, radar incidence angle *(Sun et al., 1991; Wang et al., 1993)* and look direction *(Sun and Ranson, 1998)*, variations in surface conditions *(Harrell et al., 1997; Kasischke et al., 2011; Lucas et al., 2010)* and trunk dielectric properties *(Way et al., 1991)*, and saturation *(Dobson et al., 1992; Kasischke et al., 1997; Ranson and Sun, 1997)*. These issues have been discussed in the last chapter. *Sandberg et al. (2014)* estimated biomass change in a hemi-boreal forest from 2007 to 2010 using airborne P-band SAR data, and concluded that growth and thinning in a forest can be measured with 64 equivalent number of look (ENL) in SAR imagery and a 50% change in biomass. Ahmed et al. *(Ahmed et al., 2014)* indicated that the combined error from field measurements and remote sensing could be as much as 100% at sub-plot level (0.25 ha) for Howland and Harvard Forest sites, and recommended at least a 1 ha (100 m) spatial resolution for mapping of forest biomass.

In this chapter we will investigate: 1) what will be the proper scale for mapping biomass from SAR data, 2) what are the uncertainties in the mapping of forest biomass using data from spaceborne and airborne systems, and 3) at which level predictions are reliable in terms of the changes in biomass. The changes in forest biomass for the study

sites were analyzed using SAR data from spaceborne (1994–2009) and airborne (1989–1994–2009) SAR systems.

4.2   *Data*

Spaceborne and airborne SAR data (Figure 4-1) are employed to map the change in biomass over a 15-year period (1994–2009) and a 20-year period (1989–2009). Details about the study site, SAR data, and auxiliary data have been introduced in the last two chapters, and are not described herein. The field data used for training and validation are summarized in Table 4-1.
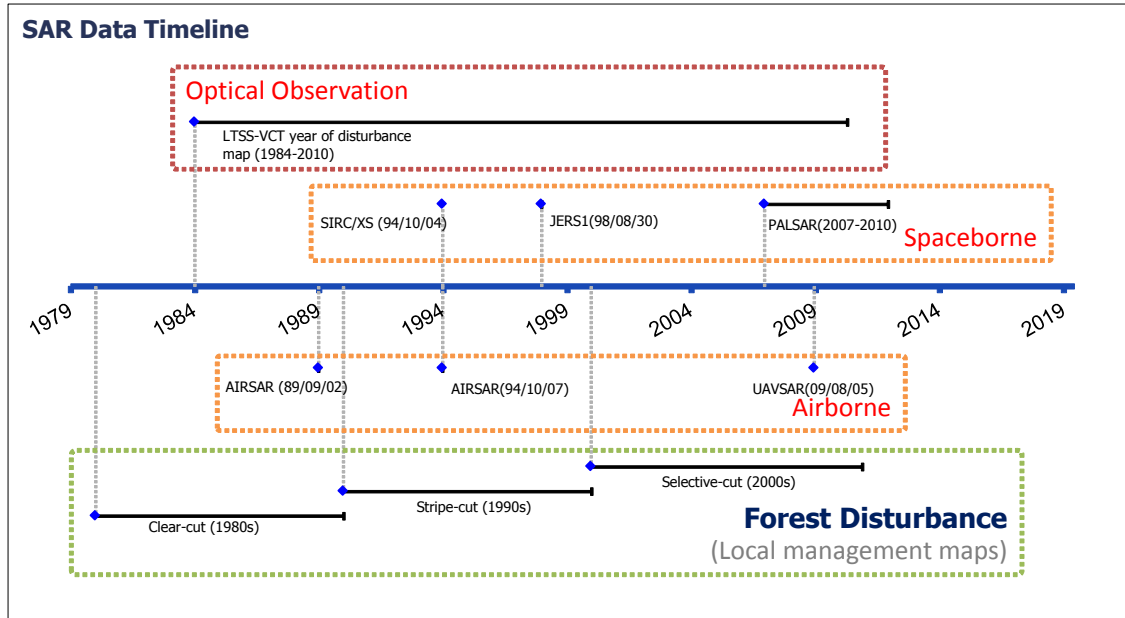
Figure 4-1. Timeline of SAR data at HF site. Optical data are acquired during the leaf-on season, and SAR data are from L-band. Forest management maps are digitized from local management maps.

Table 4-1. Summary of field estimated biomass in 2009 at different plot-level

Plot-size	N	Mean	Min	Max
ha		$Mg \cdot ha^{-1}$	$Mg \cdot ha^{-1}$	$Mg \cdot ha^{-1}$
0.25 ha	115	141.1	0.3	361.4
0.5 ha	57	140.3	0.6	316.0
1.0 ha	24	143.3	1.0	278.9
All	196	141.2	0.3	361.4

4.3   Method

The overall procedure consists of multi-source data processing, radiometric normalization, model development, and biomass mapping (Figure 4-2).
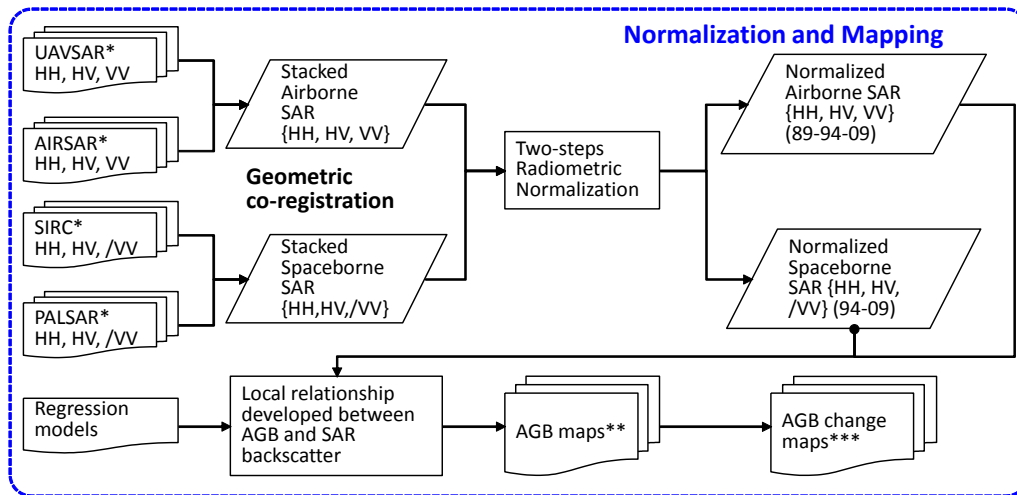
Figure 4-2. Flowchart of SAR data preparation, normalization and mapping.

4.3.1   Multi-source SAR data processing

Current radar derived products for surface conditions such as soil moisture are still under development and are often with large uncertainties in estimates. In order to limit the influence of surface conditions on the retrieval of forest biomass from radar backscatter attributes, SAR images with very low or no precipitation within three days around acquisition date were selected for further analysis.

Archived AIRSAR data in the 1990s were provided by JPL in the compressed strokes matrix (CM) format *(JPL, 2003)*. The 4 x 4 Stokes matrix data was compressed into 10-byte format, to reduce the original 1.92 GB data to 37.5 Mbytes per scene *(Dubois and Norikane, 1987)*. SIR-C/XSAR data in 1994 were provided in the compressed SIR-C format *(JPL, 1994)* with a CEOS header file. For both AIRSAR and

SIR-C/XSAR systems, multi-looked complex (MLC) data were used in this study. The compressed AIRSAR and SIR-C/XSAR data were processed to coherency elements (T3) from quad polarimetric data and to covariance elements (C3) from dual polarimetric data. These datasets were processed using the PolSARPro Polarimetric SAR Data Processing and Educational Tool developed by the European Space Agency (Version 4.2.0) *(Pottier et al., 2009)*.

Slant range AIRSAR layers were converted to ground range images using "Slant Range Correction" function in ENVI 4.8. This step converts the distance from the radar (slant range, Υ_{SR}) to distance along the ground (i.e., ground range, Υ_{GR}) and samples data to a desired output pixel spacing as follows:

$$\gamma_{GR}^{\circ} = \gamma_{SR}^{\circ} / \sin\theta \qquad \text{Equation 4-1}$$

where θ is the incidence angle.

Then, the ground range layers of AIRSAR and SIR-C were manually registered to a Landsat7 ETM+ image (path011/row029) acquired on Sept 9, 2000, using a first-degree polynomial model.

PALSAR operates in several modes, including two fine-beam modes: single polarization (FBS) and dual polarization (FBD); and a full polarization mode (PLR). The FBD mode with HH and HV data at the 34.3 ° incidence angle (image center) were used in this study. PALSAR FBD and PLR data from 2007 to 2009 were acquired at Level 1.1/1.5 and were processed to normalized radar cross section (NRCS). These datasets were processed using the MapReady Remote Sensing Toolkit (Version 3.1.22) *(Gens and Logan, 2003)* supported by Alaska Satellite Facility (ASF) and the terrain information

from National Elevation DEM (NED). NRCS of the polarization component is derived

from following equations with a single calibration factor (CF):

L1.5 product: $NRCS\ (dB) = 10\log_{10}(<DN^2>) + CF$ **Equation 4-2**

L1.1 product: $NRCS\ (dB) = 10\log_{10}(<R^2 + I^2>) + CF - 32.0$ **Equation 4-3**

where DN is the digital number value (amplitude) in the image; R and I are intensity and

phase values; and CF is listed in *Table 4-2* provide by JAXA.

(http://www.eorc.jaxa.jp/en/about/distribution/info/alos/20090109en_3.html).

Table 4-2. The calibration factor (CF) for ALOS/PALSAR data

Processing date	Before Jan. 8, 2009	After Jan. 9, 2009
FBD34.3 HH	-83.2	-83
FBD34.3 HV	-80.2	-83
PLR21.5	-83.4	-83

UAVSAR polarimetric (PolSAR) data in 2009 were acquired from JPL in ground

range grid (GRD) format in geographic coordinate system (WGS 84). These datasets

were then projected into a common frame of reference (UTM 19N WGS 84) used in this

study.

Table 4-3. Co-registration accuracies for the selected SAR data the test sites

Sensor	Scene id	Acquisition date	#Point	RMS		Resolution (m)
				X	Y	
PALSAR/FBD	ALPSRP198390890	10/15/2009	31	0.4510	0.4045	12.5
PALSAR/FBD	ALPSRP191680890	8/30/2009	29	0.4005	0.3541	12.5
PALSAR/PLR	ALPSRP179280900	6/6/2009	57	0.4575	0.3957	12.5
PALSAR/PLR	ALPSRP172570900	4/21/2009	76	0.4240	0.4826	12.5
PALSAR/FBD	ALPSRP131290890	7/12/2008	31	0.4985	0.4066	12.5
PALSAR/FBD	ALPSRP124580890	5/27/2008	46	0.4179	0.3250	12.5
PALSAR/FBD	ALPSRP120350890	4/28/2008	38	0.3237	0.3979	12.5
PALSAR/FBD	ALPSRP091030890	10/10/2007	30	0.3866	0.3505	12.5
PALSAR/FBD	ALPSRP086800890	9/11/2007	41	0.4251	0.4156	12.5
PALSAR/FBD	ALPSRP084320890	8/25/2007	41	0.4193	0.4483	12.5
PALSAR/FBD	ALPSRP080090890	7/27/2007	30	0.4840	0.4593	12.5
PALSAR/FBD	ALPSRP077610890	7/10/2007	39	0.4495	0.4778	12.5
PALSAR/FBD	ALPSRP073380890	6/11/2007	37	0.4806	0.4431	12.5
PALSAR/PLR	ALPSRP071920900	6/1/2007	47	0.4185	0.4019	12.5
PALSAR/FBD	ALPSRP068932710	5/11/2007	65	0.4345	0.4079	12.5
PALSAR/FBD	ALPSRP065210900	4/16/2007	71	0.4477	0.4872	12.5
SIR-C/XSAR	PR12331	4/13/1994	32	0.2816	0.4851	30
SIR-C/XSAR	PR47494	10/4/1994	22	0.3878	0.4410	30
AIRSAR	CM6220	10/7/1997	31	0.3549	0.3759	10

*PALSAR data used in this study involved two modes: FBD= Fine beam dual mode, and PLR=Polarimetric mode.

Finally, all SAR data including AIRSAR, SIR-C/XSAR, PALSAR were co-registered to the same Landsat image (September 09, 2000, path011/row029,) using a modified ROI_PAC script for precise co-registrations *(Ni et al., 2013b)*. The registration errors (RMS) were minimized (<1 pixel) to reduce the influence of geolocation errors in SAR data (*Table 4-3*). All conversions were processed in power domain ($m^2 m^{-2}$), and the arithmetic mean values were used when aggregating SAR data to different scales. Backscatter coefficients were converted into dB domain for biomass estimation:

$$\sigma°(dB) = 10\log_{10}\sigma°(m^2 m^{-2})$$ **Equation 4-4**

Airborne SAR data (i.e., AIRSAR and UAVSAR) were normalized by the correction models as described in Chapter 3 to reduce the effect of incidence angle.

4.3.2 Modeling approaches for biomass estimation

SAR backscatter coefficients, band ratios, and relevant indices are found to be sensitive to canopy structural variables and biomass *(Gon çalves et al., 2011; Henderson and Lewis, 1998; Pope et al., 1994; Saatchi et al., 2010)*. Specifically, Table 4-4 summarizes the indices used in this study as predictors in biomass modeling. We utilized indices including single polarization backscattering coefficients (*i.e.*, HH, HV, and VV), cross-polarized indices, and full-polarized indices. The single-polarized indices are applicable for all SAR data in this study, while the full-polarized indices are not available for either PALSAR FBS or PALSAR FBD due to the lack of full-polarization (absent HV and/or VV). All statistical calculations were performed using R with packages 'caTools', 'forecast' and 'caret' *(Liaw and Wiener, 2002)*.

Table 4-4. SAR backscatter coefficient, cross- and full- polarized indices

Attributes	Equation	Function and reference
σ_k^o	$10^{\frac{\sigma_k^o[dB]}{10}}$ $\sigma_k^o[dB] = 20\log 10\left(\lvert S_k \rvert F_j\right)$	Backscattering coefficient* *Henderson and Lewis (1998)*
R_{cross}	$\dfrac{\sigma^0{}_{HV}}{\sigma^0{}_{HH}}$	Cross-polarized ratio *Henderson and Lewis (1998)*
RFDI	$\dfrac{\sigma^0{}_{HH} - \sigma^0{}_{HV}}{\sigma^0{}_{HH} + \sigma^0{}_{HV}}$	Radar forest degradation index *Saatchi et al. (2010)*
BMI	$\dfrac{\sigma^0{}_{HH} + \sigma^0{}_{VV}}{2}$	Biomass index *Pope et al. (1994)*
VSI	$\dfrac{\sigma_{HV}^o}{\sigma_{HV}^o + BMI}$	Volume scattering index *Pope et al. (1994)*

Expressed in the intensity format. |Sk| is the amplitude response (k = HH, VV, or HV) and Fj is a calibration factor for column j, determined from data collected over the trihedral corner reflectors (Gonçalves et al., 2011).

Forest biomass values are related to SAR backscatter (σ_p^o) as:

$$AGB = e^{(a+b\sigma_p^o)}$$ **Equation 4-5**

where σ_p^o represents backscatter value (*i.e.*, sigma naught) at different polarizations (*i.e.*,

HH and HV) and *a* and *b* are the exponential coefficients. To improve the fitting process,

we estimated coefficients using linear regression:

$$y = a + b\sigma_p^o$$ **Equation 4-6**

where *y=ln(AGB)* and *a* and *b* are the linear coefficients.

4.3.3 Accuracy assessment of regression models

We assessed the regression models using leave-one-out cross-validation (LOOCV)

performed with R (Version 2.14.2) *(Kuhn, 2008)*. The predicted values were regressed

against the field-measured values to quantify the accuracy of the model using statistical

indicators such as root mean square error from cross-validation (*RMSEcv*), relative error

of *RMSEcv* (*RMSEcv%*), and coefficient of determination (R^2).

The LOOCV is an effective solution to evaluate the regression models when there

are a small number of samples to test the model *(Zhao and Popescu, 2009)*. The general

procedure of LOOCV is described as follows:

1) Select observation *i* from a test set (*i.e.*, *n* independent observations $y_1, ..., y_n$)

and fit the model using the remaining data. Then compute the predicted residual for the

omitted observation:

$$e_i^* = y_i - \widehat{y}_i$$ **Equation 4-7**

2) Repeat step 1 for *i=1, ..., n*.

3) Compute the *RMSE* from $e_1^*, \cdots, e_n^*$, which is called $RMSE_{cv}$.

The ratio of $RMSE_{cv}$ to the mean observed value is also calculated:

$$RMSEcv(\%) = \frac{RMSEcv}{\bar{y}}$$

Equation 4-8

where $\bar{y}$ is the mean biomass.

4.3.4   Mapping forest biomass and changes

The mapping procedure consists of four steps (Figure 4-2): 1) normalize the SAR data; 2) develop the prediction model; 3) evaluate the model performance; and 4) map the biomass and changes.

To normalize the SAR data, a two-step radiometric normalization was conducted to spaceborne and airborne SAR data. Specifically, airborne AIRSAR data in 1989 and 1994 were normalized to UAVSAR data in 2009, and spaceborne SIR-C/XSAR data in 1994 were normalized to PALSAR data in 2009. Then, the developed biomass-backscatter regression models were applied to multi-year SAR data to generate biomass maps for spaceborne and airborne data from 1989, 1994 and 2009 for the study area. Finally, maps of the changes in biomass were created for 15- and 20-year periods from airborne SAR data, and for a 15-year period from spaceborne SAR data.

4.4   Result

4.4.1   SAR backscatter sensitivity to biomass

The backscatter-biomass regression models show strong correlation across different spatial scales (Table 4-5). The SAR backscatter values at all polarizations (HH, HV, and VV) were regressed to field-measured biomass at three scales (0.25 ha, 0.5 ha,

92

and 1.0 ha). At all polarizations, the R^2 of this relationship increased as the plot size increased, where the least variability was observed at 1.0 ha plot-scale. This biomass-HV relationship had the highest coefficient of determinations (R^2) at all spatial scales for UAVSAR (0.47, 0.48, and 0.60) and PALSAR (0.50, 0.57, and 0.68) as plot size increased. The biomass-backscatter relationship derived from airborne UAVSAR data is stronger than that from spaceborne PALSAR data. This is not unexpected, given the finer spatial resolution and the higher signal to noise ratio in airborne data. Since more equivalent 'looks' average values over field plots, there was a better agreement at 1.0 ha plot-scale despite the variability at 0.25 ha plot-scale.

4.4.2 Evaluation of prediction models

The predictions models from PALSAR 2009 data were evaluated across three plot-levels (Table 4-5, Table 4-6, and Table 4-7). The best model at all three plot-levels is the HV model, and overall model accuracy improved with larger plot size. The best single-term model is the HV model at 1.0 ha plot-level with the highest explanation of total variance (68%) and the lowest $RMSE_{CV}$ of 45.5 Mg·ha^{-1} (31.7%).

The predictions models from UAVSAR data in 2009 were evaluated across three plot-levels: 1) 0.25 ha, 2) 0.5 ha, and 3) 1.0 ha, respectively (Figure 4-3, Figure 4-4, Figure 4-5, and Figure 4-6). This is similar to the trends observed from the PALSAR data. As expected, the best model at all three plot-levels is the HV model with higher explanation of total variance (R^2), and lower $RMSE_{CV}$. The overall model performance improved as the plot-size increased. The HV model at 1.0 ha (equivalent to 100 m pixel size) explained 60% of the total variance and had a $RMSE_{CV}$ of 49.0 Mg·ha^{-1} (34.2%).

Moreover, the best multi-variable model is the HH+HV+VV model at 1.0 ha plot-level with the highest explanation of total variance (72%) and the lowest $RMSE_{CV}$ of 40.9 $Mg \cdot ha^{-1}$ (28.5%).

Therefore, the multi-variable models (Table 4-7) derived from PALSAR data (HH and HV) and UAVSAR data (HH, HV, and VV) at 1.0 ha plot-level were selected to predict biomass. The selected models were applied to all SAR data (*i.e.*, UAVSAR, AIRSAR, PALSAR, and SIR-C/XSAR) and the biomass maps were generated at 100 m spatial resolution.

Table 4-5. Summary of single term regression models at different plot-level

Instrument /Year	Variable	Plot-size (ha)	a	b	R^2	RMSEcv ($Mg \cdot ha^{-1}$)	RMSEcv (%)
PALSAR 2009	HH	0.25	8.37±0.88	0.56±0.13	0.24	75.9	53.8%
		0.50	8.65±1.25	0.60±0.18	0.26	72.0	51.3%
		1.0	9.26±2.06	0.69±0.31	0.34	65.6	45.8%
	HV	0.25	11.64±0.83	0.57±0.07	0.50	63.0	44.6%
		0.50	11.79±1.10	0.59±0.09	0.57	53.8	38.4%
		1.0	12.37±1.54	0.64±0.13	0.68	45.5	31.7%
UAVSAR 2009	HH	0.25	8.11±0.48	0.63±0.08	0.20	91.2	64.6%
		0.50	8.24±0.66	0.66±0.12	0.19	84.4	60.2%
		1.0	8.63±0.95	0.72±0.17	0.27	78.1	54.5%
	HV	0.25	11.16±0.50	0.57±0.04	0.47	59.5	42.2%
		0.50	11.27±0.62	0.57±0.05	0.48	55.8	39.7%
		1.0	11.42±0.82	0.59±0.07	0.60	49.0	34.2%
	VV	0.25	10.26±0.58	0.75±0.08	0.44	67.2	47.6%
		0.50	10.44±0.75	0.78±0.10	0.45	62.0	44.2%
		1.0	10.87±1.03	0.83±0.14	0.64	46.9	32.7%

* bolded is the best models; equations in form of AGB=exp(a+bx);

Table 4-6. Summary of single index regression models at different plot-level

Instrument /Year	Variable	Plot-size (ha)	a	b	R^2	RMSEcv $(Mg·ha^{-1})$	RMSEcv (%)
PALSAR 2009	Rcross	0.25	8.90±0.94	0.78±0.17	0.15	103.6	73.4%
		0.50	9.84±1.33	0.94±0.24	0.27	90.3	64.4%
		1.0	10.81±1.98	1.13±0.36	0.30	93.1	64.9%
	RFDI	0.25	1.98±0.82	-1.03±0.31	0.09	132.7	94.0%
		0.50	1.03±1.24	-1.41±0.47	0.23	107.1	76.3%
		1.0	-0.08±2.03	-1.82±0.77	0.25	119.5	83.4%
UAVSAR 2009	Rcross	0.25	11.32±1.18	1.10±0.19	0.30	92.7	65.6%
		0.50	11.84±1.64	1.19±0.27	0.37	97.9	69.8%
		1.0	13.20±2.42	1.42±0.40	0.41	92.3	64.4%
	RFDI	0.25	0.22±0.95	-1.98±0.42	0.26	116.8	82.7%
		0.50	-0.03±1.33	-2.10±0.59	0.33	121.6	86.7%
		1.0	-1.44±2.13	-2.72±0.94	0.35	126.0	87.9%
	BMI	0.25	9.26±0.51	0.73±0.08	0.28	85.4	60.5%
		0.50	9.43±0.67	0.76±0.10	0.28	77.2	55.0%
		1.0	9.80±0.92	0.81±0.14	0.40	66.4	46.3%
	VSI	0.25	16.02±1.38	1.79±0.22	0.28	74.1	52.5%
		0.50	16.39±1.86	1.85±0.29	0.32	66.2	47.2%
		1.0	17.57±2.41	2.04±0.38	0.42	62.3	43.5%

* bolded is the best models; equations in form of AGB=exp(a+bx);
Rcross=HV/HH, RFDI=(HH+HV)/(HH-HV), BMI=(HH+VV)/2, VSI=HV/(HV+BMI).

Table 4-7. Summary of multi-variable regression models at different plot-level

Instrument /Year	Variable	Plot-size (ha)	a	b	c	d	R^2	RMSEcv (Mg·ha^{-1})	RMSEcv (%)
PALSAR 2009	HH, HV	0.25	11.84±0.82	-0.20±0.15	0.70±0.12		0.46	68.2	48.3%
		0.5	12.14±1.07	-0.32±0.22	0.79±0.17		0.56	59.2	42.2%
		1.0	12.77±1.41	-0.42±0.33	0.90±0.24		**0.62**	55.8	38.9%
UAVSAR 2009	HH, HV	0.25	11.92±0.61	-0.26±0.14	0.75±0.11		0.56	53.2	37.7%
		0.5	12.10±0.77	-0.29±0.18	0.79±0.14		0.61	47.5	33.8%
		1.0	12.34±1.08	-0.34±0.29	0.83±0.22		0.70	41.9	29.2%
	HH, HV,VV	0.25	11.90±0.62	-0.26±0.14	0.72±0.16	0.04±0.16	0.56	52.9	37.5%
		0.5	12.05±0.77	-0.28±0.18	0.70±0.20	0.11±0.20	0.62	46.7	33.3%
		1.0	12.28±1.13	-0.32±0.31	0.76±0.35	0.09±0.32	**0.72**	40.9	28.5%

*bolded is the best models; equations in form of AGB=exp($a+bx_1+cx_2+dx_3$);
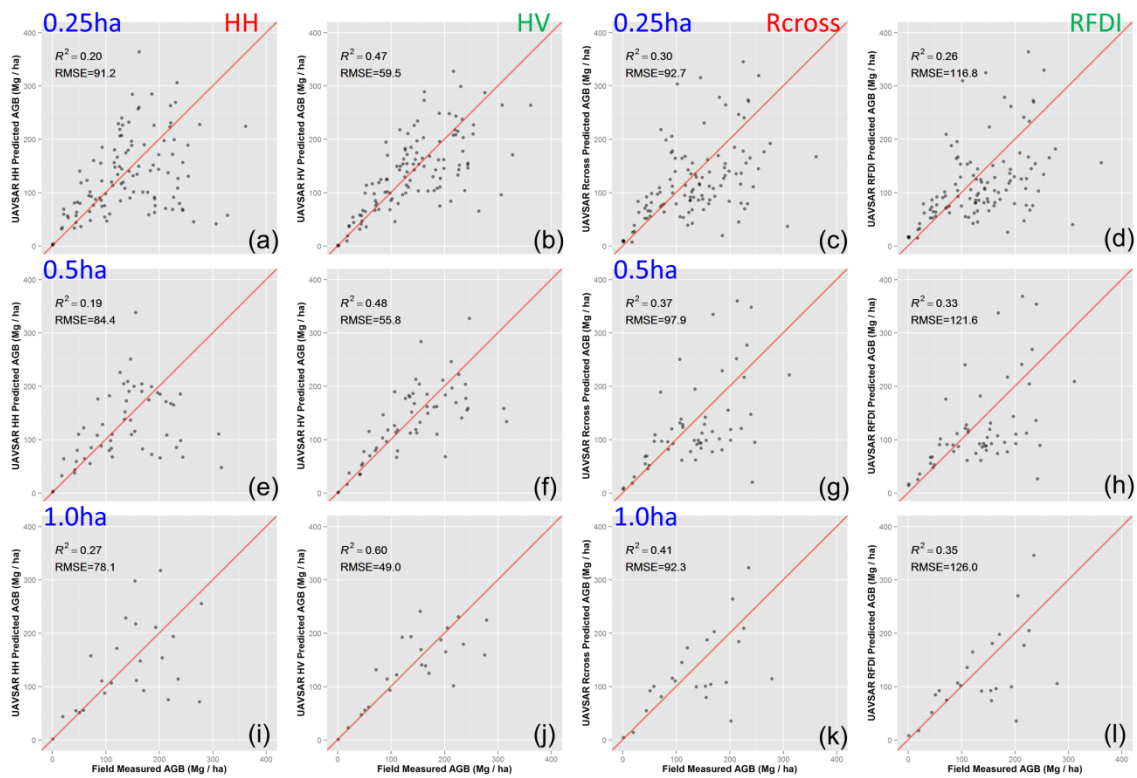
Figure 4-3. Model evaluation across different scales for UAVSAR 2009 data: HH and HV polarizations. UAVSAR 0.25 ha, 0.5 ha, and 1.0 ha plot-levels: (a) 0.25 ha HH, (b) 0.25 ha HV (c) 0.25 ha Rcross, (d) 0.25 ha RFDI, (e) 0.5 ha HH, (f) 0.5 ha HV (g) 0.5 ha Rcross, (h) 0.25 ha RFDI, (i) 1.0 ha HH, (j) 1.0 ha HV (k) 1.0 ha Rcross, and (l) 1.0 ha RFDI. X axis is the field-measured AGB density (Mg·ha^{-1}). Y axis is predicted AGB density (Mg·ha^{-1}). Red solid line is 1:1 line.
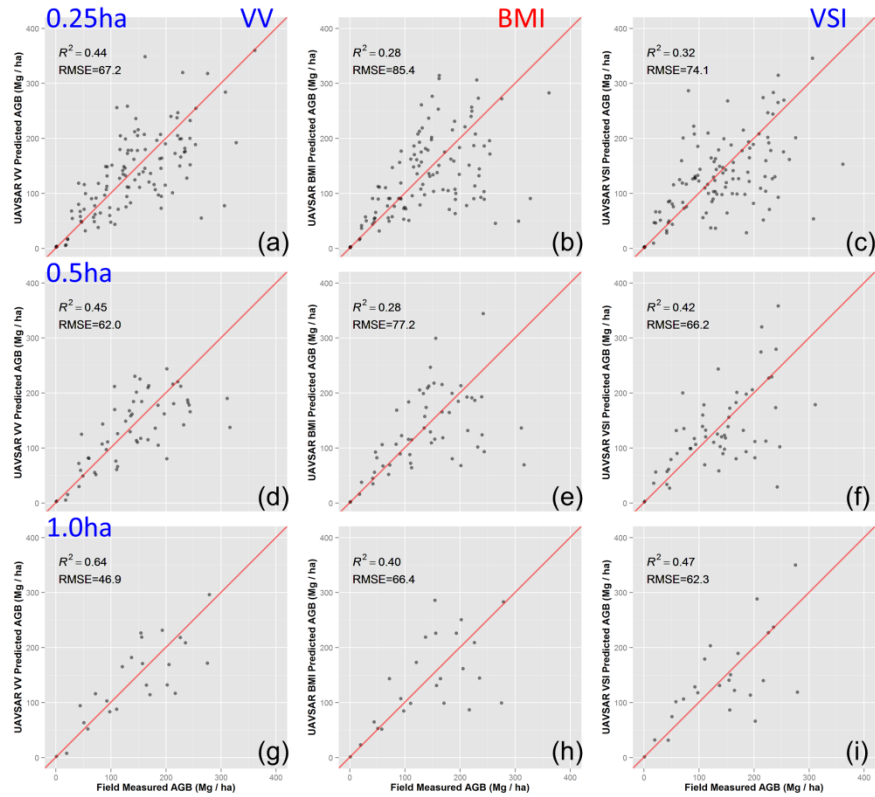
Figure 4-4. Model evaluation across different scale for UAVSAR 2009 data: VV polarization. UAVSAR 0.25 ha, 0.5 ha, and 1.0 ha plot-levels: (a) 0.25 ha VV, (b) 0.25 ha BMI (c) 0.25 ha VSI, (d) 0.5 ha VV, (e) 0.5 ha BMI, (f) 0.5 ha VSI, (g) 1.0 ha VV, (h) 1.0 ha BMI, and (i) 1.0 ha VSI. X axis is the field-measured AGB density (Mg·ha-1). Y axis is predicted AGB density (Mg·ha-1). Red solid line is 1:1 line.
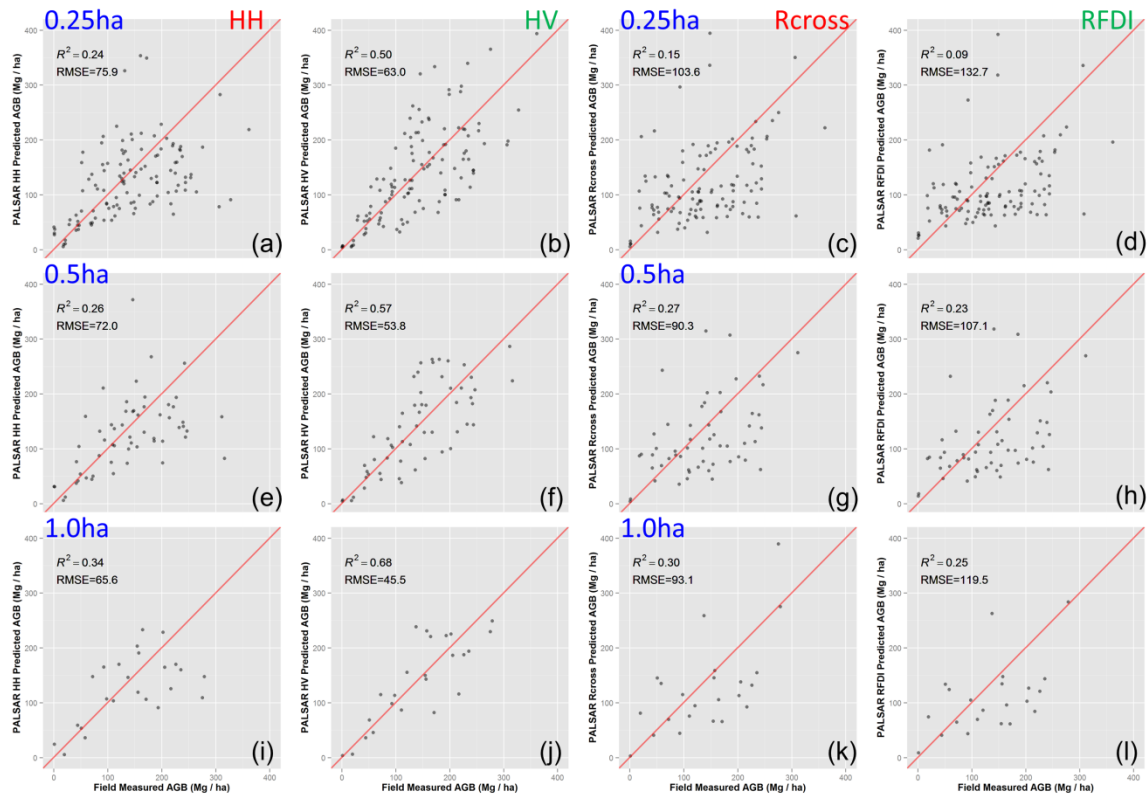
Figure 4-5. Model evaluation across different scale for PALSAR 2009 data: HH and HV polarizations. PALSAR 0.25 ha, 0.5 ha, and 1.0 ha plot-levels: (a) 0.25 ha HH, (b) 0.25 ha HV (c) 0.25 ha Rcross, (d) 0.25 ha RFDI, (e) 0.5 ha HH, (f) 0.5 ha HV (g) 0.5 ha Rcross, (h) 0.25 ha RFDI, (i) 1.0 ha HH, (j) 1.0 ha HV (k) 1.0 ha Rcross, and (l) 1.0 ha RFDI. X axis is the field-measured AGB density (Mg$\cdot$ha^{-1}). Y axis is predicted AGB density (Mg$\cdot$ha^{-1}). Red solid line is 1:1 line.
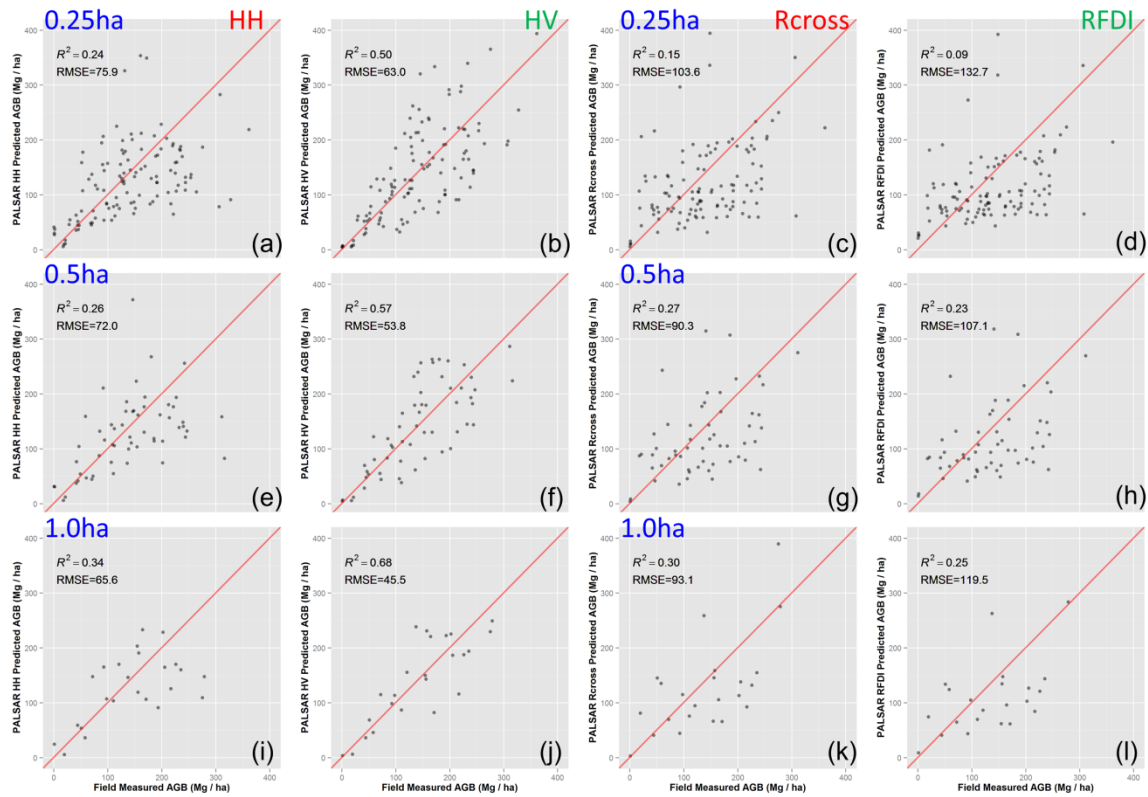
Figure 4-6. Model evaluation across different scale for PALSAR 2009 data: HH and HV polarizations. PALSAR 0.25 ha, 0.5 ha, and 1.0 ha plot-levels: (a) 0.25 ha HH, (b) 0.25 ha HV (c) 0.25 ha Rcross, (d) 0.25 ha RFDI, (e) 0.5 ha HH, (f) 0.5 ha HV (g) 0.5 ha Rcross, (h) 0.25 ha RFDI, (i) 1.0 ha HH, (j) 1.0 ha HV (k) 1.0 ha Rcross, and (l) 1.0 ha RFDI. X axis is the field measured AGB density ($Mg \cdot ha^{-1}$). Y axis is predicted AGB density ($Mg \cdot ha^{-1}$). Red solid line is 1:1 line.

4.4.3 Biomass mapping from multi-source SAR data

Exponential regression models were derived from field-measured biomass at the 1.0 ha plot-level and SAR backscatter at different polarizations. Specifically, two sets of models were developed: the PALSAR models for spaceborne systems (*i.e.*, SIR-C and PALSAR), and the UAVSAR models for airborne systems (*i.e.*, AIRSAR and UAVSAR). The models were applied to the corresponding SAR data, and biomass maps were generated at 100 m spatial resolution for the study site.

Biomass maps from SAR data were produced using the selected regression model (Figure 4-7a-d). The biomass map from LVIS data (Figure 4-7f) was produced using the RH50 regression model as described in Chapter 2. The biomass ranges up to 250 Mg·ha^{-1}, with a color of orange (0 - 50 Mg·ha^{-1}) to dark green (>250 Mg·ha^{-1}) indicating an increase of biomass. The overall patterns are similar in maps generated from spaceborne and airborne SAR data in 1994 and 2009. In both 1994 and 2009, high values of biomass (>200 Mg·ha^{-1}) were located in the near mature forests (outlined by pink polygon). Regions north of this undisturbed forest had lower values of biomass in 2009, corresponding to the disturbance detected by LTSS-VCT product. These patterns in 2009 were similar to the map derived from waveform LiDAR data (*i.e.*, LVIS in Chapter 2).
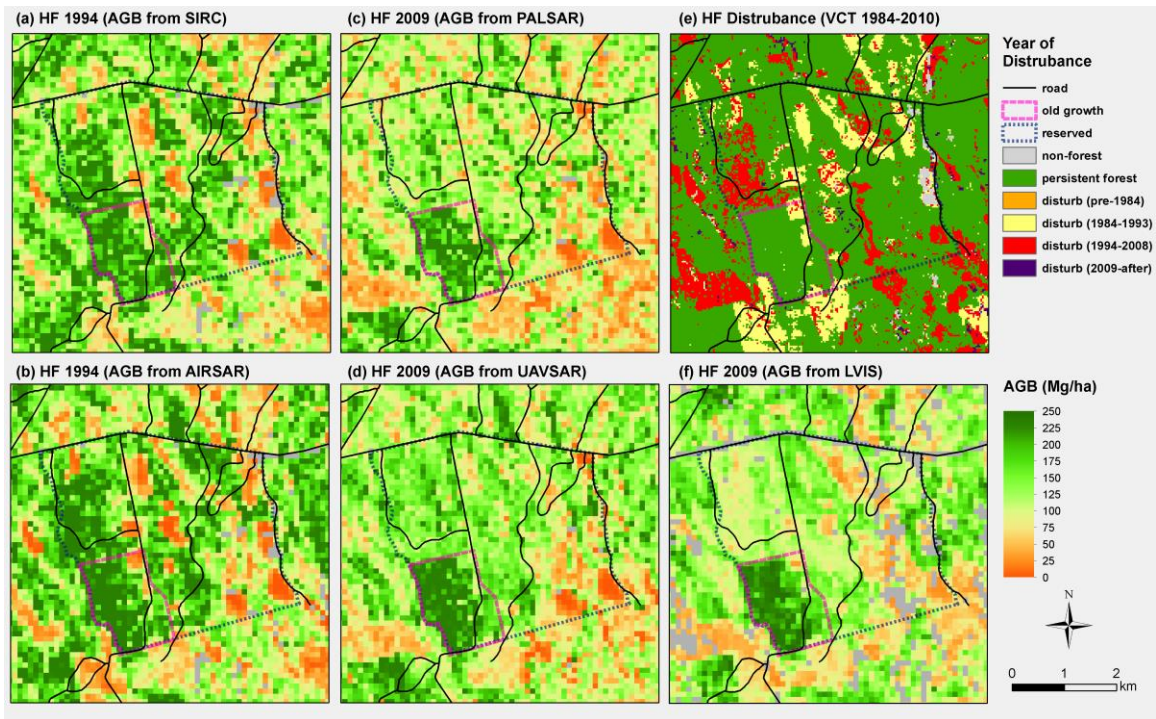
Figure 4-7. Forest biomass maps at 100 m resolution (1994-2009).
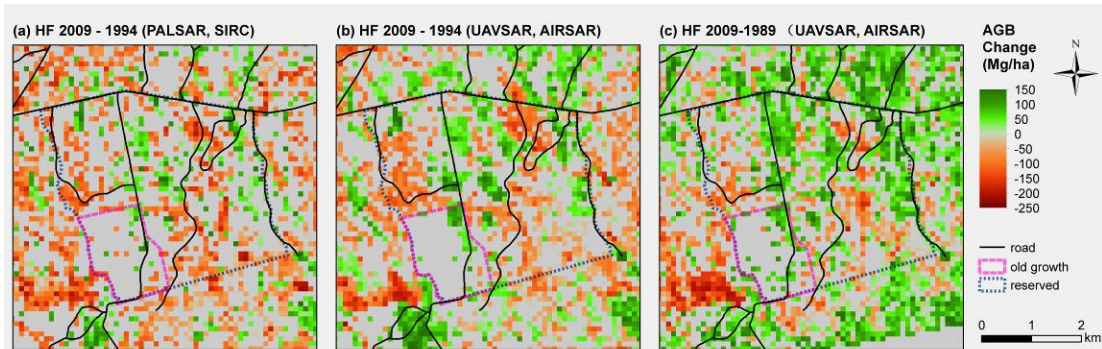
Figure 4-8. Change in biomass at HF site via cross-image normalized multi-source SAR data: (a) 2009PALSAR-1994SIR-C, (b) 2009UAVSAR-1994AIRSAR, and (c) 2009UAVSAR-1989AIRSAR. Maps are at 100 m spatial resolution, and with confidence interval (95%) is applied in predictions.

4.4.4   Biomass change mapping

Changes in biomass (green to red color) from 1994 to 2009 were derived at 100 m spatial resolution (Figure 4-8a & b). Confidence intervals (CI, 95%) of prediction were generated to exclude the predictions with overlapped values in two periods. Spatial patterns of changes in biomass derived from spaceborne and airborne systems are consistent with the forest disturbance patterns detected by the LTSS-VCT product (Figure 4-7c). Specifically, both change maps show the forest disturbance as well as the post-disturbance regrowth (*i.e.*, highlighted by red and green colors in Figure 4-7e). In addition, results from airborne systems (UAVSAR 2009 and AIRSAR 1994) reveal more detailed changes in biomass than those from spaceborne systems (PALSAR 2009 and SIR-C 1994).

4.5   *Discussion*

Our results highlight three important issues concerning the mapping of biomass and changes in biomass using L-band SAR data: (1) the effect of map scale on model accuracy and the errors from radar backscatter, (2) the effect of modeling approaches on the biomass estimation, and (3) the effect of errors in *in-situ* estimates of biomass.

4.5.1   Mapping scale and errors in radar data

Speckle noise in radar data is a critical factor affecting the application of SAR data in mapping of forest biomass. The improved accuracy in prediction models with the increase of plot sizes from 0.25 to 1.0 ha, was largely due to the reduction in geolocation errors and speckle noise. The decreasing trends in $RMSE_{CV}$ with increase of plot size are consistent in both spaceborne and airborne SAR systems. Previous studies *(Luckman et*

al., 1998; Saatchi et al., 2011a; Sumantyo and Amini, 2008) have indicated that to reduce the effect of speckle noise on biomass estimation, it is required to filter or aggregate the data to a certain map scale. The optimal pixel size or the equivalent number of multi-look (ENL) for biomass mapping from radar data is system dependent because nominal spatial resolutions vary among different SAR systems. For example, to develop a robust biomass prediction model, spaceborne PALSAR with an nominal ground range resolution of 12.5 m, is suggested to be aggregated to at least 75 m (~0.5 ha) *(Sun et al., 2011)*. While airborne UAVSAR, with a finer ground range resolution of 5 m, could be used at 50 m spatial resolution (0.25 ha) *(Zhang, 2011)*.

Multi-temporal and multi-looking-angle SAR data are found to be efficient in improving the accuracy in biomass estimates, because the averaging process reduces sensor calibration errors and influences from environment. However, the variances from multi-temporal data are uncertain and the underlining mechanisms are complicated because the changes in SAR backscattering depend on soil moisture and dielectric conditions which have not been well quantified spatially or temporally.

In addition, simulated errors (*i.e.*, 1 dB and 0.5 dB) from SAR data show that most of the estimated biomass from field measurement is within the error zones of HV model for PALSAR (Figure 4-9 & c) and UAVSAR (Figure 4-9 b & d). Results indicate that 0.5 dB or better radiometric calibration accuracy is required to generate a reliable HV model for biomass estimation. Recent spaceborne SAR systems such as PALSAR with a radiometric accuracy of 0.22 dB in the Amazon forest areas *(Shimada et al., 2009),* would meet for this requirement. However, the archived AIRSAR and SIR-C/XSAR data does not have a high enough radiometric accuracy. Therefore, mapping changes in

biomass using a combination of these datasets would have inherent errors from the remotely sensed data.

Due to limited co-incidence field measurements in our study site, we could not develop the direct change model as suggested in the previous study *(Dubayah et al., 2010)*. Instead, 0.25 to 1.0 ha plots were selected to develop uniform biomass equations using LOOCV method for spaceborne and airborne SAR data. The L-band airborne SAR data employed in this study were acquired using similar instruments (AIRSAR and UAVSAR). The sensor calibration accuracy improved over time for airborne as well as spaceborne instruments.

4.5.2 Errors in prediction models

Modeling approaches have influence on the values and distributions of predicted biomass. A 95% confidence interval of prediction is used here to present a range for the mean in the exponential HV models (blue dashed line in Figure 4-10). The confidence intervals are narrow at the lower range of biomass (*i.e.*, 0-150 Mg·ha^{-1}), however getting wider at the higher level of biomass (*i.e.*, >150 Mg·ha^{-1}).
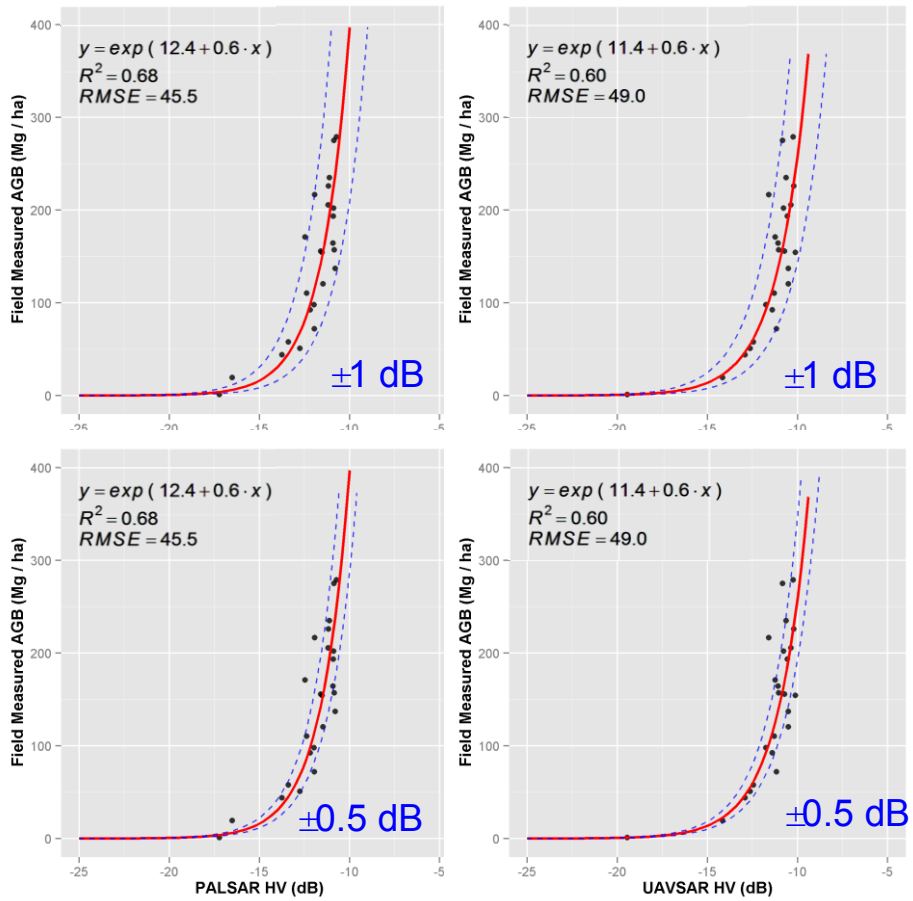
Figure 4-9. Simulated errors from SAR datasets: (a) PALSAR 2009 HV with ±1 dB error, (b) UAVSAR 2009 HV with ±1 dB error, (c) PALSAR 2009 HV with ±0.5 dB error, and (d) UAVSAR 2009 HV with ±0.5 dB error. Red solid line is the fitted regression model, and blue dashed lines show the SAR calibration error interval.
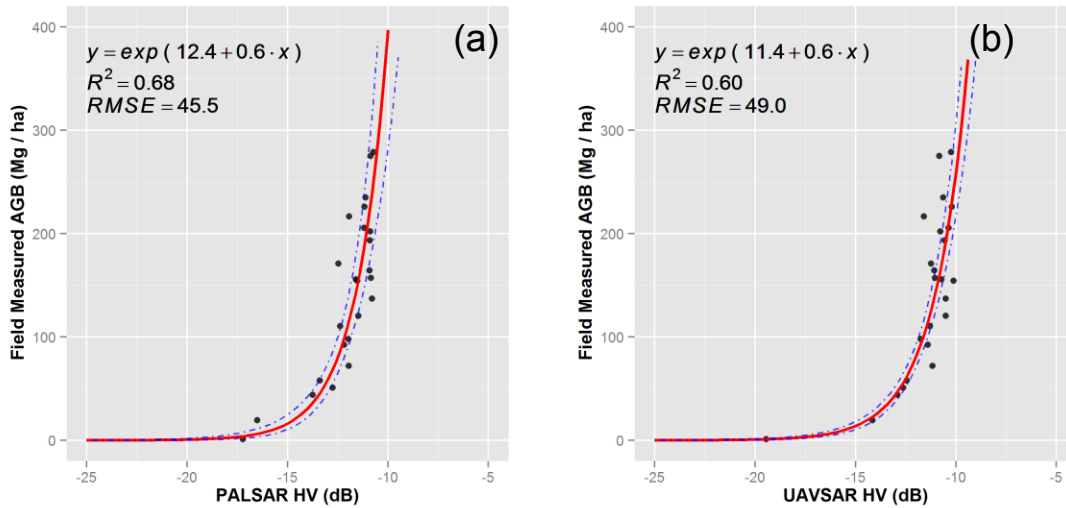
Figure 4-10. Errors from regression models: (a) PALSAR 2009 HV, (b) UAVSAR 2009 HV. Y axis is the field measured AGB density (Mg·ha^{-1}) at 1.0 ha plot-level. X axis is SAR backscatter at HV polarization in decibel (dB). Red solid line is the prediction curve, and blue dashed lines are the 95% confidence intervals of predictions.

The model evaluations show that HV models are the best among single-term models; and that HH+HV+VV models are the best among multi-variable models; and models that use dual or full polarization perform better than single polarization in estimation of biomass. The HV model is the best single-term prediction model for both spaceborne (*i.e.*, PALSAR) and airborne (*i.e.*, UAVSAR) SAR systems. The performance of all models were improved markedly with increase of plot sizes from 0.25 ha to 1.0 ha. At 1.0 ha plot-level, HV models derived from both spaceborne and airborne data agreed well with field estimates (R^2=0.68, $RMSE_{CV}$=45.5 Mg·ha^{-1}, $RMSE_{CV}$%=31.7%; and R^2=0.60, $RMSE_{CV}$=49.0 Mg·ha^{-1}, $RMSE_{CV}$%=34.2%). The HH+HV+VV model derived from airborne data corresponds better with field estimates at 1.0 ha plot-level than that of single-term models in terms of R^2 as well as RMSE (R^2=0.72, $RMSE_{CV}$=40.9 Mg·ha^{-1}, $RMSE_{CV}$%=28.5%).

4.5.3 Uncertainty in *in-situ* estimates

In this study, the same year (2009) *in-situ* data and SAR backscatter were selected to develop regression models. Therefore, the time-shift between *in-situ* and *RS* measurements was minimized. Careful selection of suitable allometric equations for specific study sites is critical for a robust estimate of biomass. The choice of DBH based allometric equations have influences on the estimated field biomass (Appendix Figure 5-1). The difference between two allometric equations (Jenkins and Young) for our study sites is within 5% at 0.25 ha, 0.5 ha, and 1.0 ha plot-level. However, larger uncertainties are found in a higher range of biomass, and this could potentially increase the uncertainty in the produced biomass map.

4.6   Conclusion

Exponential regression models were used for mapping changes in forest biomass at a medium spatial resolution (100 m) using multi-source spaceborne and airborne SAR data over 15- and 20- year periods. Results from this study demonstrated the ability of multi-source SAR data to monitor changes in forest biomass, and assess the changes in forest carbon budget.

Changes mapped using archived SAR dataset (*i.e.*, AIRSAR and SIR-C/XSAR) have uncertainties from sensor calibration error, and the timing of data acquisition limits the application of multi-temporal monitoring. When the period between the dates of two or multiple sets is too short, the loss of carbon from forest disturbance is not measurable (above the measurement error). Conversely, the gain of carbon from forest stand regrowth will be beyond the detectable range due to saturation. Results from this study

improved our knowledge about L-band SAR's capability to monitor changes in biomass from forest disturbance and post-disturbance recovery.

Several current and future spaceborne SAR systems will continue to provide data for these types of studies. The ALOS PALSAR-2 launched in 2014 provides full polarizations at high spatial resolution (<10 m) and has a 14-day repeat cycle to monitor forest carbon changes *(Shimoda and Xiong, 2012)*. The NASA-ISRO Synthetic Aperture Radar (NISAR, targeted to launch in 2020) mission is designed to carry an L-band and S-band SAR to make global measurements. Future soil moisture products with a better spatial resolution (~3 km) will be available from Soil Moisture Active Passive (SMAP, launched in 2015) mission. This will improve the biomass predictions from SAR data by reducing the effects of surface wetness. Findings from this study provide calibration and validation methods as the foundation for improving the performance of current and future spaceborne system.

Chapter 5 Summary of Findings, Contributions and Future Research Directions

Mapping biomass and changes in biomass over relatively short time scales is a challenging task, yet it is crucial in order to obtain a better understanding of the effects of forest disturbance and post-disturbance regrowth on the terrestrial carbon cycle. Current approaches using active remote sensing for biomass dynamic studies explored mostly local to regional scales due to data limitations. There is additionally a strong and growing need to develop effective mapping and assessment at a national to continental scale in support of climate treaty frameworks such as REDD+ *(Goetz and Dubayah, 2011)*. The work presented in this dissertation investigates LiDAR and SAR remote sensing approaches to this problem at selected study sites.

In this dissertation, multi-temporal waveform LiDAR and multi-source SAR data were applied to map forest biomass and its changes at different key map scales for the two study sites: Howland Forest and Penobscot Experimental Forest. The main goals were to map changes in forest biomass from waveform LiDAR data and assess the loss from disturbance and the gain from post-disturbance recovery, analyze the sensitivity of SAR signatures to changes in forest biomass and the major influence factors including incidence angle, soil moisture and disturbance type, and finally map changes in biomass using multi-source SAR data from spaceborne and airborne platforms.

Major findings and contributions of this dissertation are summarized in sections 5.1 and 5.2, and future research directions are described in section 5.3.

5.1   *Major findings*

Chapter 2 to Chapter 4 of this dissertation explored approaches for biomass estimation from LiDAR and SAR data, and revealed the limitations of using a single-sensor approach. Discussion of the problems that need to be dealt with led to key insights into LiDAR and SAR data acquisition and processing relevant to future projects to support climate treaties such as REDD+. Specifically, the main findings and significance are summarized as follows.

Firstly, biomass prediction models at waveform LiDAR footprint-level were developed and then applied to assess the change in biomass at 1.0 ha map scale. The disturbance-specific models were found to be significantly different at footprint-level and the effects of disturbance on the biomass estimations gradually diminished with the increase of plot sizes from 0.25 ha to 1 ha. Evaluation of models indicated an improved accuracy with increasing plot sizes, and agreed well with field estimates at 1 ha plot-level (R^2=0.91, 22.4 Mg·ha^{-1}, 15.6%). Moreover, prediction errors from waveform LiDAR were minimized when footprint coverage approached about 50% of the area of 1 ha plots (16 footprints) with no improvement beyond that.

Secondly, the sensitivity analysis of forest biomass to SAR backscattering was conducted to investigate: 1) the influence of factors other than the change in forest biomass (i.e., radiometric distortion caused by incidence angle and soil moisture) on SAR backscatter; 2) the feasibility of cross-image normalization between multi-temporal and multi-sensor SAR data; and 3) the possibility of applying normalized backscatter to detect changes in biomass due to forest disturbance and post-disturbance recovery. Results from the cross-image normalization indicated that: 1)

the effect of incidence angle on SAR backscatter could be reduced to less than 1 dB by the correction model for airborne SAR data, and 2) over 50% of the changes in SAR backscatter due to soil moisture could be eliminated by the proposed cross-image normalization procedure, and 3) changes in forest biomass above 100 Mg ħa^{-1} or greater than 50% (biomass limited to 250 Mg ħa^{-1}) are detectable using the cross-normalized SAR data.

Lastly, the changes in forest biomass over the study sites were mapped at 100 m spatial resolution for periods of a 15-year period using spaceborne data and a 20-year period using airborne data. Results highlighted important issues concerning the mapping process using L-band SAR data: 1) speckle noise in radar data as well as geolocation errors were reduced with the increase of plot sizes from 0.25 ha to 1 ha, and 2) multi-variable models were found to outperform the single-term models developed for biomass estimation using either spaceborne or airborne data. At 1 ha plot-level, multi-variable models using spaceborne and airborne data agreed better with field estimates (R^2=0.62, RMSEcv=55.8 Mg·ha^{-1}, 38.9%; and R^2=0.72, RMSEcv=40.9 Mg·ha^{-1}, 28.5%) than single-term HV models (R^2=0.68, RMSEcv=45.5 Mg·ha^{-1}, 31.7%; and R^2=0.60, RMSEcv=49.0 Mg·ha^{-1}, 34.2%).

5.2   *Major contributions*

This study mapped changes in biomass from LiDAR data in Chapter 2, analyzed sensitivity of SAR backscatter to biomass in Chapter 3, and mapped changes in forest biomass using multi-source SAR data in Chapter 4. The major contributions are:

- No reliable models at waveform LiDAR footprint-level models for biomass and change mapping have been developed previously. This study indicates that prediction models at the scale of individual LVIS footprints are reliable when geolocation errors are minimized, and suggests a certain density of LVIS footprints is required for mapping biomass dynamics.

- This study attempts to minimize the influence of incidence angle and soil moisture on SAR backscatter for estimation of biomass. The normalization algorithms to reduce effects of incidence angle and soil moisture are not bound by a specific sensor.

- No previous research has been conducted to map the changes in forest biomass from forest disturbance and post-disturbance recovery using multi-source L-band SAR data. This dissertation study provides a detailed case study and may stimulate new interest in studies on forest biomass dynamics from SAR data.

5.3   *Future research directions*

This dissertation is a preliminary study in mapping changes in biomass after forest disturbance over a temperate forest using LiDAR and SAR remote sensing. Results from this study improve our knowledge concerning waveform LiDAR and L-band SAR's capability in monitoring and assessment of net carbon budget from forest disturbance and post-disturbance recovery. Findings from this study provide calibration and validation methods as a foundation for improving the performance of current and future spaceborne systems.

Experiments with repeat LiDAR in Chapter 2 have demonstrated the ability of LiDAR to monitor and assess changes in biomass after forest disturbance. The

sensitivity analysis and discussions in Chapter 3 and Chapter 4 have indicated the importance of integrating multi-sensor and multi-source remote sensing data to produce accurate estimates at a local to regional scale. Although radar data outperform optical data by penetrating through clouds for forest applications, it also has limitations and complexities. Combined multi-temporal SAR data will improve single date estimates for biomass. Also, recent studies have indicated that synergic use of LiDAR, SAR and InSAR has great potential in reducing uncertainties in biomass estimates. The vertical vegetation structure (*i.e.*, canopy height) can also be derived from InSAR or optical stereo images. More studies are going on in this area, and ecosystem models which provide the relationships between vegetation attributes are being used for attribute estimates and predictions under different scenarios.

Moreover, several ongoing spaceborne LiDAR and SAR missions guarantee the continuation of this work in terms of mapping forest biomass and the changes in biomass. For example, the NASA Earth Venture Program recently has selected the Global Ecosystem Dynamics Investigation (GEDI) Lidar with multiple laser beams, which is based on the high-SNR waveform profile LVIS, to measure forest structures and surface topography at high resolution from the International Space Station (ISS) *(Blair et al., 2014; Dubayah et al., 2014)*. GEDI will be launched as early as 2018 to provide billions of vegetation height and structure measurements for the precise estimation of biomass within the orbital coverage provided by ISS (+/- 51.6 degrees latitude). On the other hand, several spaceborne SAR missions provide more opportunities in mapping forest biomass using SAR remote sensing. The potential for multi-source L-band SAR to estimate forest biomass at global level will be increased

115

as ALOS/PALSAR-2 and NISAR become operational and provide data comparable to existed ALOS-PALSAR and SIR-C/XSAR data archives.

Ultimately, there still exist areas for continued investigation before we can confidently map biomass dynamics using remotely sensed data at policy-relevant scales (e.g., regional, national to continental scales) with the required accuracy in a consistent and transparent framework. LiDAR and SAR remote sensing are relatively new for the vegetation community, and the lack of consistent and continuous observation leads to large uncertainties in different studies. We anticipate more researches will improve our ability in reducing these uncertainties.

Glossary

AFM	American Forest Management
AGB	Aboveground Biomass
AIRSAR	AIRborne Synthetic Aperture Radar
ALOS	Advanced Land Observing Satellite
ALTM	Airborne Laser Terrain Mappers
ASF	Alaska Satellite Facility
BGB	Belowground Biomass
BOREAS	Boreal Ecosystem-Atmosphere Study
ESA	European Space Agency
REDD+	Reduced Emissions from Deforestation and Forest Degradation Plus
DBH	Diameter at Breast Height
FIA	Forest Inventory and Analysis
GEDI	Global Ecosystem Dynamics Investigation
InSAR	Interferometric Synthetic Aperture Radar
JAXA	Japan Aerospace Exploration Agency
JERS-1	Japanese Earth Resources Satellite 1
JPL	Jet Propulsion Laboratory
LiDAR	Light Detection and Ranging
LULCC	Land Use and Land-Cover Change
LUT	Look Up Table
LVIS	LiDAR Vegetation an Imaging Sensor

NASA	National Aeronautics and Space Administration
NED	National Elevation Dataset
NISAR	NASA-ISRO Synthetic Aperture Radar
NLCD	National Land Cover Data
PALSAR	Phased Array type L-band Synthetic Aperture Radar
PolSAR	Polarimetric Synthetic Aperture Radar
Radar	Radio Detection and Ranging
SAR	Synthetic Aperture Radar
SIR-C/XSAR	Spaceborne Imaging Radar-C and X-Band SAR
RTM	Radiative Transfer Model
UAVSAR	Uninhabited Aerial Vehicle Synthetic Aperture Radar
LTSS-VCT	Landsat Series Stack- Vegetation Change Tracker

Appendices
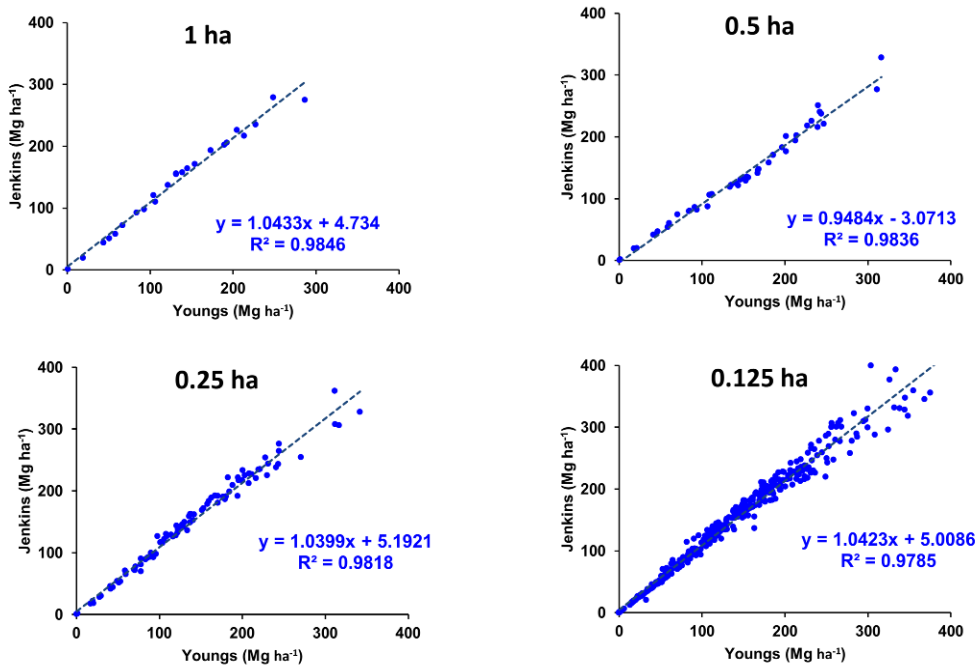
Figure 5-1. Fied estimated biomass from national equations as a function of regional equations across different plot-levels at HF and PEF sites: (a) 1.0 ha, (b) 0.5 ha, (c) 0.25 ha, and (d) 0.125 ha.
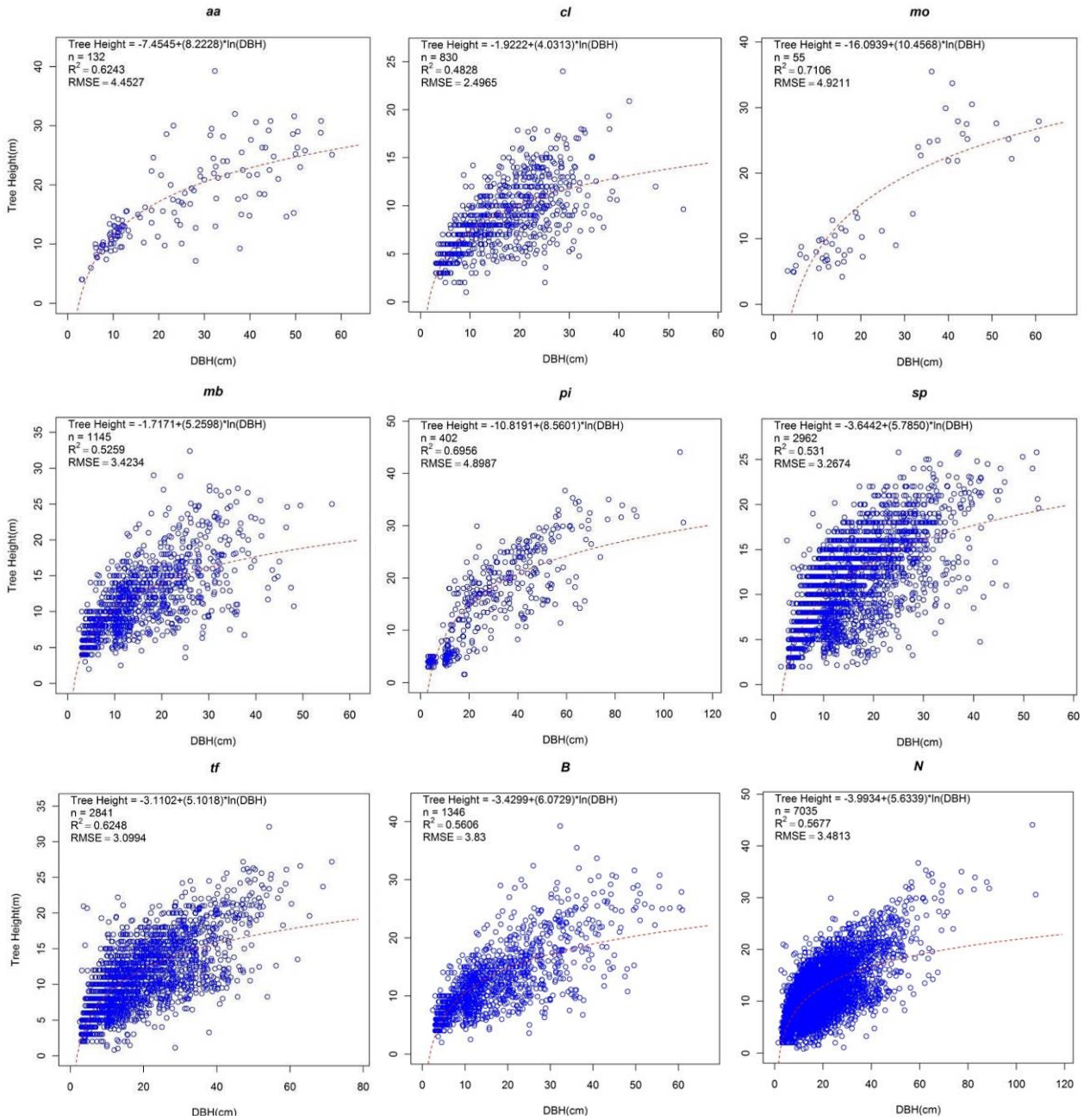
Figure 5-2. Tree height as a funciton of DBH by: (a) seven species groups from Jenkins, and (b) two general species groups.

Species group:
aa = aspen / alder / cottonwood / willow; cl = cedar / larch; mo = hard maple / oak / hickory / beech;
mb = soft maple / birch; pi = pine; sp = spruce; tf = true fir / hemlock;
B = broadleaf; N = needleleaf;

120
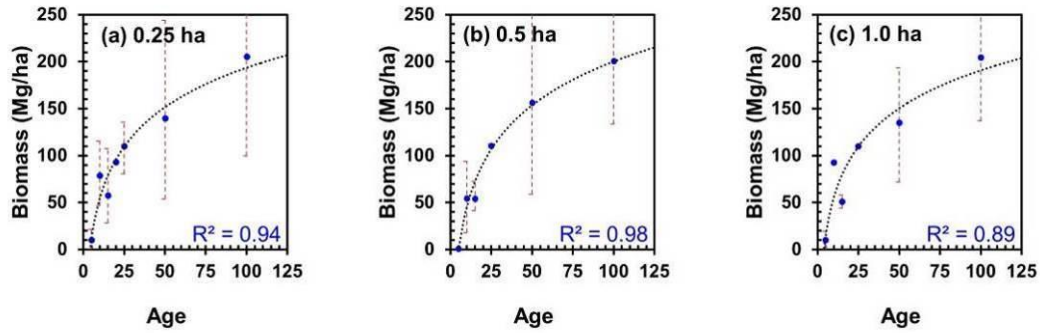
Figure 5-3. Growth curve with age from LTSS-VCT and field estimated biomass: (a) 0.25 ha plot, (b) 0.5 ha plot, (c) 1.0 ha plot. X axis represents age classes in an interval of 5 year, with classes as 0-5, 5-10, …, 100. Age 100 indicated that the plots haven't been disturbed from 1900s according to management record. Y axis represents mean AGB at plot-level. Blue dots show mean values for each age class, with dashed bars are variance.
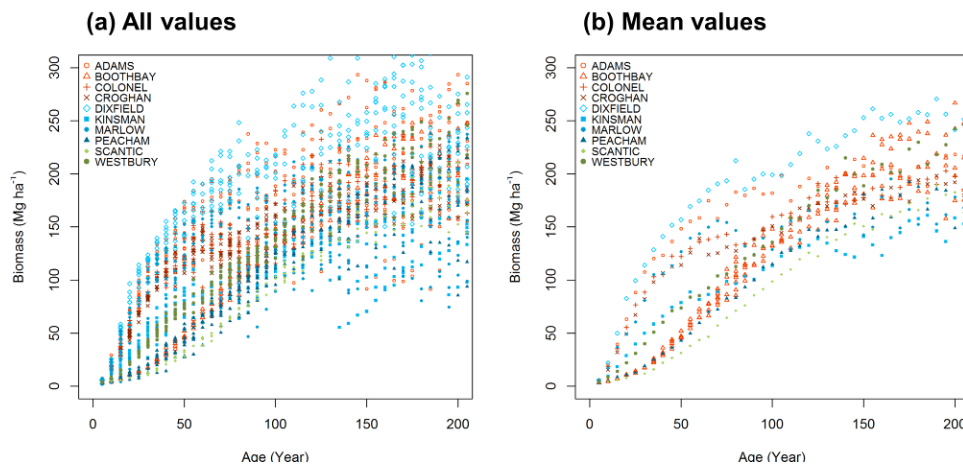
Figure 5-4. Growth curve with age and biomass from ZELIG model simulation: (a) all values, and (b) mean values of each soil classes. ADAMS to WESTBURY are 10 different type of soil based on drainage and taxonomic classification.

121

Table 5-1. Allometric equations for biomass estimation in this study

Jenkins*	Code	Genus	Species	Common name	Young[1]		Jenkins[2]	
					b0	b1	b0	b1
tf	ABBA	Abies	*balsamea*	Balsam fir	0.5958	2.4017	-2.5384	2.4814
mb	ACRU	Acer	*rubrum*	Red maple	0.9392	2.3804	-1.9123	2.3651
mb	BEAL	Betula	*alleghaniensis*	Yellow birch	1.1297	2.3376	-1.9123	2.3651
mb	BEPA	Betula	*papyrifera*	Paper birch	0.4792	2.6634	-1.9123	2.3651
mb	BEPO	Betula	*populifolia*	Grey birch	1.0931	2.3146	-1.9123	2.3651
mo	FAGR	Fagus	*grandifolia*	Beech	1.3303	2.2988	-2.0127	2.4342
mh	FRAM	Fraxinus	*americana*	White ash	/	/	-2.4800	2.4835
sp	PIRU	Picea	*rubens*	Red spruce	0.8079	2.3316	-2.0773	2.3323
pi	PIST	Pinus	*strobus*	White pine	0.4080	2.4490	-2.0773	2.3323
aa	POGR	Populus	*grandidentata*	Big-toothed aspen	0.4689	2.6087	-2.2094	2.3867
aa	POTR	Populus	*tremuloides*	Trembling aspen	0.4689	2.6087	-2.2094	2.3867
cl	THOC	Thuja	*occidentalis*	Northern white cedar	1.1182	1.9269	-2.0336	2.2592
tf	TSCA	Tsuga	*canadensis*	Hemlock	0.6803	2.3617	-2.5384	2.4814
mh	UNK	/	/	/	/	/	-2.4800	2.4835

[1] Young, Ribe, and Wainwright 1980 *(Young et al., 1980)* weight tables for tree and shrub species in Maine

$B \text{ (kg)} = \exp(b0+b1*\ln(dbh/2.54))*0.4536$; where 2.54 and 0.4536 are the factors to convert inch to cm, ln = natural log base "e" (2.718282)

[2] Jenkins equations *(Jenkins et al., 2003)* for national-scale biomass estimation

$B \text{ (kg)} = \exp(b0+b1*\ln(dbh))$

*Jenkins abbreviations:

aa = aspen / alder / cottonwood / willow; cl = cedar / larch; df = douglas-fir; mb = soft maple / birch; mh = mixed hardwood;

mo = hard maple / oak / hickory / beech; pi = pine; sp = spruce; tf = true fir / hemlock; wo = woodland species (juniper / oak / mesquite);

Table 5-2. DBH-based Height Equations from Field Measurements (1989 to 2010)

Research site	Code	Species group	Parameter		DBH		Height		n	R^2	RMSE	p
			a	b	min	max	min	max				
Howland	DB	Deciduous Broadleaf	-3.4299	6.0729	2.5	60.9	2.0	39.3	1346	0.5606	3.83	<0.001
Howland	EN	Evengreen Needleleaf	-3.9934	5.6339	1.5	108.0	0.8	44.1	7035	0.5677	3.48	<0.001
Howland	aa	Aspen / alder / cottonwood / willow	-7.4545	8.2228	3.1	58.0	4.0	39.3	132	0.6243	4.45	<0.001
Howland	mb	Soft maple / birch	-1.7171	5.2598	2.5	56.2	2.0	32.4	1145	0.5259	3.42	<0.001
Howland	mo	Hard maple / oak / hickory / beech	-16.0939	10.4568	3.2	60.7	4.2	35.5	55	0.7106	4.92	<0.001
Howland	cl	Cedar / larch	-1.9222	4.0313	3.1	53.0	1.0	24.0	830	0.4828	2.50	<0.001
Howland	tf	Douglas-fir	-3.1102	5.1018	2.6	71.4	0.8	32.1	2841	0.6248	3.10	<0.001
Howland	pi	Pine	-10.8191	8.5601	3.0	108.0	1.6	44.1	402	0.6956	4.90	<0.001
Howland	sp	Spruce	-3.6442	5.7850	1.5	53.0	2.0	25.8	2962	0.5310	3.27	<0.001

Diameter at breast height (dbh) equation: h = a*ln(dbh)+b

Where dbh = diameter at breast height (cm, at height = 1.37 m), h = height (m)

n = number of trees in sample;

R^2 = coefficient of determination;

RMSE = root mean squared error or estimate of the standard deviation of the regression error term;

p = significant level;

Include both hardwood and softwood species from dryland forest

Bibliography

Ahmed, R., Siqueira, P., & Hensley, S. (2014). Analyzing the Uncertainty of Biomass Estimates From L-Band Radar Backscatter Over the Harvard and Howland Forests. *IEEE Transactions on Geoscience and Remote Sensing, 52*, 3568-3586

Almeida-Filho, R., Shimabukuro, Y.E., Rosenqvist, A., & Sánchez, G.A. (2009). Using dual-polarized ALOS PALSAR data for detecting new fronts of deforestation in the Brazilian Amazônia. *International Journal of Remote Sensing, 30*, 3735-3743

Anderson, J., Martin, M.E., Smith, M.L., Dubayah, R.O., Hofton, M.A., Hyde, P., Peterson, B.E., Blair, J.B., & Knox, R.G. (2006). The use of waveform lidar to measure northern temperate mixed conifer and deciduous forest structure in New Hampshire. *Remote Sensing of Environment, 105*, 248-261

Anderson, J.E., Plourde, L.C., Martin, M.E., Braswell, B.H., Smith, M.-L., Dubayah, R.O., Hofton, M.A., & Blair, J.B. (2008). Integrating waveform lidar with hyperspectral imagery for inventory of a northern temperate forest. *Remote Sensing of Environment, 112*, 1856-1870

Asner, G.P., Mascaro, J., Muller-Landau, H.C., Vieilledent, G., Vaudry, R., Rasamoelina, M., Hall, J.S., & van Breugel, M. (2012). A universal airborne LiDAR approach for tropical forest carbon mapping. *Oecologia*, 1-14

Asner, G.P., Powell, G.V.N., Mascaro, J., Knapp, D.E., Clark, J.K., Jacobson, J., Kennedy-Bowdoin, T., Balaji, A., Paez-Acosta, G., Victoria, E., Secada, L., Valqui, M., & Hughes, R.F. (2010). High-resolution forest carbon stocks and emissions in the Amazon. *Proceedings of the National Academy of Sciences, 107*, 16738-16742

Balzter, H., Skinner, L., Luckman, A., & Brooke, R. (2003). Estimation of tree growth in a conifer plantation over 19 years from multi-satellite L-band SAR. *Remote Sensing of Environment, 84*, 184-191

Blair, J., Dubayah, R., Hofton, M., Luthcke, S., Rabine, D., Wake, S., Coyle, B., Stysley, P., & Salerno, C. (2014). Full-waveform Airborne and Spaceborne Laser Altimetry for Mapping and Sampling the Earth's Forests, Cryosphere, and Land surfaces. In, *AGU*. San Francisco, USA

Blair, J.B., & Hofton, M.A. (1999). Modeling laser altimeter return waveforms over complex vegetation using high-resolution elevation data. *Geophys. Res. Lett., 26*, 2509-2512

Blair, J.B., Hofton, M.A., & Rabine, D.L. (2006). Processing of NASA LVIS elevation and canopy (LGE, LCE and LGW) data products, version 1.02. In G. NASA Goddard Space Flight Cent., Md (Ed.)

Blair, J.B., Rabine, D.L., & Hofton, M.A. (1999). The Laser Vegetation Imaging Sensor: a medium-altitude, digitisation-only, airborne laser altimeter for mapping vegetation and topography. *ISPRS Journal of Photogrammetry and Remote Sensing, 54*, 115-122

Botkin, D.B., & Simpson, L.G. (1990). Biomass of the North American Boreal Forest: A Step toward Accurate Global Measures. *Biogeochemistry, 9*, 161-174

Bourgeau-Chavez, L.L., Leblon, B., Charbonneau, F., & Buckley, J.R. (2013). Evaluation of polarimetric Radarsat-2 SAR data for development of soil moisture retrieval algorithms over a chronosequence of black spruce boreal forests. *Remote Sensing of Environment, 132*, 71-85

Canadell, J.G., & Raupach, M.R. (2008). Managing Forests for Climate Change Mitigation. *Science, 320*, 1456-1457

Collins, J.N., Hutley, L.B., Williams, R.J., Boggs, G., Bell, D., & Bartolo, R. (2009). Estimating landscape-scale vegetation carbon stocks using airborne multi-frequency polarimetric synthetic aperture radar (SAR) in the savannahs of north Australia. *International Journal of Remote Sensing, 30*, 1141-1159

Dobson, M.C., Ulaby, F.T., LeToan, T., Beaudoin, A., Kasischke, E.S., & Christensen, N. (1992). Dependence of radar backscatter on coniferous forest biomass. *IEEE Transactions on Geoscience and Remote Sensing, 30*, 412-415

Dobson, M.C., Ulaby, F.T., Pierce, L.E., Sharik, T.L., Bergen, K.M., Kellndorfer, J., Kendra, J.R., Li, E., Lin, Y.C., Nashashibi, A., Sarabandi, K., & Siqueira, P. (1995). Estimation of forest biophysical characteristics in Northern Michigan with SIR-C/X-SAR. *IEEE Transactions on Geoscience and Remote Sensing, 33*, 877-895

Drake, J.B., Dubayah, R.O., Clark, D.B., Knox, R.G., Blair, J.B., Hofton, M.A., Chazdon, R.L., Weishampel, J.F., & Prince, S. (2002). Estimation of tropical forest structural characteristics using large-footprint lidar. *Remote Sensing of Environment, 79*, 305-319

Drake, J.B., Knox, R.G., Dubayah, R.O., Clark, D.B., Condit, R., Blair, J.B., & Hofton, M. (2003). Above-ground biomass estimation in closed canopy Neotropical forests using lidar remote sensing: factors affecting the generality of relationships. In, *Global Ecology and Biogeography* (pp. 147-159): Wiley-Blackwell

Dubayah, R., Goetz, S., Blair, J.B., Luthcke, S., Healey, S., Hansen, M., Hofton, M., Hurtt, G., Kellner, J., & Fatoyinbo, T. (2014). The Global Ecosystem Dynamics Investigation (GEDI) Lidar. In, *ForestSAT2014 Open Conference System*

Dubayah, R.O., & Drake, J.B. (2000). Lidar Remote Sensing for Forestry. *Journal of Forestry, 98*, 44-46

Dubayah, R.O., Sheldon, S.L., Clark, D.B., Hofton, M.A., Blair, J.B., Hurtt, G.C., & Chazdon, R.L. (2010). Estimation of tropical forest height and biomass dynamics using lidar remote sensing at La Selva, Costa Rica. *Journal of Geophysical Research, 115*, G00E09

Dubois, P.C., & Norikane, L. (1987). Data volume reduction for imaging radar polarimetry. In, *IGARSS Symposium*

Englhart, S., Keuck, V., & Siegert, F. (2011). Aboveground biomass retrieval in tropical forests -- The potential of combined X- and L-band SAR data use. *Remote Sensing of Environment, 115*, 1260-1271

Evans, A., & Perschel, R. (2009). A review of forestry mitigation and adaptation strategies in the Northeast U.S. *Climatic Change, 96*, 167-183

Frazer, G.W., Magnussen, S., Wulder, M.A., & Niemann, K.O. (2011). Simulated impact of sample plot size and co-registration error on the accuracy and uncertainty of LiDAR-derived estimates of forest stand biomass. *Remote Sensing of Environment, 115*, 636-649

Gens, R., & Logan, T. (2003). Alaska Satellite Facility Software Tools: Manual In G. Institution (Ed.). Fairbanks, AK, USA: University of Alaska

Goetz, S., & Dubayah, R. (2011). Advances in remote sensing technology and implications for measuring and monitoring forest carbon stocks and change. *Carbon Management, 2*, 231-244

Gonçalves, F.G., Santos, J.R., & Treuhaft, R.N. (2011). Stem volume of tropical forests from polarimetric radar. *International Journal of Remote Sensing, 32*, 503-522

Gonzalez, P., Asner, G.P., Battles, J.J., Lefsky, M.A., Waring, K.M., & Palace, M. (2010). Forest carbon densities and uncertainties from Lidar, QuickBird, and field measurements in California. *Remote Sensing of Environment, 114*, 1561-1575

Guo, Y., Shi, Z., Zhou, L.-q., Jin, X., Tian, Y.-f., & Teng, H.-f. (2013). Integrating Remote Sensing and Proximal Sensors for the Detection of Soil Moisture and Salinity Variability in Coastal Areas. *Journal of Integrative Agriculture, 12*, 723-731

Hall, F.G., Bergen, K., Blair, J.B., Dubayah, R., Houghton, R., Hurtt, G., Kellndorfer, J., Lefsky, M., Ranson, J., Saatchi, S., Shugart, H.H., & Wickland, D. (2011). Characterizing 3D vegetation structure from space: Mission requirements. *Remote Sensing of Environment, 115*, 2753-2775

Harrell, P.A., Kasischke, E.S., Bourgeau-Chavez, L.L., Haney, E.M., & Christensen Jr, N.L. (1997). Evaluation of approaches to estimating aboveground biomass in Southern pine forests using SIR-C data. *Remote Sensing of Environment, 59*, 223-233

Heath, L.S., Hansen, M., Smith, J.E., Miles, P.D., & Smith, B.W. (2008). Investigation into calculating tree biomass and carbon in the FIADB using a biomass expansion factor approach. *McWilliams, WH, Moisen, GG & Czaplewski, RL (eds.)*

Henderson, F.M., & Lewis, A.J. (1998). *Manual of Remote Sensing: Principles and Applications of Imaging Radar*. New York: John Wiley and Sons

Hollinger, D.Y., Goltz, S.M., Davidson, E.A., Lee, J.T., Tu, K., & Valentine, H.T. (1999). Seasonal patterns and environmental control of carbon dioxide and water vapour exchange in an ecotonal boreal forest. *Global Change Biology, 5*, 891-902

Houghton, R., House, J., Pongratz, J., Van Der Werf, G., DeFries, R., Hansen, M., Quéré, C.L., & Ramankutty, N. (2012). Carbon emissions from land use and land-cover change. *Biogeosciences, 9*, 5125-5142

Houghton, R.A., Hall, F., & Goetz, S.J. (2009). Importance of biomass in the global carbon cycle. *Journal of Geophysical Research: Biogeosciences, 114*, G00E03

Huang, C., Goward, S.N., Masek, J.G., Thomas, N., Zhu, Z., & Vogelmann, J.E. (2010). An automated approach for reconstructing recent forest disturbance history using dense Landsat time series stacks. *Remote Sensing of Environment, 114*, 183-198

Hudak, A.T., Strand, E.K., Vierling, L.A., Byrne, J.C., Eitel, J.U.H., Martinuzzi, S., & Falkowski, M.J. (2012). Quantifying aboveground forest carbon pools and fluxes from repeat LiDAR surveys. *Remote Sensing of Environment, 123*, 25-40

Hyde, P., Dubayah, R., Peterson, B., Blair, J.B., Hofton, M., Hunsaker, C., Knox, R., & Walker, W. (2005). Mapping forest structure for wildlife habitat analysis using waveform lidar: Validation of montane ecosystems. *Remote Sensing of Environment, 96*, 427-437

Imhoff, M.L. (1995). Radar backscatter and biomass saturation: ramifications for global biomass inventory. *IEEE Transactions on Geoscience and Remote Sensing, 33*, 511-518

Jenkins, J.C., Chojnacky, D.C., Heath, L.S., & Birdsey, R.A. (2003). National-scale biomass estimators for United States tree species. *Forest Science, 49*, 12-35

Jenkins, J.C., Chojnacky, D.C., Heath, L.S., & Birdsey, R.A. (2004). Comprehensive Database of Diameter-based Biomass Regressions for North American Tree Species. In, *General Technical Report NE-319*. Newtown Square, PA: U.S. Department of Agriculture, Forest Service, Northeastern Research Station

JPL (1994). SIR-C data compression software user guide. In J.P. Laboratory (Ed.). Pasadena, California: California Institute of Technology

JPL (2003). AIRSAR Integrated Processor Documentation. In, *AIRSAR data format*. Pasadena, CA: Jet Propulsion Laboratory Publication

Kasischke, E.S., Melack, J.M., & Craig Dobson, M. (1997). The use of imaging radars for ecological applications--A review. *Remote Sensing of Environment, 59*, 141-156

Kasischke, E.S., Tanase, M.A., Bourgeau-Chavez, L.L., & Borr, M. (2011). Soil moisture limitations on monitoring boreal forest regrowth using spaceborne L-band SAR data. *Remote Sensing of Environment, 115*, 227-232

Kellndorfer, J.M., Walker, W.S., LaPoint, E., Kirsch, K., Bishop, J., & Fiske, G. (2010). Statistical fusion of lidar, InSAR, and optical remote sensing data for forest stand height characterization: A regional-scale method based on LVIS, SRTM, Landsat ETM+, and ancillary data sets. *J. Geophys. Res., 115*, G00E08

Kuhn, M. (2008). Building predictive models in R using the caret package. *Journal of Statistical Software, 28*, 1-26

Kurvonen, L., Pulliainen, J., & Hallikainen, M. (1999). Retrieval of biomass in boreal forests from multitemporal ERS-1 and JERS-1 SAR images. *IEEE Transactions on Geoscience and Remote Sensing, 37*, 198-205

Langner, A., Achard, F., & Grassi, G. (2014). Can recent pan-tropical biomass maps be used to derive alternative Tier 1 values for reporting REDD+ activities under UNFCCC? *Environmental Research Letters, 9*

Le Quere, C., Peters, G.P., Andres, R.J., Andrew, R., Boden, T., Ciais, P., Friedlingstein, P., Houghton, R., Marland, G., & Moriarty, R. (2014). Global carbon budget 2013. *Earth System Science Data, 6*, 235-263

Lefsky, M.A. (2010). A global forest canopy height map from the Moderate Resolution Imaging Spectroradiometer and the Geoscience Laser Altimeter System. *Geophys. Res. Lett., 37*, L15401

Lefsky, M.A., Cohen, W.B., Harding, D.J., Parker, G.G., Acker, S.A., & Gower, S.T. (2002b). Lidar remote sensing of above ground biomass in three biomes. *Global Ecology and Biogeography, 11*, 393-399

Lefsky, M.A., Harding, D., Cohen, W.B., Parker, G., & Shugart, H.H. (1999). Surface Lidar Remote Sensing of Basal Area and Biomass in Deciduous Forests of Eastern Maryland, USA. *Remote Sensing of Environment, 67*, 83-98

Lefsky, M.A., Hudak, A.T., Cohen, W.B., & Acker, S.A. (2005a). Geographic variability in lidar predictions of forest stand structure in the Pacific Northwest. *Remote Sensing of Environment, 95*, 532-548

Lefsky, M.A., Keller, M., Pang, Y., De Camargo, P.B., & Hunter, M.O. (2007). Revised method for forest canopy height estimation from Geoscience Laser Altimeter System waveforms. *J. Appl. Remote Sens, 1*, 013537

Lefsky, M.A., Turner, D.P., Guzy, M., & Cohen, W.B. (2005b). Combining lidar estimates of aboveground biomass and Landsat estimates of stand age for spatially extensive validation of modeled forest productivity. *Remote Sensing of Environment, 95*, 549-558

Levine, E.R., Knox, R.G., & Lawrence, W.T. (1994). Relationships between soil properties and vegetation at the Northern Experimental Forest, Howland, Maine. *Remote Sensing of Environment, 47*, 231-241

Liaw, A., & Wiener, M. (2002). Classification and Regression by randomForest. *R news, 2*, 18-22

Lu, D. (2006). The potential and challenge of remote sensing-based biomass estimation. *International Journal of Remote Sensing, 27*, 1297-1328

Lu, D., Chen, Q., Wang, G., Liu, L., Li, G., & Moran, E. (2014). A survey of remote sensing-based aboveground biomass estimation methods in forest ecosystems. *International Journal of Digital Earth*, 1-64

Lucas, R., Armston, J., Fairfax, R., Fensham, R., Accad, A., Carreiras, J., Kelley, J., Bunting, P., Clewley, D., Bray, S., Metcalfe, D., Dwyer, J., Bowen, M., Eyre, T., Laidlaw, M., & Shimada, M. (2010). An Evaluation of the ALOS PALSAR L-Band Backscatter -- Above Ground Biomass Relationship Queensland, Australia: Impacts of Surface Moisture Condition and Vegetation Structure. *IEEE Journal of Selected Topics in Applied Earth Observations and Remote Sensing, 3*, 576-593

Luckman, A., Baker, J., Honzák, M., & Lucas, R. (1998). Tropical forest biomass density estimation using JERS-1 SAR: Seasonal variation, confidence limits, and application to image mosaics. *Remote Sensing of Environment, 63*, 126-139

Luckman, A., Baker, J., Kuplich, T.M., Yanasse, C.d.C.F., & Frery, A.C. (1997). A study of the relationship between radar backscatter and regenerating tropical forest biomass for spaceborne SAR instruments. *Remote Sensing of Environment, 60*, 1-13

Malhi, Y., Baldocchi, D., & Jarvis, P. (1999). The carbon balance of tropical, temperate and boreal forests. *Plant, Cell & Environment, 22*, 715-740

Mallet, C., & Bretar, F. (2009). Full-waveform topographic lidar: State-of-the-art. *ISPRS Journal of Photogrammetry and Remote Sensing, 64*, 1-16

Mascaro, J., Detto, M., Asner, G.P., & Muller-Landau, H.C. (2011). Evaluating uncertainty in mapping forest carbon with airborne LiDAR. *Remote Sensing of Environment, 115*, 3770-3774

Mather, P.M. (2004). *Computer Processing of Remotely Sensed Images*. Chichester, West Sussex, England: John Wiley & Sons Ltd.

Means, J.E., Acker, S.A., Harding, D.J., Blair, J.B., Lefsky, M.A., Cohen, W.B., Harmon, M.E., & McKee, W.A. (1999). Use of Large-Footprint Scanning Airborne Lidar To Estimate Forest Stand Characteristics in the Western Cascades of Oregon. *Remote Sensing of Environment, 67*, 298-308

Menges, C., Van Zyl, J., Hill, G., & Ahmad, W. (2001). A procedure for the correction of the effect of variation in incidence angle on AIRSAR data. *International Journal of Remote Sensing, 22*, 829-841

Mitchard, E., Saatchi, S., White, L., Abernethy, K., Jeffery, K., Lewis, S., Collins, M., Lefsky, M., Leal, M., & Woodhouse, I. (2011a). Mapping tropical forest biomass

with radar and spaceborne LiDAR: overcoming problems of high biomass and persistent cloud. *Biogeosciences Discuss, 8*, 8781-8815

Mitchard, E.T.A., Saatchi, S.S., Lewis, S.L., Feldpausch, T.R., Woodhouse, I.H., Sonké, B., Rowland, C., & Meir, P. (2011b). Measuring biomass changes due to woody encroachment and deforestation/degradation in a forest-savanna boundary region of central Africa using multi-temporal L-band radar backscatter. *Remote Sensing of Environment, 115*

Mitchard, E.T.A., Saatchi, S.S., Woodhouse, I.H., Nangendo, G., Ribeiro, N.S., Williams, M., Ryan, C.M., Lewis, S.L., Feldpausch, T.R., & Meir, P. (2009a). Using satellite radar backscatter to predict above-ground woody biomass: A consistent relationship across four different African landscapes. *Geophys. Res. Lett., 36*, L23401

Mitchard, E.T.A., Saatchi, S.S., Woodhouse, I.H., Nangendo, G., Ribeiro, N.S., Williams, M., Ryan, C.M., Lewis, S.L., Feldpausch, T.R., & Meir, P. (2009b). Using satellite radar backscatter to predict above-ground woody biomass: A consistent relationship across four different African landscapes. *Geophysical Research Letters, 36*, L23401

Monk, C.D., Child, G.I., & Nicholson, S.A. (1970). Biomass, Litter and Leaf Surface Area Estimates of an Oak-Hickory Forest. *Oikos, 21*, 138-141

Næsset, E., & Gobakken, T. (2008). Estimation of above- and below-ground biomass across regions of the boreal forest zone using airborne laser. *Remote Sensing of Environment, 112*, 3079-3090

Næsset, E., Gobakken, T., Bollandsås, O.M., Gregoire, T.G., Nelson, R., & Ståhl, G. (2013). Comparison of precision of biomass estimates in regional field sample surveys and airborne LiDAR-assisted surveys in Hedmark County, Norway. *Remote Sensing of Environment, 130*, 108-120

Nelson, R., Ranson, K.J., Sun, G., Kimes, D.S., Kharuk, V., & Montesano, P. (2009). Estimating Siberian timber volume using MODIS and ICESat/GLAS. *Remote Sensing of Environment, 113*, 691-701

Ni-Meister, W., Lee, S., Strahler, A.H., Woodcock, C.E., Schaaf, C., Yao, T., Ranson, K.J., Sun, G., & Blair, J.B. (2010). Assessing general relationships between aboveground biomass and vegetation structure parameters for improved carbon estimate from lidar remote sensing. *J. Geophys. Res., 115*, G00E11

Ni, W., Sun, G., Guo, Z., Zhang, Z., He, Y., & Huang, W. (2013a). Retrieval of Forest Biomass From ALOS PALSAR Data Using a Lookup Table Method. *IEEE Journal of Selected Topics in Applied Earth Observations and Remote Sensing, V6*, 875-886

Ni, W., Sun, G., Zhang, Z., Guo, Z., & He, Y. (2013b). Co-registration of two DEMs: impacts on forest height estimation from SRTM and NED at Mountainous Areas. *IEEE Geoscience and Remote Sensing Letter*

Nilsson, M. (1996). Estimation of tree heights and stand volume using an airborne lidar system. *Remote Sensing of Environment, 56*, 1-7

Nunery, J.S., & Keeton, W.S. (2010). Forest carbon storage in the northeastern United States: Net effects of harvesting frequency, post-harvest retention, and wood products. *Forest Ecology and Management, 259*, 1363-1375

Pang, Y., Lefsky, M., Andersen, H.E., Miller, M.E., & Sherrill, K. (2008). Validation of the ICEsat vegetation product using crown-area-weighted mean height derived using crown delineation with discrete return lidar data. *Canadian Journal of Remote Sensing, 34*, S471-S484

Peddle, D.R., Huemmrich, K.F., Hall, F.G., Masek, J.G., Soenen, S.A., & Jackson, C.D. (2011). Applications of the BIOPHYS Algorithm for Physically-Based Retrieval of Biophysical, Structural and Forest Disturbance Information. *IEEE Journal of Selected Topics in Applied Earth Observations and Remote Sensing, 4*, 971-982

Pope, K.O., Rey-Benayas, J.M., & Paris, J.F. (1994). Radar remote sensing of forest and wetland ecosystems in the Central American tropics. *Remote Sensing of Environment, 48*, 205-219

Pottier, E., Ferro-Famil, L., Allain, S., Cloude, S.R., Hajnsek, I., Papathanassiou, K., Moreira, A., Williams, M., Minchella, A., Lavalle, M., & Desnos, Y.L. (2009). Overview of the PolSARpro v4.0: The open source toolbox for polarimetric and interferometric polarimetric SAR data processing. In, *International Geoscience and Remote Sensing Symposium* (pp. 936-939). Capetown, South Africa

Ranson, K.J., Saatchi, S., & Guoqing, S. (1995). Boreal forest ecosystem characterization with SIR-C/XSAR. *IEEE Transactions on Geoscience and Remote Sensing, 33*, 867-876

Ranson, K.J., & Sun, G. (1997). An evaluation of AIRSAR and SIR-C/X-SAR images for mapping northern forest attributes in Maine, USA. *Remote Sensing of Environment, 59*, 203-222

Ranson, K.J., & Sun, G. (2000). Effects of environmental conditions on boreal forest classification and biomass estimates with SAR. *IEEE Transactions on Geoscience and Remote Sensing, 38*, 1242-1252

Ranson, K.J., Sun, G., Knox, R.G., Levine, E.R., Weishampel, J.F., & Fifer, S.T. (2001). Northern Forest Ecosystem Dynamics Using Coupled Models and Remote Sensing. *Remote Sensing of Environment, 75*, 291-302

Ranson, K.J., Sun, G., Lang, R.H., Chauhan, N.S., Cacciola, R.J., & Kilic, O. (1997c). Mapping of boreal forest biomass from spaceborne synthetic aperture radar. *J. Geophys. Res., 102*, 29599-29610

Robinson, C., Saatchi, S., Neumann, M., & Gillespie, T. (2013). Impacts of Spatial Variability on Aboveground Biomass Estimation from L-Band Radar in a Temperate Forest. *Remote Sensing, 5*, 1001-1023

Rosenqvist, Å., Milne, A., Lucas, R., Imhoff, M., & Dobson, C. (2003). A review of remote sensing technology in support of the Kyoto Protocol. *Environmental Science & Policy, 6*, 441-455

Rowland, C.S., Balzter, H., Dawson, T.P., Luckman, A., Patenaude, G., & Skinner, L. (2008). Airborne SAR monitoring of tree growth in a coniferous plantation. *International Journal of Remote Sensing, 29*, 3873-3889

Saatchi, S., Dubayah, R., Clark, D., Chazdon, R., & Hollinger, D. (2010). Estimation of Forest Biomass Change From Fusion of Radar and Lidar. In, *IEEE International Geoscience and Remote Sensing Symposium*. Honolulu, Hawaii, USA

Saatchi, S., Marlier, M., Chazdon, R.L., Clark, D.B., & Russell, A.E. (2011a). Impact of spatial variability of tropical forest structure on radar estimation of aboveground biomass. *Remote Sensing of Environment, 115*, 2836-2849

Saatchi, S.S., Harris, N.L., Brown, S., Lefsky, M., Mitchard, E.T.A., Salas, W., Zutta, B.R., Buermann, W., Lewis, S.L., Hagen, S., Petrova, S., White, L., Silman, M., & Morel, A. (2011b). Benchmark map of forest carbon stocks in tropical regions across three continents. *Proceedings of the National Academy of Sciences, 108*, 9899-9904

Safford, L.O., Frank, R.M., & Little, E.L. (1969). *Trees and shrubs of the Penobscot Experimental Forest, Penobscot County, Maine*: Northeastern Forest Experiment Station

Salas, W., Ducey, M., Rignot, E., & Skole, D. (2002). Assessment of JERS-1 SAR for monitoring secondary vegetation in Amazonia: I. Spatial and temporal variability in backscatter across a chrono-sequence of secondary vegetation stands in Rondonia. *International Journal of Remote Sensing, 23*, 1357-1379

Sandberg, G., Ulander, L.M.H., Fransson, J.E.S., Holmgren, J., & Le Toan, T. (2011). L- and P-band backscatter intensity for biomass retrieval in hemiboreal forest. *Remote Sensing of Environment, 115*, 2874-2886

Sandberg, G., Ulander, L.M.H., Wallerman, J., & Fransson, J.E.S. (2014). Measurements of Forest Biomass Change Using P-Band Synthetic Aperture Radar Backscatter. *IEEE Transactions on Geoscience and Remote Sensing, 52*, 6047-6061

Santoro, M., Fransson, J.E.S., Eriksson, L.E.B., & Ulander, L.M.H. (2010). Clear-Cut Detection in Swedish Boreal Forest Using Multi-Temporal ALOS PALSAR Backscatter Data. *IEEE Journal of Selected Topics in Applied Earth Observations and Remote Sensing, 3*, 618-631

Santos, J.R., Lacruz, M.S.P., Araujo, L.S., & Keil, M. (2002). Savanna and tropical rainforest biomass estimation and spatialization using JERS-1 data. *International Journal of Remote Sensing, 23*, 1217-1229

Scott, N.A., Rodrigues, C.A., Hughes, H., Lee, J.T., Davidson, E.A., Dail, D.B., Malerba, P., & Hollinger, D.Y. (2004). Changes in carbon storage and net carbon exchange one year after an initial shelterwood harvest at Howland Forest, ME. *Environmental Management, 33*, 9-22

Shimada, M., Isoguchi, O., Tadono, T., & Isono, K. (2009). PALSAR radiometric and geometric calibration. *IEEE Transactions on Geoscience and Remote Sensing, 47*, 3915-3932

Shimoda, H., & Xiong, X. (2012). Earth Observing Missions and Sensors: Development, Implementation, and Characterization II. In, *Proc. of SPIE Vol* (pp. 852801-852801)

Small, D. (2011). Flattening Gamma: Radiometric Terrain Correction for SAR Imagery. *Geoscience and Remote Sensing, IEEE Transactions on, 49*, 3081-3093

Solberg, S. (2010). Mapping gap fraction, LAI and defoliation using various ALS penetration variables. *International Journal of Remote Sensing, 31*, 1227 - 1244

Sumantyo, J.T.S., & Amini, J. (2008). A model for removal of speckle noise in SAR images (ALOS PALSAR). *Canadian Journal of Remote Sensing, 34*, 503-515

Sun, G., & Ranson, K.J. (1998). Radar modelling of forest spatial patterns. *International Journal of Remote Sensing, 19*, 1769-1791

Sun, G., Ranson, K.J., Guo, Z., Zhang, Z., Montesano, P., & Kimes, D. (2011). Forest biomass mapping from lidar and radar synergies. *Remote Sensing of Environment, 115*, 2906-2916

Sun, G., Ranson, K.J., & Kharuk, V.I. (2002). Radiometric slope correction for forest biomass estimation from SAR data in the Western Sayani Mountains, Siberia. *Remote Sensing of Environment, 79*, 279-287

Sun, G., Simonett, D.S., & Strahler, A.H. (1991). A radar backscatter model for discontinuous coniferous forests. *IEEE Transactions on Geoscience and Remote Sensing, 29*, 639-650

Swatantran, A., Dubayah, R., Roberts, D., Hofton, M., & Blair, J.B. (2011). Mapping biomass and stress in the Sierra Nevada using lidar and hyperspectral data fusion. *Remote Sensing of Environment, 115*, 2917–2930

Thomas, N.E., Huang, C., Goward, S.N., Powell, S., Rishmawi, K., Schleeweis, K., & Hinds, A. (2011). Validation of North American Forest Disturbance dynamics derived from Landsat time series stacks. *Remote Sensing of Environment, 115*, 19-32

Urban, D. (1990). A versatile model to simulate forest pattern: a user's guide to ZELIG version 1.0. *Environmental Sciences Department, The University of Virginia, Charlottesville, Virginia*

Ustin, S., Wessman, C., Curtiss, B., Kasischke, E., Way, J.B., & Vanderbilt, V. (1991). Opportunities for using the EOS imaging spectrometers and synthetic aperture radar in ecological models. *Ecology, 72*, 1934-1945

Wang, Y., Day, J.L., Davis, F.W., & Melack, J.M. (1993). Modeling L-band radar backscatter of Alaskan boreal forest. *IEEE Transactions on Geoscience and Remote Sensing, 31*, 1146-1154

Way, J., Paris, J., Dobson, M.C., McDonals, K., Ulaby, F.T., Weber, J., Ustin, L., Vanderbilt, V.C., & Kasischke, E.S. (1991). Diurnal change in trees as observed by optical and microwave sensors: the EOS synergism study. *IEEE Transactions on Geoscience and Remote Sensing, 29*, 807-821

Weisbin, C.R., Lincoln, W., & Saatchi, S. (2013). A Systems Engineering Approach to Estimating Uncertainty in Above-Ground Biomass (AGB) Derived from Remote-Sensing Data. *Systems Engineering*

Young, H.E., Ribe, J.H., & Wainwright, K. (1980). Weight tables for tree and shrub species in Maine. In, *Miscellaneous Report 230*. , University of Maine at Orono: Life Sciences and Agriculture Experiment Station

Zhang, Z. (2011). Biomass retrieval based on lidar and SAR data. In, *School of Geography and Remote Sensing* (p. 140). Beijing: Beijing Normal University

Zhao, K., & Popescu, S. (2009). Lidar-based mapping of leaf area index and its use for validating GLOBCARBON satellite LAI product in a temperate forest of the southern USA. *Remote Sensing of Environment, 113*, 1628-1645

Zhao, K., Popescu, S., Meng, X., Pang, Y., & Agca, M. (2011). Characterizing forest canopy structure with lidar composite metrics and machine learning. *Remote Sensing of Environment, 115*, 1978-1996

Zink, M., Olivier, P., & Freeman, A. (1993). Cross-calibration between airborne SAR sensors. *IEEE Transactions on Geoscience and Remote Sensing, 31*, 237-245